Master of Science Thesis

Graphene oxide as a filler for improved conductivity and mechanical stability in poly(co-aryl piperidinium) anion exchange membranes

Letizia Calzolari

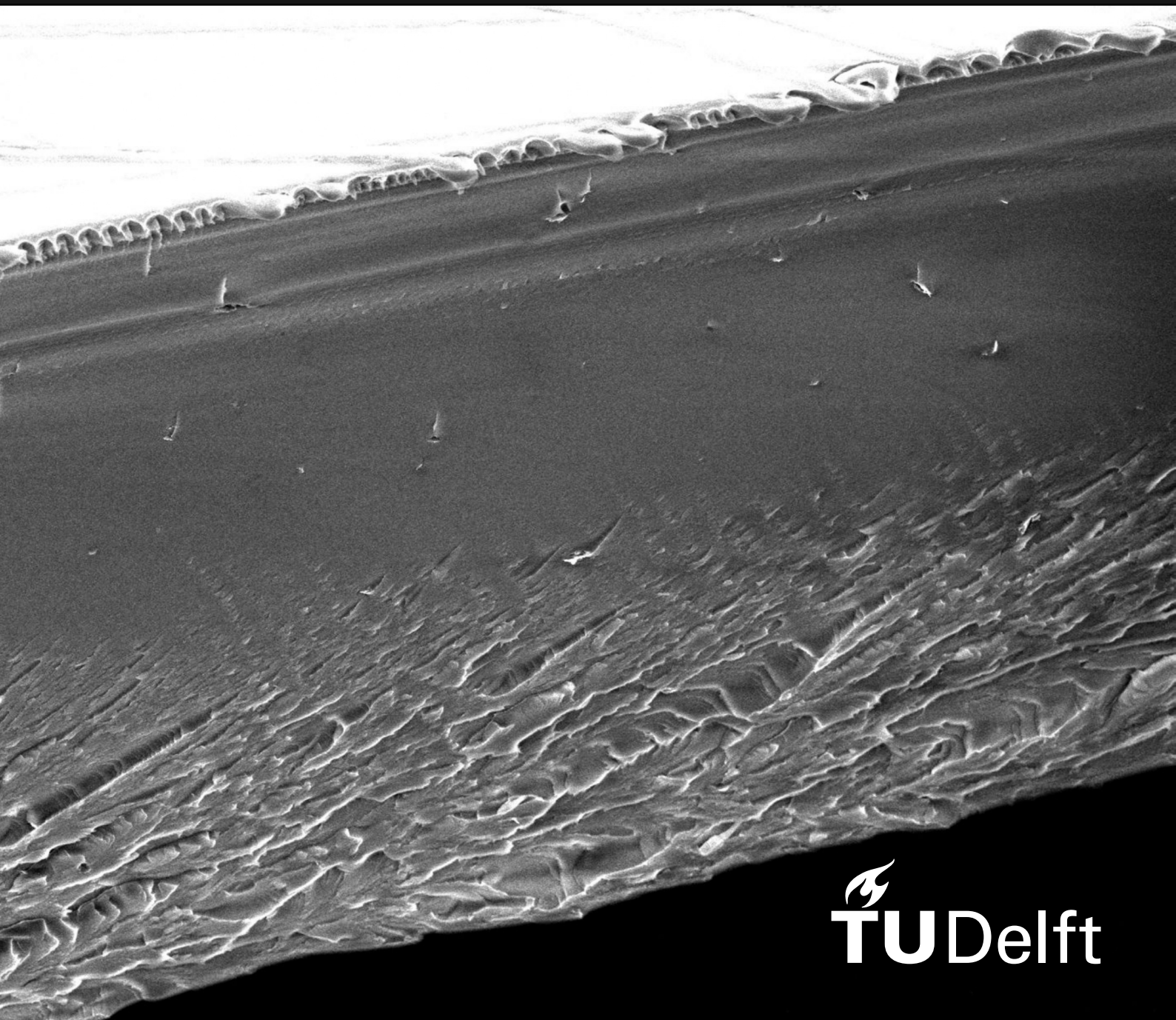

TU Delft

Master of Science Thesis

Graphene oxide as a filler for improved conductivity and mechanical stability in poly(co-aryl piperidinium) anion exchange membranes

by

Letizia Calzolari

Student Number 5864852

Supervisors:	David Vermaas, Hanieh Bazyar
Daily Supervisor:	Thanos Papageorgiou
Project Duration:	May, 2024 - November, 2024
Faculty:	Faculty of Chemical Engineering, Delft

Defense Date: 21 November, 2024

TU Delft

Preface

Over the past months, working on this project has been both challenging and rewarding. One of the most memorable moments came after weeks—or rather, months—of refining the membrane fabrication procedure. When I finally succeeded, I felt incredibly proud that all the effort had paid off. In the end, it all came down to 50 microliters of water. This project has once again reminded me of the value of patience and determination in life. I feel grateful and proud to have worked on a project that supports the essential scientific progress needed to help ensure a livable future for my generation.

I would like to thank my daily supervisor, Dr. Thanos Papageorgiou, for his guidance throughout this project. His steady encouragement and positive outlook helped me through the challenges. I also want to thank Professor David Vermaas for his insightful feedback and Professor Baris Kumru for his valuable assistance. I am grateful to both for taking the time to serve on my committee and for reviewing my thesis. I also thank Professor Hanieh Bazyar for welcoming me into this project.

I want to express my gratitude to the lab technicians, Aleksandra Kondakova, Sietse Kuipers, and Liliana Baron, who provided training and patiently answered all my questions, helping me build confidence in the lab.

This thesis marks the closing chapter of my student life, a journey that began in Bologna, Italy, and has brought me here to Delft, Netherlands. It has been a journey filled with challenges, excitement, and discovery, driven by my curiosity for science.

Reflecting on this experience, I feel deeply grateful to the people who supported me. I'd like to thank my friends in Delft, both in Chemical Engineering and from my house, for making this place feel like a new home and for sharing the highs and lows. To my friends in Italy, your encouragement, interest, and constant presence, even from afar, have been invaluable to me.

Finally, I want to thank Tommi, my companion and support in this journey, and in many more to come. And to my family—my grandparents, my siblings, and my parents—you have always believed in me, encouraged me to do my best, and stood by me every step of the way. Thank you for everything.

Letizia Calzolari

Abstract

The drive for sustainable hydrogen production has highlighted Anion Exchange Membrane Water Electrolysis (AEMWE) as a promising technology. Operating in alkaline conditions, AEMWE can utilize non-precious metal catalysts, offering a cost-effective alternative to proton exchange membrane (PEM) electrolysis. Achieving industrial scalability for AEMWE, however, depends on enhancing the performance of anion exchange membranes (AEMs), particularly by improving hydroxide ion conductivity, mechanical properties and stability in alkaline media.

This study aims to determine the optimal graphene oxide (GO) concentration as a nanofiller in poly(co-aryl piperidinium) AEMs to maximize hydroxide conductivity and dimensional stability. The research followed a two-stage approach: first, developing a reproducible membrane fabrication method to create uniform GO-AEM composites, refining solvent composition, thermal treatment, and mixing techniques. Key improvements, including a 5% water-DMSO co-solvent system, enhanced GO-polymer interactions and stability across GO concentrations.

In the second stage, various GO concentrations were systematically evaluated to identify an optimal loading. Conductivity testing revealed a peak at 0.5% GO, where conductivity nearly doubled from 33 mS/cm in the pristine membrane to 59 mS/cm, attributed to enhanced ion-conducting pathways. Ion exchange capacity (IEC) slightly declined, suggesting GO's active participation in ion conduction or structural improvement. Electrochemical performance tests demonstrated that membranes with higher conductivity corresponded to improved current densities.

Microscopic and thermal analyses (SEM, AFM, TGA) verified uniform GO dispersion at low to moderate concentrations, with agglomeration observed at 1%, correlating with conductivity and stability trends. Mechanical testing indicated an initial reduction in stiffness and hardness at low GO loadings, followed by reinforcement at higher concentrations. Water uptake (WU) peaked at 0.125% GO before declining, while swelling ratio (SR) followed an inverse trend, optimizing dimensional stability and water management at 0.125% loading. Post-electrolysis, higher GO concentrations effectively limited swelling, confirming improved operational dimensional stability.

In conclusion, this study demonstrates that integrating GO into poly(co-aryl piperidinium) AEMs effectively enhances ion conductivity and mechanical stability, essential for advancing AEMWE at scale. The 0.125% GO concentration achieved highest water uptake (17%, up from 7% in the pristine membrane) and minimized swelling (6%, down from 13%), while the 0.5% loading delivered peak hydroxide conductivity (59 mS/cm, nearly doubling from 33 mS/cm) and improved operational mechanical stability (post-electrolysis swelling ratio of 27%, down from 37%), establishing this composition as a promising candidate for efficient AEMWE applications.

Contents

List of Figures

List of Tables

Nomenclature

Abbreviations

Abbreviation	Definition
AEM	Anion Exchange Membrane
AEMWE	Anion Exchange Membrane Water Electrolysis
AEI	Anion Exchange Ionomer
AFM	Atomic Force Microscopy
AWE	Alkaline Water Electrolysis
CCM	Catalyst-Coated Membrane
CCS	Catalyst-Coated Substrate
CP	Chronopotentiometry
CV	Cyclic Voltammetry
DLS	Dynamic Light Scattering
DMSO	Dimethyl Sulfoxide
DMA	Dynamic Mechanical Analysis
DSC	Differential Scanning Calorimetry
DTG	Derivative Thermogravimetry
EDS	Energy Dispersive Spectroscopy
EtOH	Ethanol
FT-IR	Fourier-Transform Infrared Spectroscopy
GDL	Gas Diffusion Layer
GO	Graphene Oxide
GPC	Gel Permeation Chromatography
GHG	Greenhouse Gas
HER	Hydrogen Evolution Reaction
IEC	Ion Exchange Capacity
PDI	Polydispersity Index
RD	Research and Development
SEM	Scanning Electron Microscopy
SOEC	Solid Oxide Electrolysis
SR	Swelling Ratio
TGA	Thermogravimetric Analysis
UTM	Universal Testing Machine
WU	Water Uptake

Symbols

Symbol	Definition	Unit
A_{membrane}	Membrane Area	[cm^2]
A_c	Projected Contact Area in nano-indentation	[nm^2]
C_{AgNO_3}	Concentration of $AgNO_3$	[M]
c	Polymer Concentration	[g/dL]
d	Thickness	[µm]
D	Hydrodynamic Diameter	[nm]
E	Young's Modulus	[GPa]
E_r	Reduced Modulus	[GPa]

Symbol	Definition	Unit
E_{rev}	Reversible Cell Potential	[V]
E_{tn}	Thermo-neutral Potential	[V]
F	Faraday Constant	[C/mol]
G	Conductance	[mS/cm^2]
H	Hardness	[GPa]
H_{mix}	Enthalpy of Mixing	[kJ/mol]
i	Current Density	[mA/cm^2]
IEC	Ion Exchange Capacity	[meq/g]
k_H	Huggins Constant	[-]
K	Mark-Houwink Parameter	[-]
ΔG°	Gibbs Free Energy Change	[kJ/mol]
ΔH°	Enthalpy Change	[kJ/mol]
ΔS°	Entropy Change	[J/mol K]
M_{dry}	Mass of Dry Membrane	[g]
M_{wet}	Mass of Wet Membrane	[g]
M_v	Viscosity-average Molar Mass	[g/mol]
P_{max}	Maximum Load in nano-indentation	[N]
R_{blank}	System Resistance (Blank)	[Ohm]
R_{membrane}	Membrane Resistance	[Ohm]
R_{total}	Total System Resistance	[Ohm]
S	Contact Stiffness	[N/m]
SR	Swelling Ratio	[-]
σ	Conductivity	[S/cm]
T_{dry}	Thickness of Dry Membrane	[µm]
T_{wet}	Thickness of Wet Membrane	[µm]
T	Temperature	[°C] or [K]
T_g	Glass Transition Temperature	[°C]
V_{cell}	Cell Voltage	[V]
V_{AgNO_3}	Volume of $AgNO_3$	[mL]
V_{act}	Activation Overpotential	[V]
WU	Water Uptake	[-]
$[\eta]$	Intrinsic Viscosity	[dL/g]
η	Solution Viscosity	[Pa·s]
η_0	Solvent Viscosity	[Pa·s]
η_{sp}	Specific Viscosity	[-]
ν	Poisson's Ratio	[-]
ε_r	Dielectric Constant	[-]

1

Introduction

The pursuit of sustainable and reliable energy sources has intensified as the global demand for energy increases, alongside the urgent need to address the escalating climate crisis. Currently, over 80% of global energy consumption relies on fossil fuels, a primary driver of greenhouse gas emissions and, consequently, global warming and climate instability [54]. International initiatives like the Paris Agreement and the European Green Deal underscore the need for significant emission reductions and a shift toward renewable energy sources [115]. However, the intermittent nature of renewable power sources, such as wind and solar, necessitates efficient storage solutions to ensure stable power generation [96]. In this context, hydrogen is emerging as a critical energy carrier, with potential both as a storage medium and as a zero-emission fuel when produced via renewable-powered water electrolysis [7]. Yet, less than 5% of hydrogen production is currently "green," with most hydrogen still derived from fossil fuels [9].

Among water electrolysis technologies, anion exchange membrane water electrolysis (AEMWE) is gaining interest as a cost-effective alternative to proton exchange membrane (PEM) electrolysis. Operating under alkaline conditions, AEMWE offers the advantage of using non-precious metal catalysts, which significantly lowers material costs while maintaining high hydrogen purity [61]. For AEMWE to reach viable large-scale application, however, advancements across multiple aspects, particularly in the anion exchange membranes (AEMs) themselves, are essential [26]. Specifically, improvements in hydroxide ion conductivity, mechanical stability, and resistance to alkaline degradation are crucial for AEM performance [74].

Recent research has thus focused on optimizing AEM structure and composition to achieve these targets. Among these advancements, newly developed polymers like poly(co-aryl piperidinium) have shown promise in meeting AEM requirements for conductivity, stability, and mechanical properties [14, 17]. In this project, a variant of poly(co-aryl piperidinium), not commercially available and supplied by the project's industrial partner HyET, serves as the base material for further enhancement.

A key challenge in AEM development remains managing the trade-off between ion conductivity and mechanical stability [74]. While increasing water uptake generally enhances conductivity by facilitating ion transport, it also leads to membrane swelling, compromising strength and stability. To address this, recent studies have investigated methods such as cross-linking, phase separation, and advanced casting techniques, each aiming to optimize AEM performance by balancing these demands [26].

A more recent approach involves incorporating nanofillers into the AEM matrix to improve ion conductivity and mechanical stability by forming organized ion-conducting pathways and reinforcing the membrane structure [87]. Among these, graphene oxide (GO) has shown particular potential in AEM research, demonstrating enhancements in conductivity, reduced swelling, and improved alkaline stability when integrated into various polymer matrices [83, 77]. However, studies indicate that the effect of GO is highly matrix-specific, with performance improvements dependent on the interaction and compatibility between the filler and the specific polymer matrix.

To date, GO has not yet been explored as a filler in poly(co-aryl piperidinium) AEMs. In this thesis, therefore, GO is investigated as a filler for poly(co-aryl piperidinium) to assess its impact on electrochemical performance, focusing on conductivity and mechanical stability, two essential properties for effective AEM function. The aim is to determine an optimal GO loading that enhances both properties, addressing the typical trade-off between ion conductivity and structural stability. The central research question guiding this study is: *What is the optimal loading of graphene oxide filler for improving ion conductivity and mechanical stability in poly(co-aryl piperidinium) anion exchange membranes?*

The research framework comprises two main stages. First, a reproducible membrane-casting method will be developed to create composite membranes with varying GO concentrations. Second, these membranes will undergo comprehensive testing to evaluate key AEM properties. Through this approach, the study aims to identify the optimal amount of graphene oxide needed to enhance the performance of a poly(co-aryl piperidinium) membrane, providing insights into GO's role as an effective filler material for advanced AEMs. Ultimately, this research seeks to contribute to the broader goal of advancing AEMWE technology to support efficient and sustainable hydrogen production.

This report describes the research presented, moving from context and background to experimental findings and conclusions:

- Chapter 2 situates hydrogen, specifically "green hydrogen" produced via water electrolysis, as a critical element in the energy transition. It surveys global energy trends, the pressing climate crisis, and the technological and policy-driven shifts toward renewable energy.
- Chapter 3 delves into the principles of water electrolysis, with a focus on AEMWE as a promising approach. This chapter provides an in-depth discussion of AEMs and highlights current strategies for improving them, with a focus on nanofillers, like GO, culminating in the research proposal of this thesis.
- Chapter 4 details the experimental procedures, including the process for fabricating membranes with varying GO concentrations and the membrane-casting method; the detailed iterative process leading to a successful fabrication method is provided in the appendix. This chapter also outlines the testing protocols used to evaluate membrane properties.
- Chapter 5 presents and discusses the results and key findings, evaluating the effects of different GO loadings on membrane performance. The analysis includes a discussion of conductivity, mechanical properties and stability improvements. This chapter explores the relationship between GO content and AEM structure, identifying an optimal concentration.
- Chapters 6 and 7 present the conclusions, recommendations, and outlook of this research. The thesis concludes by summarizing the findings, reflecting on their implications for AEMWE technology, and suggesting potential avenues for future research.

2

Energy Landscape

2.1. Global Energy and Environmental Challenges

The rising global energy demand, fueled by population growth and industrial expansion, has led to extensive fossil fuel use, which significantly contributes to greenhouse gas (GHG) emissions. Fossil fuels, including coal, oil, and natural gas, currently account for over 80% of global energy consumption, with approximately 70% reliance in Europe [54, 56]. Combustion of these fuels releases substantial amounts of carbon dioxide (CO_2) and other greenhouse gases (e.g., nitrogen oxides, NOx) into the atmosphere, driving global warming and climate change. This environmental crisis is evident through extreme weather events, such as the unusually severe flooding recently experienced in my hometown Bologna, Italy, as well as rising sea levels and biodiversity loss, all of which threaten ecosystems and human life. The continued dependence on finite fossil fuel resources also raises concerns about energy security, highlighting the need for a fundamental reassessment of energy consumption and production.

In response, the Paris Agreement, signed in 2015, set the goal of limiting global temperature rise to well below 2°C, with efforts to cap the increase at 1.5°C [115]. Additionally, the European Green Deal targets a minimum 55% reduction in GHG emissions by 2030 compared to 1990 levels, and an increase in the share of renewable energy in the EU's energy mix to 32%, revised more ambitiously to 42.5% under the Renewable Energy Directive [115, 34]. Achieving these goals requires an immediate reduction in carbon emissions, a shift from fossil fuels to renewable sources, and efforts to capture existing carbon emissions in the atmosphere and oceans. As of 2020, renewable energy contributed around 10% of global energy consumption, insufficient to meet international climate targets [91]. More specifically, the EU has made notable progress toward its 2030 climate goals; as of 2022, the EU had reduced emissions by about 32.5% from 1990 levels, with renewables comprising 23% of the EU's total energy consumption [33, 35]. However, challenges remain. One major obstacle to renewable energy adoption is intermittency; wind and solar power, while clean and sustainable, cannot consistently provide continuous energy, highlighting the need for efficient energy storage solutions to ensure stable, reliable power generation [96].

2.2. Hydrogen as a Solution

Hydrogen, one of the most abundant elements on earth, is emerging as a critical component of the global energy transition due to its versatility and potential to reduce emissions across various sectors. Hydrogen can serve as a zero-emission fuel, an energy storage medium, and a carrier, as well as a green feedstock for chemical and other industries [7].

A primary role of hydrogen lies in its capacity as an energy carrier. Excess electricity generated from renewable sources, such as wind and solar, can be used to produce hydrogen through water electrolysis, a process that splits water into hydrogen and oxygen. Hydrogen can then be stored and reconverted to electricity as needed, addressing the intermittency of renewable sources. Although hydrogen has a higher energy density than conventional fossil fuels, its low volumetric density may favor its conversion into ammonia, methanol or liquid organic hydrogen carriers for storage and transport [1].

When used as fuel in fuel cells, hydrogen reacts with oxygen to produce water as the only byproduct, making it a zero-emission energy carrier. Hydrogen can also be used in direct combustion for energy production [99]. Additionally, hydrogen is essential in decarbonizing industries that are hard to electrify, such as steel and cement production, where it can serve as an industrial feedstock. Beyond its current use in sectors like oil refining and ammonia production, hydrogen has the potential to replace fossil fuels in heavy industries, significantly reducing carbon emissions. Global hydrogen demand reached approximately 95 million tons (Mt) in 2022, with projections in the Net Zero Scenario estimating a demand increase to 530 Mt by 2050, with 50-65% of this being green hydrogen [79, 55].

2.2.1. Production of Hydrogen

Currently, hydrogen production is predominantly based on fossil fuels, accounting for around 96% of global hydrogen production through processes that release significant CO_2 emissions, such as methane steam reforming, making it unsustainable as a long-term solution [9].

Hydrogen is categorized by ”colors” based on the energy sources and processes used for production [127]. Gray hydrogen is produced from natural gas without capturing emissions, while blue hydrogen incorporates carbon capture and storage (CCS) to mitigate CO_2 emissions. Green hydrogen, the most sustainable form, is produced with minimal or zero GHG emissions, using renewable energy. While water electrolysis is the primary method for green hydrogen production, other emerging methods include biomass gasification, photocatalytic splitting, and microbial electrolysis. Renewable energy is essential for hydrogen production to maintain zero emissions, ensuring it serves as a truly clean energy source.

Water electrolysis remains the most viable sustainable method, producing hydrogen by splitting water into hydrogen and oxygen with zero carbon emissions or byproducts. Currently, only around 4% of global hydrogen is produced via electrolysis [9]. The cost of hydrogen from methane steam reforming ranges from €1.5 to €2.5 per kilogram, depending on natural gas prices, and with CCS, between €3 and €4 per kilogram. Green hydrogen in Europe is currently around €4 to €7 per kilogram, varying with electricity costs and electrolyzer efficiency [93, 40]. Innovations in electrolyzer technology and declining renewable energy costs are expected to make this method increasingly viable for large-scale production.

The role of green hydrogen is projected to expand substantially in the global energy transition. Significant investments from academia, industry, and government incentives aim to enhance electrolyzer efficiency, reduce production costs, and scale up hydrogen production to meet ambitious climate targets. For green hydrogen to become a competitive and viable option, production costs must match those of mature technologies, underscoring the need for continued optimization of developing hydrogen technologies.

In the next chapter, we will explore the theory of water electrolysis, delving into the mechanisms, challenges, and innovations essential for optimizing this technology for sustainable hydrogen production.

3

Theoretical Background

3.1. Water Electrolysis

3.1.1. Fundamentals

Water electrolysis is an electrochemical process that splits water (H_2O) into hydrogen (H_2) and oxygen (O_2) using electrical energy. This process is a key method for producing hydrogen, particularly when powered by renewable energy, as it results in no direct carbon emissions. The overall reaction is:

$$\mathrm{H_2O\,(l)} \longrightarrow \mathrm{H_2\,(g)} + \frac{1}{2}\,\mathrm{O_2\,(g)} \tag{3.1}$$

Water electrolysis consists of two half-reactions: the Hydrogen Evolution Reaction (HER) at the cathode and the Oxygen Evolution Reaction (OER) at the anode. In alkaline conditions, the reactions are [94]:

Cathode (HER):

$$2\,\mathrm{H_2O} + 2\,\mathrm{e^-} \longrightarrow \mathrm{H_2\,(g)} + 2\,\mathrm{OH^-} \tag{3.2}$$

Anode (OER):

$$2\,\mathrm{OH^-} \longrightarrow \frac{1}{2}\,\mathrm{O_2\,(g)} + \mathrm{H_2O} + 2\,\mathrm{e^-} \tag{3.3}$$

The minimum energy required for water electrolysis is described by the Gibbs free energy change (ΔG°) of the overall reaction, which is 237.21 kJ/mol at standard conditions (25°C, 1 atm). This corresponds to the reversible cell potential (E°_{rev}) of 1.23 V, which represents the theoretical minimum voltage necessary to drive the water-splitting reaction. The relationship between the Gibbs free energy and the cell potential is given by [107]:

$$\Delta G^\circ = -nFE^\circ_{\text{rev}} \tag{3.4}$$

where n is the number of electrons transferred (2 for one water molecule), F is the Faraday constant (96,485 C/mol), and E°_{rev} is the reversible cell potential. However, ΔG° only accounts for the electrical energy required to drive the reaction.

To account for the total energy input, both electrical and thermal, the enthalpy change (ΔH°) must be considered, which is 285.84 kJ/mol. The enthalpy change reflects the total energy required to split water, including both the electrical energy and the heat needed to compensate for the entropy change ($\Delta S^\circ = 163.6$ J/mol K). The relationship between these quantities is given by [107]:

$$\Delta G^\circ = \Delta H^\circ - T\Delta S^\circ \tag{3.5}$$

At standard conditions, this yields a thermo-neutral potential (E°_{tn}) of 1.48 V, which is the point where the reaction proceeds without requiring any external heat input or generating excess heat. This potential is higher than the reversible potential due to the entropy change associated with converting liquid water into gaseous hydrogen and oxygen [26].

In practical water electrolysis systems, the operating cell voltage (V_{cell}) is always higher than the theoretical reversible voltage (E_{rev}). This difference is due to several sources of inefficiencies, collectively referred to as overpotentials. The total cell voltage can be expressed as [26]:

$$V_{\text{cell}} = E_{\text{rev}} + V_{\text{act}} + iR_{\text{cell}}$$

where E_{rev} is the reversible voltage, V_{act} represents the activation overpotential, and iR_{cell} accounts for ohmic losses within the system.

Activation overpotential (V_{act}) arises due to the slow reaction kinetics at the electrodes, especially the OER at the anode, which involves a complex multi-step process. This overpotential arises because additional energy is required to overcome the energy barriers of the electrochemical reactions. Activation overpotential shows a logarithmic dependence on current density and can be reduced by improving the catalytic activity of the electrode materials [67, 10].

Ohmic overpotential (iR_{cell}) is caused by resistances to the flow of electrons and ions within the electrolyzer. This term is proportional to the current density and the total cell resistance [94]. The total cell resistance is composed of several resistive elements within the cell, including the resistance caused by the ion-conducting membrane, the resistance within the electrodes themselves, and the contact resistance at the interfaces between different cell components [103]. In addition, mass transport resistance (or concentration overpotential) arises due to the inefficient supply of reactants, such as OH^-, to the catalytic sites and the removal of products, such as oxygen and hydrogen, and is typically the lowest overpotential [67]. Finally, system resistances come also from components like gas diffusion layers (GDLs), bipolar plates, and external circuits that conduct the generated current.

By optimizing materials and minimizing resistances within the cell, the overall efficiency of the electrolysis system can be significantly improved. Additionally, the performance of the electrolysis system is further influenced by temperature and pressure [26]. Increasing the operating temperature reduces the activation overpotential by improving the reaction kinetics and ion transport. Higher temperatures lower the total energy required for the reaction, as seen from the Gibbs free energy relationship. Additionally, raising the pressure slightly increases the reversible voltage [8]. However, higher pressures can provide the advantage of producing compressed hydrogen directly, reducing the need for more expensive external gas compression systems.

Water electrolysis has been investigated since the late 18th century, with initial attempts using electrostatic generators for separating water into hydrogen and oxygen. The technology gained relevance in the 19th century alongside the emergence of electrochemistry. By the mid-20th century, alkaline water electrolysis (AWE) was commercialized to satisfy the increasing need for hydrogen in the chemical sector [125]. Nonetheless, this was quickly eclipsed by the petrochemical industry. The breakthrough of proton exchange membrane (PEM) water electrolysis in the 1960s was a notable progress, enabling the production of high-purity hydrogen [111]. In recent years, anion exchange membrane (AEM) water electrolysis has surfaced as a viable low-cost alternative in alkaline environments. In addition, high-temperature solid oxide electrolysis (SOEC) is being investigated for industrial uses, in environments with sufficient heat. The following section will examine the main types of low-temperature water electrolysis with focus on AEMWE technology.

3.1.2. Types of Water Electrolysis

The three primary types of low-temperature water electrolysis technologies are outlined below. Each technology has distinct characteristics, which are schematically described and compared in table 3.1, offering an overview of their key technical aspects.

Table 3.1: Technical characteristics of water electrolysis technologies [61, 117, 108].

	Alkaline	**AEM**	**PEM**
Anode	$2\,OH^- \rightarrow H_2O + 0.5\,O_2 + 2\,e^-$	$2\,OH^- \rightarrow H_2O + 0.5\,O_2 + 2\,e^-$	$H_2O \rightarrow 0.5\,O_2 + 2\,H^+ + 2\,e^-$
Cathode	$2\,H_2O + 2\,e^- \rightarrow H_2 + 2\,OH^-$	$2\,H_2O + 2\,e^- \rightarrow H_2 + 2\,OH^-$	$2\,H^+ + 2\,e^- \rightarrow H_2$
Electrolyte	KOH/NaOH (5M)	KOH/NaOH (1M)	Solid polymer electrolyte
Charge carrier	OH^-	OH^-	H^+
Separator	Porous inorganic diaphragm	Polymer membrane	Polymer membrane
HER catalyst	Ni-coated perforated SS	Ni	IrO_2
OER catalyst	Ni-coated perforated SS	Ni or NiFeCo alloys	Pt/C
GDL	Ni mesh	Ni foam/carbon cloth	Ti mesh/carbon cloth
Bipolar Plates	SS or Ni-coated SS	SS or Ni-coated SS	Pt/Au-coated Ti or Ti
Current density	200–800 mA/cm^2	200–2000 mA/cm^2	1000–2000 mA/cm^2
Cell voltage	1.8-2.4 V	1.6–2.2 V	1.8–2.2 V
Cell temperature	70–90°C	40–60°C	50–80°C
Cell pressure	25-30 bar	30 bar	30-80 bar
H_2 purity	99.5–99.9%	99.9%	99.9%
Efficiency	50–78%	57–59%	50–83%
Stack lifetime	60,000 h	30,000 h	50,000–80,000 h
Electrode area	10,000–30,000 cm^2	300 cm^2	1,500 cm^2
Capital costs	1000-1200 €/kW	Unknown	1860-2320 €/kW
Status	Mature	R&D	Commercialized

Alkaline Water Electrolysis

Alkaline water electrolysis (AWE) is a well established mature technology for large-scale hydrogen production. It has been commercially implemented since the mid-20th century, and it works with an alkaline medium, KOH or NaOH as the electrolyte (20-30%). The system works at moderate temperatures (70–90°C) and pressures (25–30 bar) and can achieve efficiencies of 50% to 78% [61, 108].

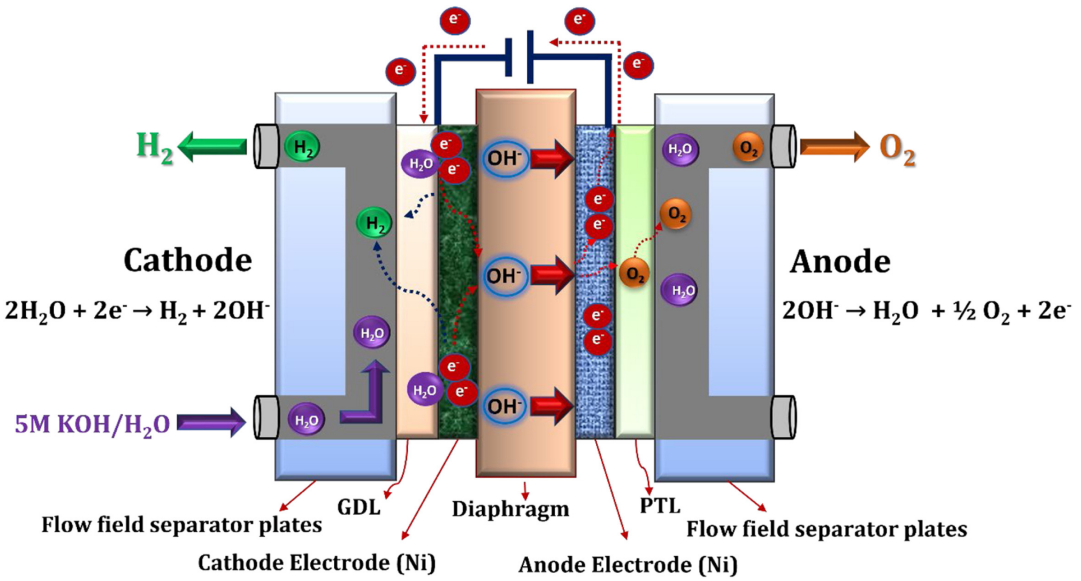

Figure 3.1: Schematic view of alkaline water electrolysis [61].

Figure 3.1 shows a schematic view of this technology. The major components of AWE are nickel-coated stainless steel electrodes for both anode and cathode with a porous diaphragm, often made of materials

like asbestos and ZrO_2, separating them. This diaphragm allows the OH^- ions to pass through while keeping the gases separated. AWE systems typically reach current densities in the range of 200–800 mA/cm^2 and a cell voltage of 1.8-2.4 V [61].

The advantages of AWE lie in its cost-effectiveness, with capital costs around 1000–1200 €/kW, with stack lifetime up to 60,000 hours [108]. The main disadvantages of AWE are the risk of corrosion by concentrated alkaline solutions and reduced purity of hydrogen due to gas crossover.

PEM Water Electrolysis

Water electrolysis by means of PEM represents a widely spread technology for high-purity hydrogen production. It was developed in the 1960s due to the disadvantageous properties of AWE. Operating in an acidic medium, PEM electrolysis uses a solid polymer electrolyte, typically Nafion, to conduct protons (H^+) from anode to cathode. The system works at moderate temperatures (50–80°C) and operates under higher pressures (30–80 bar), achieving efficiencies between 50% and 83%. PEM systems can achieve current densities between 1000 and 2000 mA/cm^2 and operate with a cell voltage between 1.8–2.2 V [61, 108].

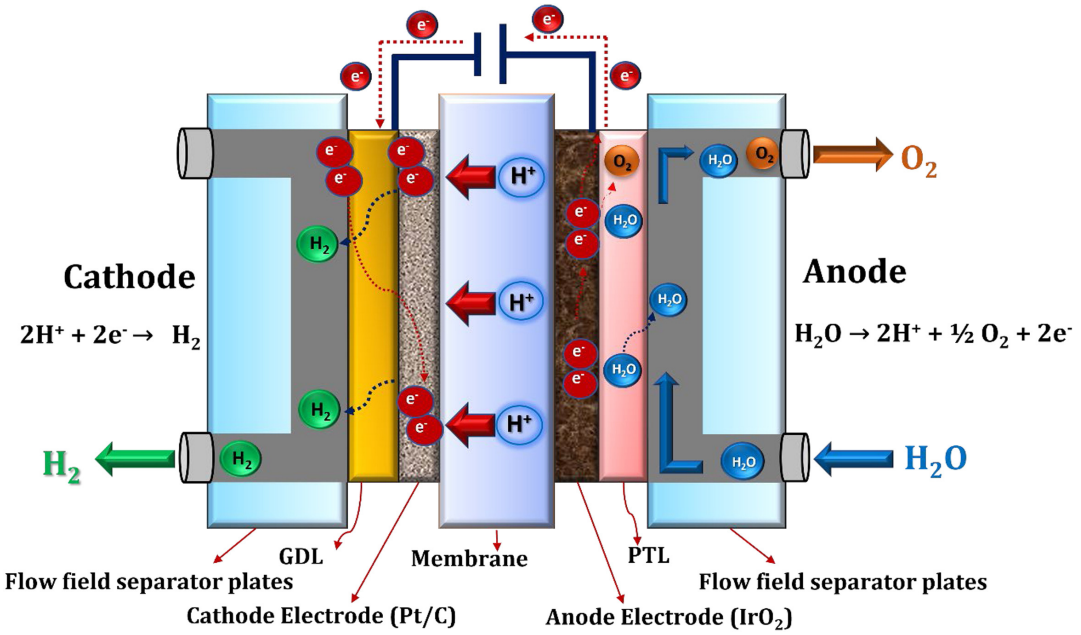

Figure 3.2: Schematic view of PEM water electrolysis [61].

Figure 3.2 shows a schematic view of this technology. The core components of PEM electrolysis include precious metal catalysts, usually Pt at the cathode and IrO_2 at the anode, which facilitate the hydrogen/oxygen evolution reactions. The electrodes are separated by a solid polymer membrane that allows proton transfer while preventing gas crossover. Currently, Nafion 117 is the most used in PEM electrolyzers commercially, with a thickness of 180 µm [57]. Thinner membranes could reduce relevant efficiency losses and improve performance at higher current densities, and are currently being studied. Other polymer membranes, such as Fumapem, Flemion, and Aciplex, have been developed, however their proton conductivity, mechanical, and chemical stability have been found to be lower [61]. In general, these membranes are based on perfluorosulfonic acid (PFSA) polymers, which provide very good chemical resistance with high proton conductivity.

The main advantages of PEM electrolysis are the possibility of producing ultra-high-purity hydrogen, up to 99.9% [117]. PEM electrolyzers allow for higher current densities, a smaller system footprint, and safer operation compared to AWE since PEM systems do not use liquid caustic electrolytes. Moreover, the kinetics of HER is faster owing to the acidic medium and the highly active surface area of Pt-based catalysts.

Yet, PEMWE has some disadvantages concerning the cost of its components: the usage of expensive

precious metals, especially iridium and platinum, significantly raises the capital cost of PEM systems, as these are necessary to withstand the acidic and corrosive environment. Non-precious metals, which are stable in alkaline systems, cannot withstand the acidic conditions of PEMWE while maintaining catalytic efficiency. Additionally, the bipolar plates are made of titanium alloy, mostly coated with either platinum or gold for the gas diffusion layers, and contribute to 48% of the cell cost [61]. The lifetime of PEM systems can be as high as 60,000 hours. To further reduce the cost of PEM electrolysis and simultaneously improve its efficiency, efforts have been made to minimize the thickness of the polymer membrane, optimize the loading of expensive metal catalysts, and find cheaper alternatives for the bipolar plates [61].

AEM Water Electrolysis

AEM water electrolysis appears to be a promising compromise, integrating the advantages of both alkaline and proton exchange membrane electrolysis methods. AEMWE was created as a cost-efficient substitute for these two technologies, functioning in an alkaline environment while using a polymeric anion exchange membrane, enabling a more compact design than the porous diaphragm. This setup enables AEMWE systems to use cost-effective, non-noble metal catalysts for alkaline systems, while benefiting from the small design and efficiency characteristic of PEM systems. AEMWE generally employs a dilute alkaline electrolyte, such as 1M KOH or distilled water, functioning at temperatures of approximately 40 to 60°C and pressures near 30 bar, with efficiencies recorded between 57% and 59% [61, 117].

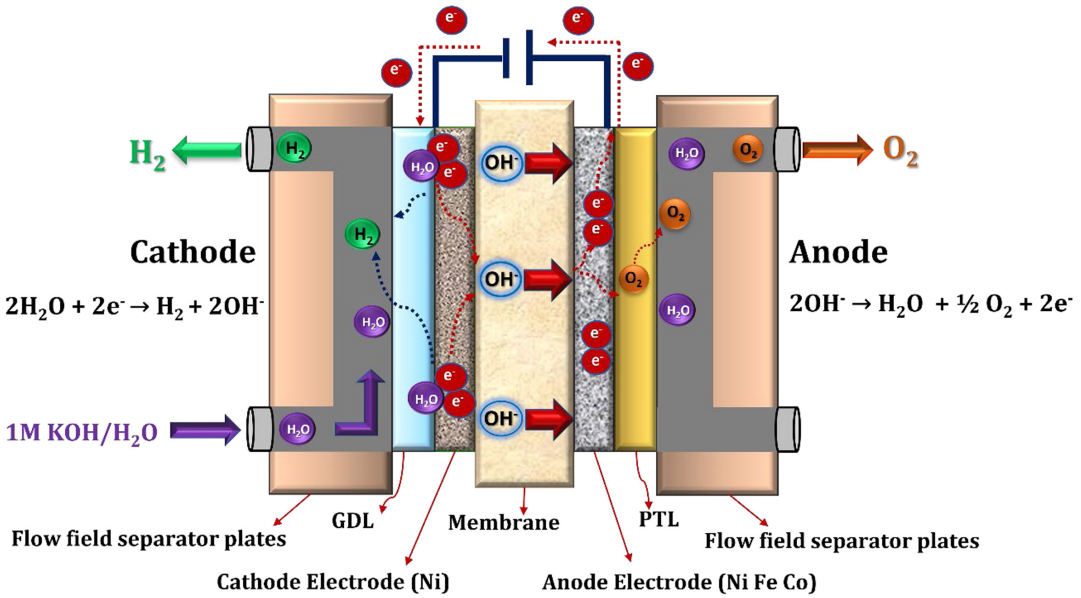

Figure 3.3: Schematic view of AEM water electrolysis [61].

Figure 3.3 shows a schematic view of AEMWE. A key advantage of AEMWE is its potential to utilize inexpensive, non-noble metal catalysts, such as nickel (Ni) at both the anode and cathode. Although this technology theoretically allows for the replacement of costly noble metals, platinum (Pt) and iridium oxide (IrO_x) are still frequently used due to their superior performance. Nonetheless, research is advancing toward improving non-noble catalysts to achieve comparable efficiency. The anion exchange membrane allows hydroxyl ions (OH^-) to pass from the cathode to the anode while preventing gas crossover. AEM systems typically operate at current densities ranging from 200 to 2000 mA/cm^2, with a cell voltage between 1.8 and 2.2 V [61].

The primary advantage of AEMWE is its ability to use less expensive materials, as it allows the replacement of costly noble metal catalysts with more economical transition metals, such as nickel, thereby substantially reducing capital costs. This substitution is feasible because AEMWE operates in a non-acidic, alkaline environment, where transition metals remain stable and effective as catalysts. For large-scale hydrogen production, the noble metals required in PEM systems, such as iridium and plat-

inum, become prohibitively costly due to their high price and limited availability [106]. Furthermore, unlike AWE, AEMWE uses low-concentration electrolytes, which reduces corrosive and handling risks and enhances the durability of the system. Nonetheless, despite these benefits, AEMWE remains in the developmental stage and faces several challenges that must be addressed to compete with PEM and AWE systems. In particular, the reported current densities and operational lifespan of AEM systems are typically lower than those of PEM systems.

Ongoing research to advance AEMWE technology focuses on improving the durability and ionic conductivity of the anion exchange membrane, alongside improving the efficiency of electrodes and catalysts. Key priorities include the development of chemically stable membranes that resist degradation while ensuring optimal ion transport, crucial for reducing ohmic losses and improving overall system efficiency. Additionally, preventing the deterioration of electrodes and catalysts, while optimizing the use of economical materials without sacrificing performance, is crucial to extending system lifetime and ensuring high efficiency. Addressing these technical challenges will make hydrogen production via AEMWE a cost-effective and scalable solution.

Table A.1 in appendix A.1 summarizes the main advantages and disadvantages of different electrolysis techniques.

3.1.3. Improving Anion Exchange Membrane Water Electrolysis

Hydrogen Evolution Reaction (HER)

The hydrogen evolution reaction (HER) is the cathodic half-cell reaction in water electrolysis. In alkaline conditions, the HER mechanism is more complex than in acidic media due to additional steps required for water dissociation [52]. Under acidic conditions, protons are directly involved in the process, resulting in the direct reduction to hydrogen gas (H_2). Under alkaline conditions, the process requires the dissociation of water molecules, hence introducing kinetic barriers.
The reaction occurs via the Volmer step, where water is adsorbed and dissociated [26]:

$$\mathrm{H_2O + e^- + M \longrightarrow M \cdot H + OH^-} \tag{3.6}$$

This is subsequently followed by either the Heyrovsky step:

$$\mathrm{H_2O + M \cdot H + e^- \longrightarrow H_2 + OH^- + M} \tag{3.7}$$

or the Tafel step:

$$\mathrm{2\,M \cdot H \longrightarrow H_2 + 2\,M} \tag{3.8}$$

Due to the high energy needed for water dissociation, the Volmer phase is typically rate-limiting.

Platinum (Pt) is considered the standard catalyst for the hydrogen evolution reaction (HER) in both acidic and alkaline environments due to its ideal hydrogen-binding energy [94]. HER performance is typically shown by a volcano plot, correlating hydrogen-binding energy with catalytic activity, with Pt situated near the peak, making it very effective for hydrogen evolution. In alkaline environments, the performance of Pt is impeded by the sluggish water dissociation during the Volmer stage. Although Pt effectively binds and releases hydrogen, it is comparatively inefficient in facilitating water dissociation, rendering its application less justifiable due to its elevated cost and limited availability. Moreover, to achieve effective HER in alkaline conditions, it is essential to optimize the adsorption energy of OH^- on the catalyst surface to promote swift adsorption and desorption of OH^-, while mitigating competition between OH^- and H^* for active sites [52].

This has driven researchers to explore alternative catalysts, with a focus on developing cost-effective options that can match platinum's performance. Examples include transition metal catalysts such as Ni-based alloys (e.g., NiMo), nanostructured Ni-based materials (e.g., $Ni(OH)_2$ on Pt), NiFe oxides and hydroxides, Mo-based compounds including carbides (Mo_2C), nitrides (Mo_2N), and sulfides, Ru nanoparticles on high-surface-area carbon, transition metal phosphides (e.g., Ni_2P, Co_2P) and nickel and cobalt sulfides [52, 26].

Oxygen Evolution Reaction (OER)

The oxygen evolution reaction (OER) is the anodic half-reaction in water electrolysis and represents a major bottleneck in enhancing the overall efficiency of the system. The OER is a four-electron process involving multiple reaction intermediates, which makes it kinetically slow. The most widely accepted mechanism for OER is the adsorbate evolution mechanism, where hydroxide ions (OH^-) adsorb onto the catalyst surface and proceed through intermediates such as $M \cdot OH$, $M \cdot O$, and $M \cdot OOH$. The reaction progresses as follows [94]:

$$\mathrm{M} + \mathrm{OH}^- \longrightarrow \mathrm{M} \cdot \mathrm{OH} + \mathrm{e}^- \tag{3.9}$$

$$\mathrm{M} \cdot \mathrm{OH} + \mathrm{OH}^- \longrightarrow \mathrm{M} \cdot \mathrm{O} + \mathrm{H_2O} + \mathrm{e}^- \tag{3.10}$$

$$\mathrm{M} \cdot \mathrm{O} + \mathrm{OH}^- \longrightarrow \mathrm{M} \cdot \mathrm{OOH} + \mathrm{e}^- \tag{3.11}$$

$$\mathrm{M} \cdot \mathrm{OOH} + \mathrm{OH}^- \longrightarrow \mathrm{M} + \mathrm{O_2} + \mathrm{H_2O} + \mathrm{e}^- \tag{3.12}$$

In acidic environments, noble metal oxides like IrO_2 and RuO_2 are commonly used due to their stability in highly oxidative and highly corrosive conditions [94]. In contrast, the low-concentration alkaline media offers a less corrosive environment than acidic conditions, which enables the use of transition metal-based catalysts such as nickel (Ni), cobalt (Co), and mixed-metal oxides or layered double hydroxides (LDHs) like $\mathrm{NiFeOxHy}$ [26]. Although AEMWE research still frequently uses IrO_2 due to its superior performance, the potential to replace noble metals with more economical, stable non-noble metals in alkaline environments drives research efforts to reduce costs. Ni-based catalysts, in particular, combine cost-effectiveness with high catalytic activity and stability in alkaline conditions.

The oxidative environment, however, can still cause catalysts to undergo changes in valence state. For example, a nickel-based catalyst might oxidize from Ni(II) to Ni(III) or higher [52]. While controlled oxidation can form highly active oxyhydroxides, such as NiOOH, excessive or uncontrolled oxidation may still degrade the catalyst over time.

Beyond conventional adsorbate mechanisms, the lattice oxygen mechanism (LOM) has gained attention for bypassing scaling relationships between $M \cdot OH$ and $M \cdot OOH$ adsorption energies [94]. By allowing lattice oxygen atoms to participate, LOM reduces overpotentials and boosts efficiency. Perovskite oxides (complex metal oxides with a specific crystal structure) have shown enhanced OER activity under this mechanism [52].

Researchers are also exploring the effects of magnetic fields on ferromagnetic OER catalysts like $CoFe_2O_4$, as magnetic fields may influence electron spin and mass transport, enhancing reaction kinetics through faster electron transfer and reduced energy barriers [52].

Membrane Electrode Assembly and Other Aspects

The Membrane Electrode Assembly (MEA), which combines the catalyst layers and the anion exchange membrane (AEM), is essential for improving the overall performance of AEMWEs. A primary concern of MEA research is the enhancement of the triple-phase boundary within the catalyst layer, where gaseous (H_2 or O_2), liquid (OH^-), and solid catalyst phases converge [26]. The efficiency of this boundary directly impacts electrochemical activity. Good gas diffusion guarantees the swift removal of gas bubbles generated at reaction sites, while proper ion transport enables the transit of OH^- ions through the catalyst layer, thereby advancing the electrochemical reactions [94].

Recent developments have focused on integrating Anion Exchange Ionomers (AEIs) into the catalytic layer to facilitate ionic channels for OH^- transport [38]. AEIs increase the conductivity of OH^- ions and serve as binders, hence improving the mechanical and chemical stability of the catalytic layer [78]. Finding the optimal balance in AEI concentration is crucial: large quantities might obstruct catalytic sites, whereas inadequate AEI reduces ion transport. Moreover, the similar chemical composition of AEI and AEM reduces interfacial resistance and mitigates mechanical stress from differential swelling, which

could otherwise impair performance over time. Achieving an optimal AEI content, typically between 5% and 20%, is essential to maintaining both ionic conductivity and long-term durability [26]. These settings, however, must be empirically tuned for particular configurations.

The method of catalyst application significantly influences MEA performance. Two commonly used techniques are Catalyst-Coated Membranes (CCM) and Catalyst-Coated Substrates (CCS) [52]. CCMs enhance interfacial contact between the catalyst and membrane, hence lowering resistance; yet, they may be susceptible to ionomer breakdown with time. Conversely, CCS approaches enhance mechanical stability but may increase the distance between the catalyst and membrane.

Efficient electrolyte selection, gas crossover management, and CO_2 contamination mitigation are additional key areas for enhancing AEMWE performance. While KOH electrolytes provide high ionic conductivity, they can degrade membranes and catalysts over time. In contrast, pure water as an electrolyte improves material stability but limits OH^- availability and has lower conductivity, requiring advanced membrane and ionomer designs to maintain adequate OH^- transport and reaction rates [26]. Gas crossover at high current densities reduces efficiency and poses safety risks, prompting research into selective membranes with improved gas separation properties [26]. Additionally, CO_2 contamination from ambient air or impurities in feed gas form carbonate (CO_3^{2-}) and bicarbonate (HCO_3^-) species, which reduce ionic conductivity and block catalytic sites, ultimately lowering efficiency [94]. Research into CO_2-resistant catalysts and membranes aims to enhance AEMWE system durability by addressing these issues.

Anion Exchange Membrane (AEM)

The anion exchange membrane (AEM) can be regarded as the heart of the AEMWE system and a major bottleneck in achieving optimal performance [74]. AEMs are primarily responsible for conducting hydroxide ions (OH^-) from the cathode to the anode, but they also play crucial roles in water management, gas separation, and maintaining the overall structural integrity of the cell.

In contrast to PEMs, which transport protons (H^+) in acidic environments, AEMs operate in alkaline conditions and must transport the larger hydroxide ions (OH^-). Unlike PEMs, which often rely on perfluorinated polymers with associated environmental and supply chain concerns, AEMs avoid these materials, making them more environmentally friendly and potentially more scalable for large-scale applications [106]. However, the greater size of OH^- ions presents a primary challenge for AEMs, as their transport is harder than that of protons. Additionally, OH^- conduction requires greater hydration and encounters higher ionic drag, further reducing ionic conductivity compared to PEMs [120]. The alkaline environment also creates chemically harsh conditions for AEMs, complicating long-term durability and stability.

The development of AEMs is still in its early stages, and current materials face significant obstacles, including low OH^- conductivity, chemical degradation, and mechanical instability. Overcoming these hurdles is essential, as improvements in AEM technology could greatly enhance the efficiency, durability, and overall cost-effectiveness of AEMWE systems. As a result, substantial research efforts are dedicated to advancing AEM development.

While the previous sections outlined other key research areas and potential improvements for the AEMWE system, this thesis will now focus more deeply on the AEM as a central component. A detailed analysis of AEMs is essential, as this research aims to optimize the performance of a poly(co-aryl piperidinium) AEM, specifically for enhanced conductivity and mechanical properties. The following sections will cover the theoretical background, material considerations, and various strategies currently being investigated to address the challenges in AEM development.

3.2. Anion Exchange Membrane

AEMs are core components of AEMWE systems, directly influencing both performance and lifespan. Their primary function is to facilitate the selective transport of hydroxide ions from the cathode to the anode. Their performance is highly dependent on their material composition and structure, with key parameters including ion transport efficiency, mechanical and thermal stability, long-term durability, and chemical resistance in alkaline environments [94]. Current research is focused on optimizing the composition and structure of these materials to achieve an ideal balance of properties. Beyond their role in AEMWEs and AEMFCs, these materials are also being explored for applications in other fields such as electrodialysis for water desalination and wastewater treatment, redox flow batteries for energy storage, carbon capture technologies, and electrochemical CO_2 reduction [39]. The wide range of potential applications has driven an increased demand for advanced AEM materials. This section discusses the materials used in AEMs, their ion transport mechanisms, degradation processes, and methods for enhancing their performance.

AEMs are made of anion exchange polymers (AEPs), which consist of cationic headgroups attached to polymer backbones. Several key parameters define the performance of AEMs, including ion exchange capacity (IEC), ion conductivity (targeted at least 100 mS/cm at 60°C [74]), chemical stability in alkaline media, mechanical stability, ability to prevent gas crossover, and long-term durability to ensure the extended lifespan of AEMWE systems.

3.2.1. Backbone and Cation Groups

As already mentioned, AEMs are composed of two key elements: the polymer backbone and the cationic groups. A simplified view might suggest that the cationic headgroups are responsible primarily for IEC, ionic conductivity, and chemical stability, while the polymer backbone contributes to mechanical and thermal stability. However, the overall performance of the AEM depends on the integrated structure of the AEPs [26]. Striking the right balance between these properties is essential in the development of high-performance AEMs capable of operating efficiently in alkaline conditions while maintaining structural integrity over time.
One of the most significant obstacles faced by AEMs is degradation in alkaline conditions. This instability results from the vulnerability of the polymer backbones and cationic headgroups. For this reason, this section will also mention degradation mechanisms.

Cation Groups

Commonly used cations in AEMs are reported in figure 3.4.

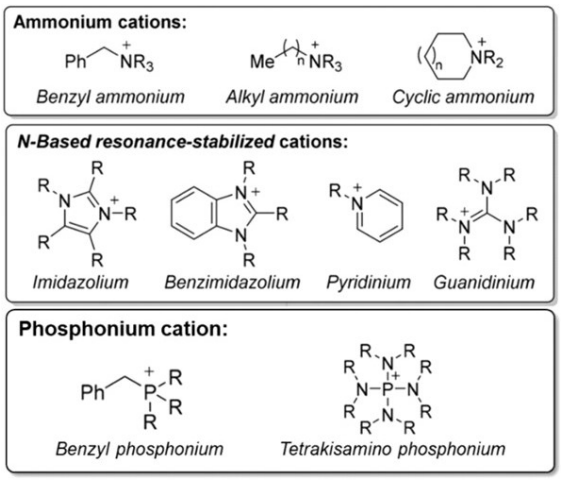

Figure 3.4: Commonly used cations for AEM [66].

Cationic functional groups are prone to Hofmann elimination and nucleophilic substitution (SN2) reactions [46], as illustrated in figure 3.5. Hofmann elimination occurs when a hydroxide ion abstracts a β-hydrogen from the carbon adjacent to the nitrogen in the cationic headgroup, leading to the formation

of an alkene, water, and detachment of the cationic group [46]. In highly alkaline environments and at elevated temperatures, this process is favored. The availability of β-hydrogens makes quaternary ammonium groups, such as trimethylammonium (TMA), very susceptible to Hofmann elimination [94]. In contrast, cyclic cations, including imidazolium and piperidinium, are protected by their ring structure, which reduces the likelihood of Hofmann elimination, despite the presence of β-hydrogens [74].

SN2 substitution occurs when hydroxide ions attack the nitrogen atom or α-carbon in the cationic headgroup, leading to cleavage of the N-C bond and forming alcohols or amines [46]. Imidazolium-based cations are resistant to Hofmann degradation but can still undergo ring-opening reactions through SN2 attacks at the C2 position [74]. Piperidinium-based cations, while more stable than open-chain quaternary ammonium groups, are less resistant than aromatic imidazolium cations. Phosphonium cations, especially those with bulky substituents, offer enhanced stability due to reduced susceptibility to both Hofmann elimination and nucleophilic substitution. Nevertheless, nitrogen-based cations continue to be favored due to their ease of synthesis, ability to integrate into polymer backbones, and the frequent higher initial ion conductivity [26].

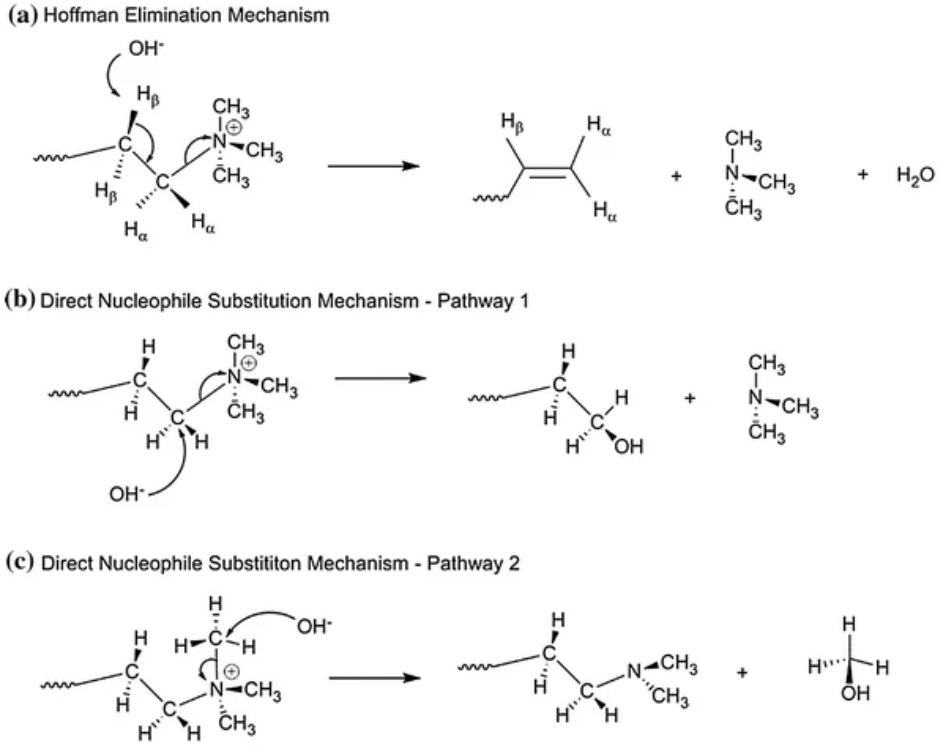

Figure 3.5: Hofmann elimination (a) and Nucleophilic substitution (b) (c) mechanism examples [46].

In order to mitigate these degradation mechanisms, researchers have concentrated on the development of cations with minimal or no β-hydrogens, such as N-spirocyclic ammonium groups, or the use of cyclic cations with geometric constraints that restrict degradation [74]. Additionally, the cation can be protected from nucleophilic attacks by introducing steric hindrance through the addition of bulky groups such as methyl, butyl, or phenyl substituents [26]. Increasing electron density around the cation using electron-donating groups, such as alkyl or aryl (aromatic) chains, further improves resistance to hydroxide ion attacks by reducing the electron deficiency of the cationic center [26].

Polymer Backbones

Commonly used polymer backbones in AEMs are reported in figure 3.6.

In terms of polymer backbones, nucleophilic attack typically targets electron-deficient sites, such as C-O bonds in aromatic ethers [46]. In fact, backbones such as poly(phenylene oxide) (PPO), polysulfone (PSF), and poly(ether ether ketone) (PEEK) are particularly susceptible to this degradation

mechanism [74]. Although backbones with aromatic ether linkages were initially popular due to their excellent mechanical strength, thermal stability, and ease of functionalization, their chemical instability in alkaline environments has led to their gradual replacement by newer AEM designs. Additionally, SN2 nucleophilic attack can occur at quaternary carbon sites that are directly attached to the cationic nitrogen within the polymer backbone, not just in side chains, leading to the formation of alcohols and the breakdown of the cationic group and backbone [46].

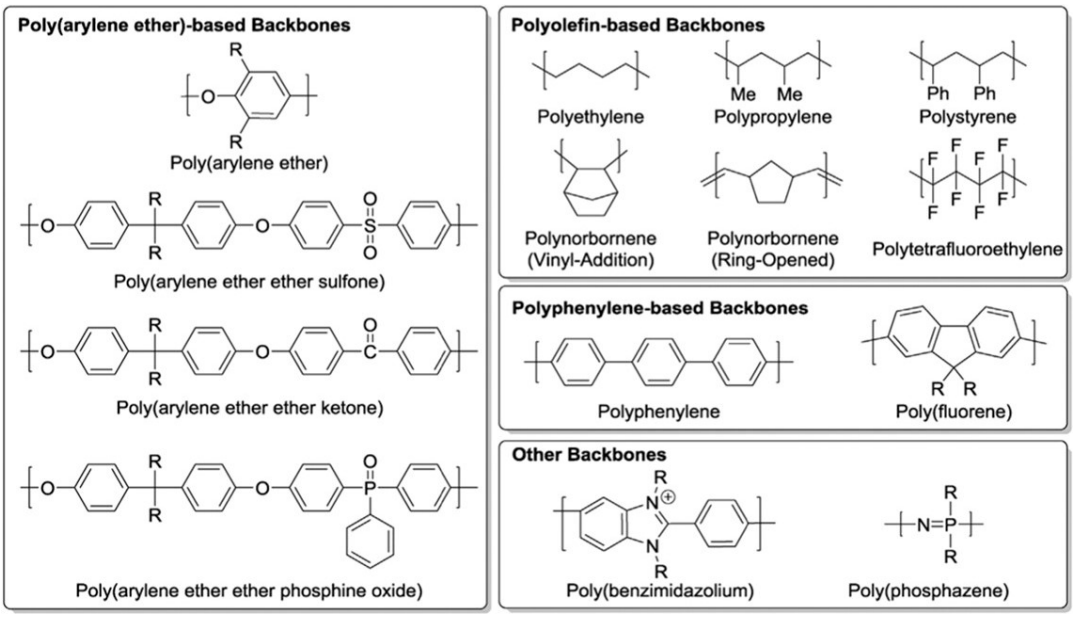

Figure 3.6: Commonly used backbones for AEM [66].

The development of ether-free backbones, such as polyarylene (aromatic), polyfluorene (polycyclic aromatic), and polyolefin (composed of carbon-carbon single bonds), has been one method of mitigating backbone degradation [26]. These backbones lack weak C-O bonds and provide enhanced resistance to nucleophilic attack.

It is essential to take into account the impact on mechanical properties when modifying the chemical structure of AEMs to increase their resistance to alkaline degradation. The chemical stability of the polymer backbone can be enhanced by the incorporation of flexible alkyl side chains or spacers, which introduce steric hindrance and donate electron density to the cationic centers [26]. And this process also increases membrane flexibility. This flexibility helps avoid overly rigid structures that could become brittle or prone to cracking under mechanical stress. It enables the membrane to more effectively withstand swelling, thereby minimizing the likelihood of mechanical damage. However, this approach presents a trade-off: while increased flexibility may reduce the likelihood of mechanical failure, it can also result in excessive water absorption or swelling. Excessive swelling can accelerate chemical degradation by exposing more of the polymer to hydroxide ions and can also damage adjacent catalysts. Therefore, careful optimization is required to balance these properties.

3.2.2. OH- Conduction Mechanism

There are two major mechanisms of OH^- ion conduction in AEMs: vehicular transport and the Grotthuss mechanism. However, the scientific community is still uncertain about the details of OH^- transport [114]. A representation of OH^- conduction is shown in figure 3.7.

In vehicular transport, OH^- ions diffuse through water-filled channels formed by hydration shells along the cationic groups in the membrane, as they attract water molecules into localized hydration zones [11]. As hydration increases, these zones overlap, creating a well-connected network of water molecules, allowing OH^- ions to diffuse while retaining their hydration shell. This mechanism is highly dependent on the polymer structure because the formation and connectivity of the water channels are influenced by how the polymer backbone and distribution of cationic sites organize the water uptake [52].

The Grotthuss mechanism involves the transfer of charge through a hydrogen-bond network. In this process, OH^- ions accept protons from nearby water molecules, converting into H_2O, while the donating water molecule becomes the new OH^- [68]. This allows the charge to propagate without the physical movement of the OH^-. This mechanism is less significant for OH^- ions compared to protons because these anions are larger and more strongly hydrated, making it harder for them to move freely without dragging water molecules. However, it gains importance at higher hydration levels [52].

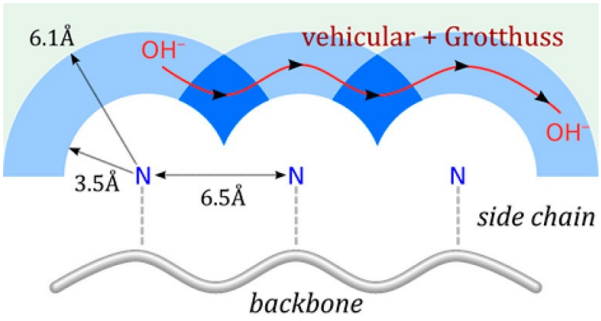

Figure 3.7: Schematic of the mechanism for OH^- transport [11].

OH^- ion conduction is influenced by a variety of factors, such as temperature, water uptake, and the overall structure of the polymer [68]. While higher IEC offers more cations for ion conduction, it can cause too much water absorption and swelling, therefore compromising membrane integrity. Because of their kinetic energy, elevated temperatures increase ion mobility, while also accelerating processes of degradation from nucleophilic substitution and Hofmann elimination. It is essential to achieve the appropriate equilibrium between hydrophilic domains and hydrophobicity in the polymer structure in order to fabricate pathways or channels for efficient OH^- transport while preserving mechanical stability.

3.2.3. Properties of AEM

As previously mentioned, several key parameters define the performance of AEMs. The membranes must efficiently conduct hydroxide ions, prevent gas crossover and maintain chemical and mechanical stability in alkaline media over prolonged periods.

- **Ion exchange capacity** (IEC) refers to the number of ion-exchange sites available in the membrane, typically measured in milligrams per gram of dry polymer [121]. The ion conductivity of the membrane increases with rising IEC. However, at high IEC levels, excessive water uptake can cause swelling, reducing conductivity and mechanical instability [74]. Therefore, balancing the IEC is crucial to maximize conductivity without compromising the membrane's mechanical and chemical integrity.
- **Water uptake** (WU) is essential for maintaining hydration and facilitating ion transport in AEMs. However, excessive WU can lead to swelling, compromising both the mechanical stability and chemical resistance of the membrane. WU and the **swelling ratio** (SR) are influenced by factors such as the number of conducting groups and the elasticity of the polymer [50]. A balance between hydration and mechanical integrity is required to prevent excessive swelling, which may lead to mechanical damage and chemical degradation.
- **Ion conductivity** is a key performance metric for AEMs, directly influencing the current density produced by the system. High conductivity is critical for efficient OH^- conduction and is at the moment targeted at a value of at least 0.1 S/cm at 60°C [74]. Conductivity depends on IEC, water content, and the polymer's ability to efficiently form water-filled channels that facilitate ion transport [11]. The conductivity measured in AEMs is through-plane, meaning it refers to the current flowing perpendicularly to the plane of the membrane.
- **Mechanical integrity** is essential to ensure that AEMs can withstand operational stresses such as swelling, temperature fluctuations, and physical wear [121]. As seen, increasing IEC can lead to excessive water uptake and membrane swelling. A flexible membrane can reduce the risk of fractures. On the other hand, membranes that are too rigid may become embrittled due to de-

hydration. Striking a balance between rigidity and flexibility is essential for long-term mechanical stability.

- AEMs must maintain **thermal stability** at operational temperatures, around 60°C, to prevent degradation. High temperatures improve ion mobility, enhancing conductivity, but also accelerate degradation processes such as Hofmann elimination and nucleophilic substitution, posing a challenge to both chemical and mechanical integrity.
- AEMs must prevent **gas crossover** between the anode and cathode compartments. Gas crossover not only reduces system efficiency by losing pure hydrogen, and limiting OH- passage, but it also poses safety risks, especially when the hydrogen concentration in oxygen exceeds 4% [26]. The membrane must act as an effective barrier to gas flow while allowing sufficient ion transport. In general, H_2 molecules are smaller and more likely to pass through the membrane compared to O_2, so minimizing hydrogen crossover is a primary focus in membrane design.
- **Chemical and alkaline stability** are critical for the long-term performance of AEMs. As seen earlier, the cationic headgroups and polymer backbone must resist alkaline degradation mechanisms for ensuring the durability of the AEM over time.

3.2.4. Commercially Available Membranes

Table 3.2 summarizes key parameters of the main commercially available AEMs. Additionally, appendix A.2 includes a table that summarizes various research studies on AEMWE, detailing combinations of catalysts, membranes, and the resulting current densities [66].

Company	Membrane	IEC (mmol/g)	Ion conductivity (mS/cm)	Thickness (µm)
Dioxide Materials	Sustainion 37-50	1.2	80 (1M KOH)	50
Fumatech	FAA-3-30	1.67–2.04 (Cl)	>5	26–34
	FAA-3-50	1.6–2.1 (Cl)	3–8 (Cl)	45–55
	FAA-3-PK-75	1.2–1.4 (Cl)	4.5–6.5 (Cl)	70–80
Ionomr	AF1-HNN5-25	1.4–1.7 (OH)	56 ± 1(OH)	25
	AF1-HNN5-50	1.4–1.7 (OH)	40 ± 2(OH)	50
	AF1-HNN8-25	2.1–2.5 (OH)	131 ± 1(OH)	25
	AF1-HNN8-50	2.1–2.5 (OH)	102 ± 3(OH)	50
Tokuyama	A201	1.7 (OH)	42 (OH)	28
	A901	1.7 (OH)	38 (OH)	10
Versogen	PiperION-A-20	2.35	150 (OH)	20
	PiperION-A-80	2.35	150 (OH)	80
Orion	TM1	2.19 (OH)	>60 (OH)	30

Table 3.2: Commercial AEMs and key parameters [66].

3.2.5. Improving AEM

As described, the design of high-performance AEMs is challenged by the complicated interaction of ion exchange capacity, water absorption, mechanical integrity, and chemical stability, but reaching the ideal balance between these is quite crucial. Researchers are developing many approaches targeted at improving AEM, minimizing the trade-off between ion conductivity and mechanical strength while guaranteeing long-term stability in alkaline conditions. This section explores the most prominent strategies in literature.

Cross Linking

Cross-linking has been thoroughly investigated as an improvement strategy for AEMs. This method allows increasing IEC while preserving mechanical stability through the formation of cross-linked networks. The method involves making chemical or physical bonds between polymer chains, thus restricting membrane swelling [74]. Physical cross-linking is based on interactions like ion-ion or van der Waals forces, whereas chemical cross-linking requires the formation of covalent bonds by reactive agents. For instance, a cross-linked poly(fluorenyl-co-terphenyl piperidinium) exhibited a modest enhancement in ionic conductivity attributed to increased IEC, while maintaining an acceptable swelling ratio due to the constraints imposed by crosslinking [16]. Another study on a ply(aryl-co-aryl-piperidinium) with

styrene crosslinks has shown constant ion conductivity with a sharp decrease in swelling ratio, increasing mechanical properties of the membrane [15]. However, cross-linking requires careful optimization. Excessive cross-linking (e.g., using long-chain cross-linkers) can lead to excessive crystallinity in the AEM, diminishing hydrophilicity and ion mobility. As shown for of poly(2,6-dimethyl-1,4-phenylene oxide) (PPO) and hydrophilic cross-linkers containing ethylene oxide, that led to excessive enhancement in crystallinity and diminished ionic conductivity and alkaline stability [26]. Additionally, it was reported that styrene-crosslinked PFTP performed worse than regular PFTP [16]. If cross-linking is too strong, it can lead to mechanically brittle AEMs. Additionally, excessive reaction steps complicate membrane processing.

Phase Separation

Microphase separation has emerged as an effective approach for improving the ion conductivity of AEMs while simultaneously maintaining mechanical stability. In this strategy, the polymer is designed to form distinct hydrophilic and hydrophobic domains, where the hydrophilic regions act as continuous channels for OH^- transport. These regions ensure efficient ion conduction, while the hydrophobic domains control excessive water uptake and reduce swelling, preserving mechanical integrity [124]. AEMs are typically divided into three main structures with different mechanisms for phase separation.

- In **dense functional group** AEMs, cationic functional groups are concentrated in specific segments or structural units, forming polar clusters that create pathways for OH^- ions. However, dense clustering often leads to poor alkaline stability due to nucleophilic attack.
- **Side chain** AEMs have flexible alkyl spacers between the polymer backbone and ion conducting groups, allowing for well defined microphase separated structures. This is because short spacers do not often offer enough mobility for ion exchange groups to form efficient ionic pathways. On the other hand excessively long spacers are too hydrophobic, reducing OH^- conductivity. As an example, side chain type PPO AEMs with varying alkyl spacer lengths demonstrated significantly higher OH^- conductivity, reaching 99.5 mS/cm at 80°C due to the well defined phase separated morphology [74]. Another studied reported a 50% decrease in swelling ratio thanks to the side hydrophobic chains, accompanied by an increase in ion conductivity in a PFBP-FLN polymer. The same study on PFTP-FLN polymer with side chains, though, reported a decrease in conductivity and similar swelling ratio [51]. The results are in fact highly dependent on the specific polymer.
- Finally, **block copolymer** AEMs consist of segments with distinct chemical compositions and properties that direct phase separation between chemically distinct domains. Similar segments cluster together, forming a well-structured network [74]. Hydrophilic segments form ion-conducting channels, while hydrophobic segments provide structural support. For instance, a block copolymer AEM with fluorenyl groups led to an ion conductivity of 144 mS/cm at 80°C, achieving nearly three times the performance of the same polymer with similar IEC without fluorenyl groups [14].

Casting Methods

Alongside traditional solution casting, novel casting techniques are being studied as strategies for improving AEMs by adjusting their structure and ion transport pathways.

- **Electric field** assisted casting is one approach that has been researched with the purpose of enhancing AEM structural alignment. Applying an electric field during the casting process promotes the alignment of polymer chains and functional groups, allowing more efficient ion transport through the structured channels [104]. A study on quaternary-aminated poly(2,6-dimethyl-1,4-phenylene oxide) (QPPO) revealed that electric field treatment enhanced the membrane's ionic conductivity from 0.06 S/cm to 0.12 S/cm at 20°C, attributed to the improved alignment of ion-conducting channels [59].
- Among the novel casting techniques that have recently attracted interest is **electrospinning**. This technique produces nanofibers with a high surface area and a structured nanostructure, facilitating the development of continuous ion-conducting channels [101]. A polymer solution is expelled from a syringe at high voltage, stretching into thin fibers that solidify upon solvent evaporation, resulting in a nanofiber mat on a grounded collector. Electrospun QPPO membranes exhibited a conductivity of 51.5 mS/cm at 60°C, more than doubling the conductivity of traditionally cast QPPO membranes (20.3 mS/cm) at similar IEC values [28].

Fillers
The use of inorganic fillers is another possibility which offers substantial promise for improving AEM performance. Composite membranes can be prepared by incorporating particles, for example, graphene oxide (GO) or carbon nanotubes (CNTs), resulting in enhanced ion conductivity and better mechanical/thermal stability. These fillers form highly conductive nanoclusters within the membrane and modulate membrane swelling [74].
One of the drawbacks of inorganic fillers, however, is that they can tend to aggregate, especially at higher filler levels. Aggregated fillers results in structural defects within the membrane, blocks anion transport, and reduces mechanical strength, increasing chances of pore formation and H_2/O_2 gas crossover. As a result, optimizing filler content is critical to maintaining the strength and performance of composite membranes.

3.2.6. Fillers

The incorporation of inorganic fillers into AEMs has gained significant attention as an approach to enhance ionic conductivity, mechanical strength, thermal resistance, and chemical durability. Despite the promising potential of fillers for AEMs, this strategy is relatively recent, becoming a major research focus only within the last decade [87]. The effect of fillers on AEM performance is highly dependent on their interaction with the polymer matrix, making it challenging to generalize their impact. A more detailed understanding of how different fillers interact within specific polymer systems is essential to optimize composite membranes for anion exchange water electrolysis application.

Fillers can enhance ion transport by improving ion-conducting channels, creating localized regions that facilitate ion movement [74]. For example, materials like graphene oxide (GO) and functionalized carbon nanotubes (CNTs) can form well-organized hydrophilic nanostructures that facilitate the efficient movement of ions. Some fillers, particularly those with intrinsic ionic conductivity, such as layered double hydroxides (LDHs) and zeolites, contribute directly to ion transport within the membrane. While inert fillers, such as silica and alumina, may primarily serve a reinforcing role, enhancing mechanical properties [87]. Fillers themselves should be highly stable in alkaline environments. For example, materials like silica and alumina may degrade or lose effectiveness in highly alkaline conditions [26]. Additionally, fillers can improve the long-term alkaline stability of AEMs through physical cross-linking (e.g., acid-base interactions, hydrogen bonding, van der Waals forces, and electrostatic interactions) or by inducing partial crystallization near the filler particles, which enhances mechanical integrity and reduces membrane swelling, and up to a point also increases ion conductivity [87].

However, the addition of fillers presents several challenges. One of the most significant is aggregation at high filler concentrations, which can cause structural defects that block ion transport pathways, reduce mechanical strength, and lead to gas crossover in applications such as water electrolysis [87]. To optimize membrane performance, it is crucial to find the right filler concentration, sufficient to enhance properties without causing aggregation. Compatibility between the filler and the polymer matrix is also critical. More compatible fillers allow for higher loadings before aggregation occurs, while less compatible fillers tend to agglomerate at lower concentrations, limiting their benefits. Functionalizable fillers like GO are especially attractive because they can be chemically modified to integrate more effectively with the polymer, allowing for higher loadings and improved dispersion [87].

Cost is another important factor when considering fillers. Advanced materials like CNTs can be expensive, and their advantages must be balanced against the overall costs. Optimizing filler content to achieve maximum performance while controlling costs and preventing agglomeration is essential for creating effective and economically viable composite membranes.

In addition, the end application of the composite membrane must be carefully considered when selecting fillers. While many inorganic fillers possess electrical conductivity, this property can be detrimental in certain applications, such as water electrolysis and fuel cells, where conductive fillers may cause short-circuiting by providing unintended electronic conduction pathways that bypass the electrochemical reactions, compromising the system's overall performance [37, 41].

Fillers can be classified according to their dimensionality: 1D, 2D and 3D materials [87]. Each type of fillers interacts differently with the polymer matrix, and the effectiveness of these fillers depends largely on how well they are integrated into the membrane structure. The dimensionality affects the surface

area, the formation of ion-conducting channels, and their role in reinforcing mechanical properties. Following are listed the main fillers reported in literature used for improving AEMs.

1D Fillers

1D fillers are characterized by their long, narrow structure, which offers a high aspect ratio. These materials form extended pathways that can improve ion conduction and provide mechanical strength to the membrane.

- **Carbon Nanotubes** (CNTs) are cylindrical structures composed of carbon atoms organized in a hexagonal lattice, in single-walled (SWCNTs) or multi-walled (MWCNTs) configurations. Functionalized CNTs (f-CNTs), which can be modified with groups like carboxyl, hydroxyl, or amino groups, enhance compatibility with the polymer matrix, improving dispersion and preventing agglomeration. Their tubular structure facilitates ion movement by aligning along the membrane surface, creating direct pathways for ion conduction [87]. CNTs are known for their excellent mechanical properties, including high tensile strength and flexibility, which reinforce composite membranes while preserving flexibility [87]. For example, incorporating imidazolium-functionalized CNTs into an Im-PEEK membrane resulted in ion conductivity of 135 mS/cm at 70°C, compared to 80 mS/cm for the pure polymer [98].
- **Titanate Nanotubes** (TNTs), like CNTs, are 1D fillers made of titanium dioxide in a tubular form. This tubular structure promotes ion conduction along the tube axis, similar to CNTs [87]. TNTs are well-known for their stability in alkaline environments, which is crucial for maintaining membrane performance under harsh conditions. Functionalizing TNTs with groups like amines or carboxyl groups improves compatibility with the polymer matrix, enhancing both mechanical strength and dimensional stability. For instance, incorporating titanate nanotubes into a QPSU matrix for fuel cell applications at a 5 wt% loading increased conductivity to 21 mS/cm at 30°C and improved tensile strength to 43 MPa [32].

2D Fillers

2D fillers are planar materials with high surface areas, facilitating the formation of interconnected, structured ion-conducting structures within the membrane [87].

- **Graphene Oxide** (GO) is a functionalized derivative of graphene that incorporates oxygen-rich functional groups, including hydroxyl, carboxyl, and epoxy groups. These functional groups help creating hydrophilic domains inside the polymer matrix, therefore enhancing the transport of hydroxide ions (OH^-) [41]. The functionalization enhances the dispersibility of GO, preventing its aggregation and maintaining a uniform distribution within the polymer matrix [87]. This functionalization is based on enhancing the interaction between the polymer matrix and the GO, so it should be tuned for each specific case. GO has been extensively studied in AEMs, with improvements in both ion conductivity and mechanical properties. For example, imidazolium-functionalized graphene oxide (Im-GO) was incorporated into a PSF membrane, resulting in a conductivity of 22.02 mS/cm, over twice that of the pristine polymer, while simultaneously decreasing water uptake and the swelling ratio [77].
- **Layered Double Hydroxides** (LDHs) are 2D materials made of metal hydroxide layers with intercalated anions. The intrinsic ionic conductivity of LDHs results from the mobility of the intercalated anions, and the stratified architecture facilitates pathways for ion transport, making them advantageous for ion transport [87]. LDHs also serve as mechanical reinforcements, enhancing stability and controlling membrane swelling. A mixed polymer QCS/PVA, infused with LDH, attained a conductivity of 47 mS/cm, in contrast to 29 mS/cm for the unmodified polymer [43].

3D Fillers

3D fillers enhance mechanical reinforcement and thermal stability, and unlike 1D and 2D fillers, are primarily used to improve structural integrity rather than ion conductivity [87].

- **Silica** (SiO_2) and **Alumina** (Al_2O_3) are commonly utilized as inert fillers to improve stiffness and dimensional stability. They have been reported to improve mechanical properties and decrease swelling when added to membrane matrices [87]. Nevertheless, these fillers might lose their efficacy or deteriorate in highly alkaline environments [26]. A Young's modulus of 2250 MPa was achieved when silica (SiO_2) particles were distributed in a QPSU matrix at 20 wt% [72].

- **Zirconia** (ZrO_2) is a filler with superior chemical stability and remarkable resistance to alkaline degradation. In contrast to alumina and silica, it does not deteriorate even when exposed to extremely high pH levels [26]. By acting as nucleation sites in the polymer matrix close to the filler particles, zirconia nanoparticles can cause partial crystallization, which improves mechanical integrity, and, up to a point, ion conductivity [87]. For instance, at 50°C, the conductivity of zirconia-dispersed Im-PSU membranes was improved to 80 mS/cm, more than that of Im-PSU [102].
- **Metal-Organic Frameworks** (MOFs) are porous 3D materials created by coordinating metal ions with organic ligands. Because of their highly porous nature and adjustable pore structure, they are promising candidates for tuning ion transport in AEMs facilitating ion mobility across their porous framework, and providing mechanical reinforcement [87]. The conductivity increased from 0.1 mS/cm at 25°C to around 1 mS/cm with a 20 wt% loading when ZIF-8 (Zeolitic Imidazolate Framework-8) was added to a PVA matrix [70].

3.2.7. Graphene Oxide as a Filler

Graphene oxide (GO) has emerged as one of the most studied 2D nanomaterials for enhancing AEMs due to its large surface area, tunable functionalization, and outstanding mechanical and chemical properties [87]. In this section, GO will be explored as a material and its fit for AEM development.

Graphene Oxide Synthesis

Hummers' method, which involves oxidizing graphite using a mixture of powerful oxidizers, is the most typical approach to synthesizing graphene oxide [42]. Typically, graphite powder is treated with sulfuric acid (H_2SO_4), potassium permanganate ($KMnO_4$), and sodium nitrate ($NaNO_3$) to introduce oxygen-containing functional groups like hydroxyl, epoxy, and carboxyl to the surface of graphite. Although the functional groups can be found all over the surface of GO sheets, they tend to be more concentrated around the edges. As a result of the disruption of the conjugated carbon structure caused by these functional groups, graphite oxide is formed, with some of the sp^3-hybridized carbon atoms becoming sp^3-hybridized. After oxidation, the exfoliation of graphite oxide into monolayer or few-layer GO sheets is usually achieved via ultrasonication or mechanical stirring. This process results in oxidized GO sheets, which are more hydrophilic and easier to disperse in solvents.

GO's thin structure consists of mono atomic layer or few-layer sheets, with lateral dimensions ranging from hundreds of nanometers to several micrometers, depending on the synthesis method [42]. This large surface area enables efficient interaction with the polymer matrix. If oxidation occurs in a harsher environment, for longer or at higher temperatures, and exfoliation is done at higher power sonication, the resulting GO will be smaller in size and more oxidized. Functional groups and interlayer spacing reach a thickness of about 0.8 nm, more than the thickness of a single layer of graphene (0.34 nm) [62]. Commercially available GO is generally around 2 µm in lateral size, but the sonication process can reduce its size. For example, it has been reported that after 120 minutes of ultrasonication, the size is reduced to 54.55% in an ultrasonic bath and to 86.36% in a probe sonicator [63].

Properties of Graphene Oxide

The powder form of GO does not have a net charge, but it possesses localized partial negative charges due to oxygen-containing groups and the negative π-cloud from its conjugated carbon structure. These regions facilitate electrostatic and hydrogen bonding interactions between GO and positively charged species in AEMs. When dispersed in solution, the deprotonation of these oxygen-containing functional groups confers a negative charge, enhancing GO's dispersibility in water and other polar solvents [81].

GO is electrically insulating (around 10^{-8} S/cm), in contrast to pristine graphene, a great electrical conductor (about 1000 S/cm) [58, 100]. The oxygen-containing groups break the conjugated carbon network, making the material more insulating. The insulating nature of GO prevents the unintended flow of electrons in AEMs, which could lead to short-circuiting or decreased performance [37, 41].

From a mechanical perspective, GO exhibits an intriguing combination of strength and flexibility [87]. Its Young's modulus, which measures the material's stiffness or resistance to elastic deformation, ranges from approximately 290 GPa to 430 GPa for amorphous GO in-plane, demonstrating its high rigidity compared to many polymers [73]. Because of its ability to withstand stress without deforming, GO is a great choice for use as a reinforcement in polymer matrices. However, despite its high stiffness,

GO also shows remarkable flexibility, meaning it can bend or be deformed without breaking [97]. This combination of high stiffness and flexibility is particularly advantageous for its addition to AEMs, as it can reinforce the membrane structure while allowing the material to accommodate mechanical stresses without compromising ion transport pathways, thus enhancing both mechanical strength, dimensional stability and durability.

Functionalization and Polymer Integration

GO tends to agglomerate due to strong van der Waals forces between its layers [100]. This aggregation significantly hinders the material's performance, especially at high concentrations, where the tightly packed layers reduce the effective surface area, block ion transport pathways, and cause defects within the membrane. These interactions are primarily driven by π-π stacking between GO layers.

To overcome this issue, GO is frequently functionalized to prevent agglomeration and ensure a uniform dispersion in the polymer matrix, as well as to enhance its compatibility with the polymer chemistry [100]. Functionalization introduces chemical groups that modify the surface properties of GO, increasing the distance between sheets and weakening the van der Waals forces. Common functionalization strategies include covalent and non-covalent modifications [41]. Covalent methods involve chemically bonding functional groups such as amines, silanes, or polymers directly onto GO's surface. Non-covalent methods include adsorption of surfactants or polymers via π-π interactions, hydrogen bonding, or electrostatic forces.

Functionalization is critical to optimizing GO's interaction with polymer matrices. The typical interaction between GO and the polymer matrix is primarily through hydrogen bonding, as seen in early studies where GO was embedded in ether-containing polymers [100]. Additionally, interactions such as π-π stacking and π-cation interactions also play a significant role in binding GO to the polymer. However, when GO is functionalized, these interactions can be further enhanced. The oxygen-rich surface of GO can be easily chemically modified using covalent functionalization, where oxygen reactive groups are exploited to attach various functional groups or polymer chains. The functionalization of GO is tailored based on the polymer matrix being used, as it should enhance compatibility between the two. This can influence the final properties of the composite membrane and increase the acceptable concentration of GO before agglomeration occurs [87].

Several methods exist for the incorporation of GO into polymer matrices. The most typical process involves combining GO with a polymer solution and then evaporating the solvent to produce the membrane [41]. Some other approaches are in-situ polymerization, which involves combining GO with monomers while polymerization is taking place, and melt mixing, which involves blending GO with a molten polymer [87]. These techniques aim at evenly dispersing GO within the polymer. One reported method to reduce agglomeration is post-casting methylation to quaternize ammonium groups, ensuring that no cations interact with GO prior to casting [21]. It has been reported in literature that adding GO to polymer matrices with cationic sites enhances compatibility due to GO's hydrophilicity. Alternatively, quaternized functionalized GO has been incorporated into polymer backbones without cationic functionalization to reduce the risk of their alkaline degradation [75]. While GO incorporation can improve mechanical properties and ion conduction, it may sometimes lower the alkaline stability of the membrane due to nucleophilic attack [41].

AEM Improvement

When incorporated into AEMs, GO interacts with the polymer matrix in several beneficial ways. The presence of hydrophilic functional groups on GO improves the ion-conducting channels by enhancing hydrophilic domains in the polymer matrix, guiding the transport of hydroxide ions [87]. GO's 2D structure also helps to organize these hydrophilic domains into continuous ion-conducting channels. It has been reported that GO can be further aligned through the application of magnetic fields, further improving conductivity pathways [41]. Additionally, the formation of separate ionic and non-ionic domains can be facilitated by functionalized GO (for example, long alkyl chains), which can lead to microphase separation in block copolymers [87]. Furthermore, GO can improve the mechanical properties of AEMs, reinforcing the polymer matrix. GO can also reduce the formation of polymer defects and promote matrix crystallization, leading to enhanced composite reinforcement [41].

Why GO?

Graphene oxide (GO) was selected as a filler for this study due to several key properties that make it particularly advantageous for enhancing AEMs. As a 2D material, GO offers a large surface area, facilitating extensive interaction with the polymer matrix and enhancing the formation of continuous ion-conducting channels [87]. Its hydrophilic oxygen-containing groups further support ion transport by creating pathways that attract and guide hydroxide ions. Additionally, GO's unique mechanical properties, combining both stiffness and flexibility, make it an excellent choice for reinforcing the mechanical properties of AEMs [97].

Another significant factor in choosing GO is its availability and cost-effectiveness [42]. Unlike other nanofillers, such as LDHs or MOFs, which often require complex and time-consuming synthesis procedures, GO is easier to produce and commercially available. This makes it a practical choice for experimentation and more economically viable for large-scale AEM applications compared to more expensive fillers like CNTs or MOFs.

One of GO's most valuable properties is its functionalization potential [100]. The oxygen-containing groups on GO make it highly tunable, allowing functional modifications to optimize its compatibility with various polymer matrices and improve membrane performance. This flexibility in functionalization also creates opportunities for future research.

Additionally, GO's insulating properties are particularly beneficial in electrochemical systems, preventing short-circuiting and ensuring that ion-conducting pathways remain intact [37, 41]. Moreover, GO is compatible with advanced fabrication techniques such as electric field-assisted casting, for improved ion transport. This feature also presents opportunities for further studies.

3.3. Research Formulation

This research addresses the enhancement of AEMWE through the development of composite AEMs using GO as a filler. AEMWE has shown promise as a viable method for hydrogen production, particularly due to its potential for cost reduction in comparison to PEMWE [61]. However, the key to advancing AEMWE lies in improving the membrane's ion conductivity, mechanical stability, and chemical resilience under alkaline conditions [74]. These areas represent the current focus of AEM research, which seeks to refine materials and membrane structures to overcome limitations in durability and efficiency [117].

The polymer used for this study is a poly(co-aryl piperidinium) block copolymer, introduced in 2021 as a promising candidate for AEMWE applications [14]. The structure of this polymer is shown in figure 3.8; however, the exact copolymer segments are not disclosed due to confidentiality. This polymer features an aromatic backbone, with one segment contributing rigidity and another providing flexibility, allowing for effective ion transport while maintaining structural integrity. Additionally, its piperidinium cationic groups offer enhanced resistance to degradation in alkaline environments, making it a promising base polymer [74]. Studies on this class of polymers indicate its potential to balance conductivity, stability, and mechanical strength. Recent advancements have aimed to improve these properties through various approaches, including polymer cross-linking [16, 17], modifications to the arrangement and composition of block copolymer segments [18, 17], cross-linking with alternative polymer phases [15], and the introduction of hydrophobic side chains [51]. However, the use of fillers like GO to enhance the properties of this polymer remains unexplored.

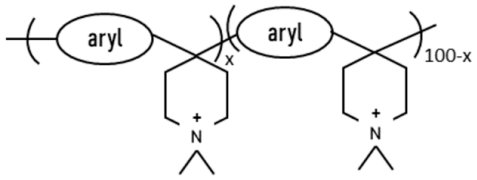

Figure 3.8: Poly(co-aryl piperidinium) AEP used in this thesis.

GO, a 2D nanomaterial, has gained interest as AEM filler due to its hydrophilic nature, large surface area, stiffness and flexibility, and compatibility with various matrices. Together, these properties give GO the potential to improve ion-conducting channel formation, enhance alkaline stability, increase mechanical integrity, and actively support the conduction mechanism, as demonstrated in studies conducted on other polymer matrices [87].

In this thesis, GO is investigated as a filler for poly(co-aryl piperidinium) to assess its impact on electrochemical performance, focusing on conductivity and mechanical stability, two critical properties for effective AEM function. The study seeks to determine an optimal GO loading that enhances both properties, overcoming the typical trade-off between ion conductivity and structural stability. In pursuit of this goal, the central research question guiding this work is:

What is the optimal loading of graphene oxide filler for improving ion conductivity and mechanical stability in poly(co-aryl piperidinium) anion exchange membranes?

The research framework consists of two main stages: first, developing a reliable and reproducible membrane-casting procedure to create composite membranes with the selected polymer matrix at various GO concentrations; and second, a comprehensive testing phase, where these membranes are evaluated across multiple sets to ensure statistical validity, focusing on key AEM properties.

Through this framework, this research aims to provide valuable insights into the potential of GO as an effective filler material for advanced AEMs, contributing to the broader goal of improving AEMWE technology for efficient hydrogen production.

4

Experimental Methodology

4.1. Membrane Preparation

The fabrication of AEMs involved four key steps: polymer solution preparation, membrane casting, membrane drying, and activation for use in a water electrolysis cell.

4.1.1. Polymer Solution

The polymer, initially in its iodide form from the synthesis process, was dissolved in DMSO and stirred on a magnetic stirrer at 50°C until a homogeneous solution was formed, typically after about 3 hours. The polymer concentration was adjusted to 22 wt%, with approximately 0.7 g of polymer used per membrane. For membranes incorporating GO as a filler, the polymer was first dissolved in a reduced volume of DMSO, allowing for the subsequent addition of the GO dispersion to achieve the final desired concentration. Due to the initially lower volume of DMSO, the stirring process was more challenging and resulted in a highly viscous polymer solution. In contrast, for pristine membranes without any filler, the full volume of DMSO was added to the polymer solution at the outset.

4.1.2. Graphene Oxide Solution

Separately, the GO dispersion was prepared by dispersing GO flakes (15-20 layers, Sigma-Aldrich) in 1 mL of a DMSO solution containing 5% water as a co-solvent. The specific concentration of water in the solution was determined through an analysis aimed at optimizing the GO dispersion. This balance took into account the high polarity and strong hydrogen-bonding affinity of water with GO, against the polymer's insolubility in water. The solution was sonicated for 2 hours, with the water bath being replaced every 30 minutes to prevent the temperature from exceeding 40°C. A detailed rationale behind these choices is provided in appendix B. The concentrations of GO incorporated into the membranes were 0.0625%, 0.125%, 0.25%, 0.5%, and 1%, corresponding to GO masses of 0.4375 mg, 0.875 mg, 1.75 mg, 3.5 mg, and 7 mg, respectively, in 0.7 g of polymer.

4.1.3. Solution Mixing

Once the GO dispersion and polymer solution were prepared, the GO dispersion was gradually added to the polymer solution, which had been allowed to cool to room temperature. The dispersion was added drop by drop, while the mixture was continuously stirred to ensure homogeneous mixing and avoid phase separation. The final solution was then stirred at room temperature for about 3 hours to ensure uniformity.

The temperature was maintained at a lower level to prevent water evaporation and increase the solution's viscosity, ensuring the optimal consistency for membrane casting [14]. To prevent air bubbles formed during stirring from affecting the homogeneity of the cast membrane, the solution was allowed to rest, enabling the bubbles to dissipate naturally. Alternatively, a desiccator and vacuum pump were used to expedite the degassing process.

4.2. Membrane Casting

Membranes were cast using an automatic TQC Sheen Dr Blade, calibrated to a height of 400 µm. Smooth-surfaced stainless steel plates were used as the casting surface, as rough surfaces would impede membrane peeling. Before each casting, the plates were cleaned using a few drops of DMSO followed by several acetone washes to ensure they were free of contaminants and dust particles.

Dr Blade was programmed to cast membranes at a length of 170 mm with a casting speed of 0.1 mm/s. Approximately 3 mL of the polymer solution was deposited as a 3 cm x 2 cm rectangular-shaped droplet near the blade, with the shorter side aligned in the direction of casting, after which the casting process began. The casting plate was securely clamped, and the Dr Blade moved steadily at the preset rate. The temperature, pressure, and relative humidity in the casting chamber were kept at ambient conditions. The produced membrane sheet was sufficient to yield one 4 cm square membrane with remaining material for additional testing.

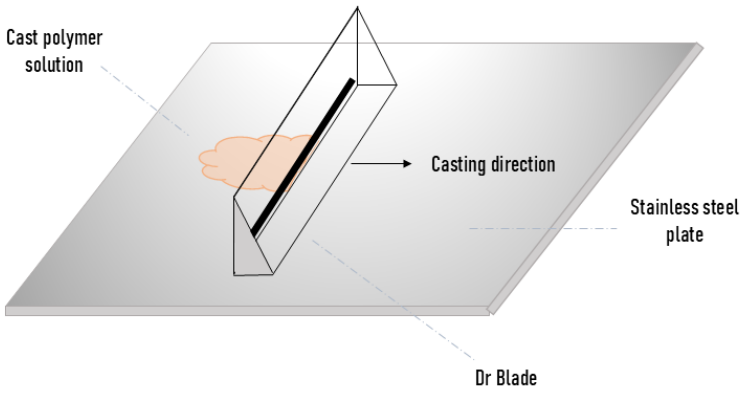

Figure 4.1: Membrane casting setup using a Dr Blade [29].

After casting was completed, the plate with the membrane on top was placed in an oven at 50°C and left to dry overnight. Given that the boiling point of DMSO is relatively high at 189°C, it was likely that some DMSO remained in the membrane. However, increasing the drying temperature could lead to instability during the drying process and cause ruptures in the membrane. This issue is further discussed in the appendix B.

To detach the membrane from the plate, water was poured onto the membrane and left for approximately 30 minutes. After this period, the membranes could be easily peeled off the casting plate. The peeled membrane was then placed between polymethyl methacrylate (PMMA) plates and dried overnight in a vacuum oven at 40°C.

Finally, the membranes were prepared for further use and testing. For conductivity and electrochemical testing, the membranes, still in the iodide form, needed to be soaked for 48 hours in KOH, during which hydroxide ions replaced the iodide ions. This activation time was selected during previous phases of the project, which indicated that while anion exchange occurred within the first 12 hours, as evidenced by a constant IEC, the thickness of the wet membranes continued to increase up to 48 hours, after which it stabilized [5].

4.3. Polymer Characterization

4.3.1. Chemical Characterization

Proton Nuclear Magnetic Resonance (H NMR)

H NMR spectroscopy was used to confirm the chemical structure of the polymer batches [20]. A sample of 5–10 mg of polymer was dissolved in 0.75 mL deuterated d6-DMSO (Sigma Aldrich, chemical shift at 2.50 ppm [14]) and 20 µL of trifluoroacetic acid (TFA, Sigma Aldrich) was added to eliminate the water peak at 3.34 ppm [14]. The solution was stirred for thirty minutes before being transferred into clean NMR tubes. Spectra were collected using an Agilent NMR spectrometer operating at 400 MHz.

Fourier-Transform Infrared Spectroscopy (FT-IR)

FT-IR spectroscopy was carried out to confirm the polymer structure of the polymer batches [44]. Dry membrane samples were positioned between the infrared source and detector, and measurements were performed in transmission mode using a ThermoScientific Nicolet iS50 instrument. The spectral range covered was from 500 to 4000 cm^{-1}. Background measurements were taken using a blank sample, and these were subtracted from the final data to ensure accurate results.

4.3.2. Thermal Properties

Thermogravimetric Analysis (TGA)

TGA was conducted to evaluate the thermal stability of the two different polymer batches and to relatively assess the graphene oxide (GO) content in membranes with varying GO loadings. Small fragments of membrane or polymer powder were dehydrated in a vacuum oven before measurement [89]. The analysis was carried out using a PerkinElmer Thermogravimetric Analyzer 8000, with a temperature range of 30°C to 800°C and a heating rate of 10°C/min [14].

Differential Scanning Calorimetry (DSC)

DSC was used to measure the glass transition temperature (Tg) of the two polymer powder batches to assess potential differences in polymer structure [31]. Samples (2-3 mg) were heated from -40°C to 440°C at a rate of 5°C/min using a PerkinElmer Diamond DSC with liquid nitrogen cooling.

4.3.3. Rheological Properties

Viscosity Measurements

Viscosity measurements were performed to determine the intrinsic viscosity of the polymer [122, 90]. A 1 wt% stock solution was prepared by dissolving 0.25 g of polymer in 25 mL of DMSO, and additional samples were prepared by serially diluting the stock solution. Measurements were conducted using a TA Instruments HR10 Hybrid Rheometer equipped with a concentric cylinder geometry, which required a sample volume of approximately 23 mL. The resulting viscosity ratios were plotted against polymer concentration to calculate the intrinsic viscosity. A detailed procedure is provided in the appendix C.

4.4. Membrane Characterization

4.4.1. Scanning Electron Microscopy (SEM)

Scanning Electron Microscopy (SEM) was employed to investigate the surface morphology and distribution of GO in the membranes [47]. Samples were analyzed using a JMS-IT700 series SEM from JOEL. Cross-sectional analysis was conducted to evaluate the dispersion of GO within the polymer matrix following sample fracture in liquid nitrogen (N_2).

4.4.2. Atomic Force Microscopy (AFM)

Atomic Force Microscopy (AFM) was utilized to assess the effect of GO on membranes' surface topography [49]. Samples were examined using a Bruker AFM. The imaging was conducted in tapping mode to minimize sample damage while acquiring detailed topographical information.

4.4.3. Nano-indentation

Nanoindentation testing was conducted to evaluate the mechanical properties of the membranes, specifically hardness and Young's modulus, in relation to varying GO content [69]. The measurements were performed using an MTS Nanoindenter XP equipped with a Berkovich tip. Each membrane was securely glued to an aluminum substrate, and a drift limit of 0.15 nm/s and an indent depth limit of 1 µm were set. Before testing the membrane samples, a control piece of quartz was indented five times to calibrate the setup. A total of 25 indentations were made using continuous stiffness mode in a clear square area at the center of each membrane, with each indent spaced 25 mm apart [21].

4.4.4. Water Uptake (WU)

Water uptake (WU) is a key parameter for understanding how the membrane structure responds to a water environment, by assessing the changes in mass. To measure WU, 4x4 cm squares of the membranes were soaked in 1M KOH for 48 hours, during which ion exchange with hydroxide ions also

occurred. After soaking, the membranes were quickly wiped with lint-free lab tissues to remove any surface liquid. The weight of the membranes was recorded both before (M_{dry}) and after soaking (M_{wet}). WU was then calculated using the following equation [66]:

$$\mathrm{WU}(\%) = \frac{M_{\mathrm{wet}} - M_{\mathrm{dry}}}{M_{\mathrm{dry}}} \times 100\% \tag{4.1}$$

4.4.5. Swelling Ratio (SR)

Similarly to WU, the swelling ratio (SR) is an important parameter for evaluating how the membrane structure reacts to a water environment, specifically by analyzing the change in thickness. To measure SR, the same membrane samples used for WU were also measured for thickness using a digital micrometer before (T_{dry}) and after (T_{wet}) soaking in 1M KOH for 48 hours and wiping off any excess surface liquid. SR was then calculated using the following equation [66]:

$$\mathrm{SR}(\%) = \frac{T_{\mathrm{wet}} - T_{\mathrm{dry}}}{T_{\mathrm{dry}}} \times 100\% \tag{4.2}$$

4.4.6. Ion Exchange Capacity (IEC)

Ion exchange capacity (IEC) is a crucial parameter that indicates the number of available cationic sites in an AEM, which are responsible for transporting anions such as hydroxide ions (OH^-). In this study, the IEC was determined by titration using a digital titrator. Membrane samples were first soaked in 40 mL of 1M NaCl solution for 48 hours to exchange the I^- ions present in the piperidinium functional groups of the membrane with the Cl^- ions from the solution. After the ion exchange, the membranes were thoroughly rinsed with water to remove any residual NaCl solution. The membranes were then soaked for 48 hours in 40 mL of 1M $NaNO_3$ solution, allowing the Cl^- ions to be released back into the $NaNO_3$ solution. This solution was subsequently titrated with $AgNO_3$ using K_2CrO_4 as a chloride indicator, with the endpoint indicated by a color change from yellow to brown/red with the formation of $Ag_2Cr_2O_4$, as shown in figure 4.2.

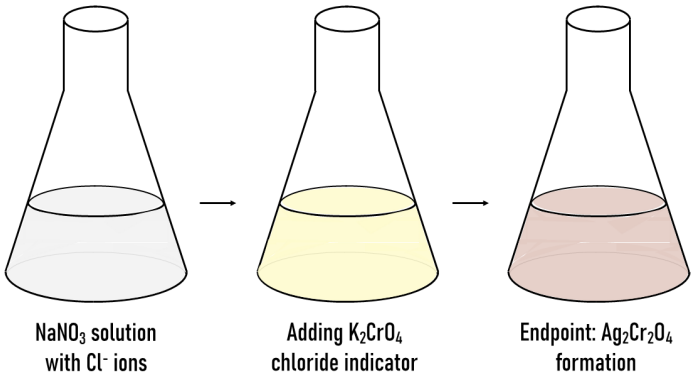

Figure 4.2: Schematic diagram of the IEC measurement.

The IEC was then calculated using the following equation [66]:

$$\mathrm{IEC\,(meq/g)} = \frac{V_{\mathrm{AgNO_3}} \cdot C_{\mathrm{AgNO_3}}}{M_{\mathrm{dry}}} \tag{4.3}$$

where $V_{\mathrm{AgNO_3}}$ is the volume of $AgNO_3$ used, $C_{\mathrm{AgNO_3}}$ is the concentration of $AgNO_3$, and M_{dry} is the mass of the dry membrane used for the experiment in grams. Since hydroxide ions (OH^-) are monovalent, the values of IEC in meq/g are numerically equivalent to mmol/g.

4.4.7. Conductivity

The ion conductivity of AEMs was measured using a four-probe setup, as illustrated in figure 4.3 [66]. The experiments were conducted using an AUTOLAB Potentiostat coupled with a 10-A booster from Metrohm. To prepare the 4x4 cm membrane squares for measurement, they were soaked in 1M KOH for 48 hours to allow for full ion exchange, as previously mentioned. During the tests, 1M KOH was recirculated through the system at a high flow rate of 100 rpm to ensure rapid bubble removal.

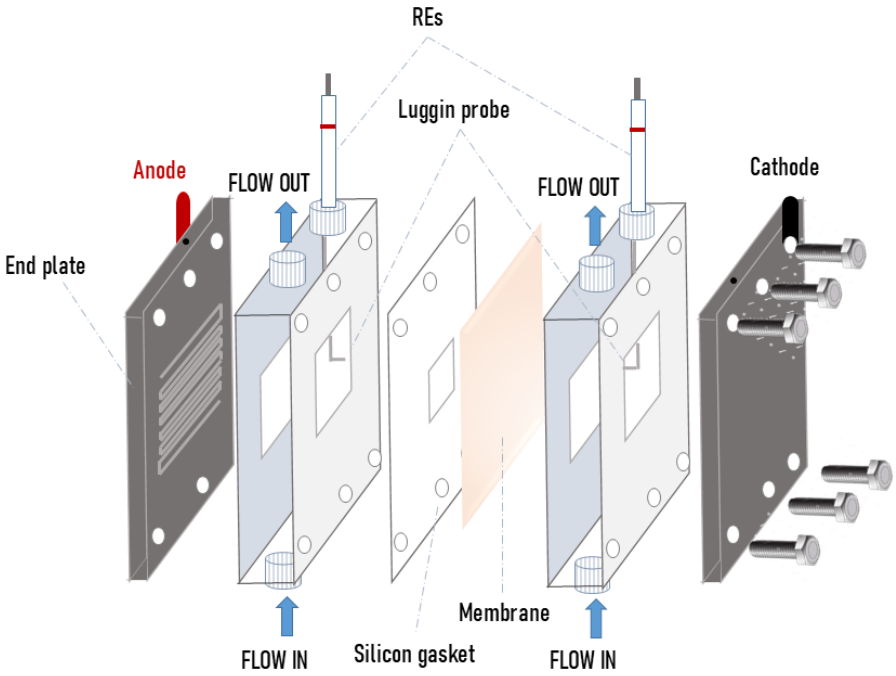

Figure 4.3: Schematic diagram of the four-probe setup used for measuring the ion conductivity [29].

The four-probe setup involved two outer electrodes (working and counter electrodes) responsible for applying the current, and two inner reference electrodes connected to Luggin probes to measure the voltage drop across the membrane. The reference electrodes used were Hg/HgO (1M KOH) (BASI Research Products). The capillaries were carefully positioned perpendicular and as close as possible to the membrane surface to ensure accurate voltage measurements.

Ion conductivity (σ) was assessed using the Linear Sweep Voltammetry Galvanostatic procedure on Nova software, with the current linearly swept from 0 to 0.3 A at a rate of 20 mA/s. Operating in the low current regime helped to avoid bubble formation, which could otherwise compromise the accuracy of the measurements. Initial potential vs. current curves were recorded without any membrane (blank) to determine the Ohmic resistance of the system. The resistance of the system (R_{blank}) was calculated from the slope of the linear voltage vs. current curve using regression analysis. Following this, the membrane was introduced, and another curve was plotted and analyzed to obtain the total resistance (R_{total}) of the membrane and the system.

The membrane resistance (R_{membrane}) was derived by subtracting the blank resistance (R_{blank}) from the total resistance (R_{total}) using the following equation:

$$R_{\text{membrane}} = R_{\text{total}} - R_{\text{blank}} \tag{4.4}$$

Finally, the ion conductivity (σ) of the membrane was calculated using the following formula [66]:

$$\sigma(\text{mS/cm}) = \frac{d}{R_{\text{membrane}} \cdot A_{\text{membrane}}} \tag{4.5}$$

where d is the thickness of the wet membrane, R_{membrane} is the resistance of the membrane, and A_{membrane} is the surface area of the membrane exposed to hydroxide ion conduction (7.62 cm^2), corresponding to the area of the silicon gasket used to couple the membrane.

4.4.8. Electrochemical Performance

The electrochemical experiments were performed in a zero-gap alkaline electrolytic cell filled with 1M KOH as the electrolyte [95]. Figure 4.4 provides a schematic representation of the cell setup. The AEMWE cell is composed of two corrosion-resistant end plates with serpentine flow channels (Dioxide Materials, USA), along with silicon gaskets and a membrane electrode assembly (MEA). The end plates facilitate the recirculation of the electrolyte through connected inlet and outlet channels. The MEA typically comprises a cathode, an anode, and the anion exchange membrane (AEM), where the electrodes usually include a gas diffusion layer (GDL) and a catalyst layer. In this study, however, pure Ni felt GDLs were used for both the cathode and anode to streamline the process and ensure that any differences in electrochemical performance arise solely from the membrane itself.

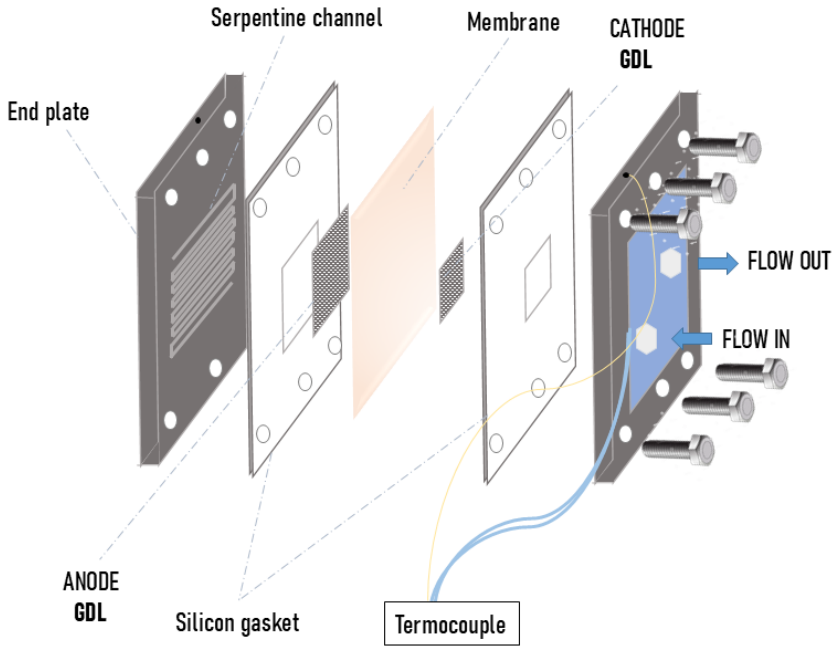

Figure 4.4: Schematic diagram of the zero-gap electrolytic cell [29].

After a 48-hour activation in 1M KOH, the 4x4 cm membrane squares were subjected to testing within the electrochemical cell, as illustrated in Figure 4.5. The electrolyte was circulated through both compartments at a rate of approximately 5 mL/min per compartment (60 rpm). The tests were powered by an AUTOLAB potentiostat coupled with a booster and conducted at room temperature.

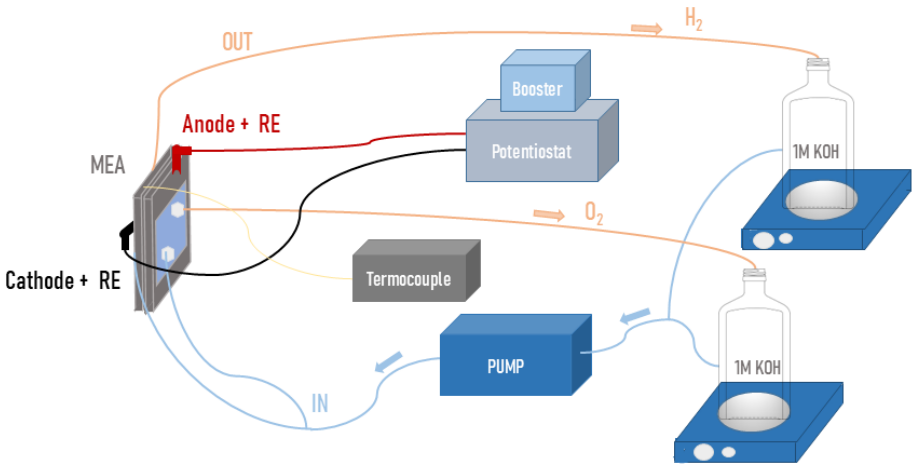

Figure 4.5: Schematic of the experimental setup used for electrochemical performance testing [29].

The testing protocol, executed using Nova software, comprised three sequential phases. The first phase involved stabilizing the system through chronopotentiometry (CP), applying a current of 1.5 A for 1500 seconds. CP is particularly useful for monitoring the stability of the electrochemical system over time. By observing the potential response under a constant current, it provided insight into the system's equilibrium before the next phase [86]. Following CP, five cycles of cyclic voltammetry (CV) were performed, sweeping the potential between 1.3 V and 2.3 V at a scan rate of 20 mV/s and a step size of 2.44 mV. CV is a key technique for assessing the electrochemical properties of membranes. The resulting cyclic voltammograms provided an analysis of current density, calculated by dividing the current by the membrane area of 5.76 cm^2, as a function of applied voltage. This analysis was critical for evaluating the performance and efficiency of the AEMs under operational conditions, although these measurements were conducted at room temperature. The data collected during CV was used to plot the polarization curve, primarily to determine the maximum current density at a given voltage. Finally, the experiment concluded with a second CP measurement under the same conditions as the initial phase, applying 1.5 A for another 1500 seconds. This final CP step verified the stability of the membrane and the overall system after the CV scans, ensuring that performance remained consistent.

5

Results and Discussion

5.1. Membranes

To begin the discussion of the results, figure 5.1 presents a set of six membranes: one pristine and five with varying GO loadings, 0.0625%, 0.125%, 0.25%, 0.5%, and 1%, that were subjected to testing. These concentrations were selected based on common filler percentages for AEMs found in literature and considering the weaker interaction between the polymer used and GO. A more detailed rationale behind these concentrations is provided in appendix B.1.2 and B.2.4. In total, three sets were cast and tested: one set from Batch 1 and two sets (2-a and 2-b) from Batch 2. The process of assessing the differences between the two polymer batches is detailed in appendix C.

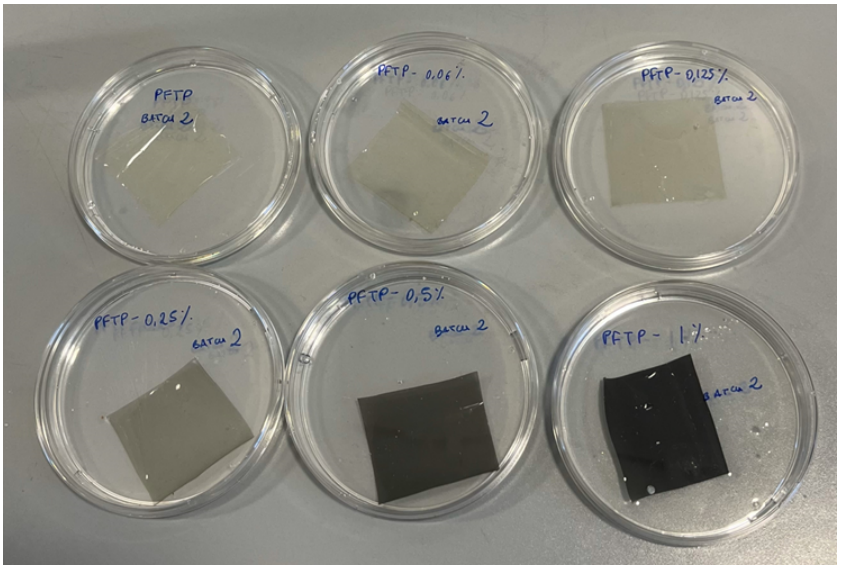

Figure 5.1: Membrane samples at increasing GO concentrations.

5.2. Conductivity

Conductivity is the crucial parameter for rating AEMs because it directly influences the current density, which is proportional to the rate of hydrogen production [94]. Figure 5.2 shows the OH^- conductivity for different membranes from Batch 2. The conductivity graph for Batch 1 is reported in appendix D.1.

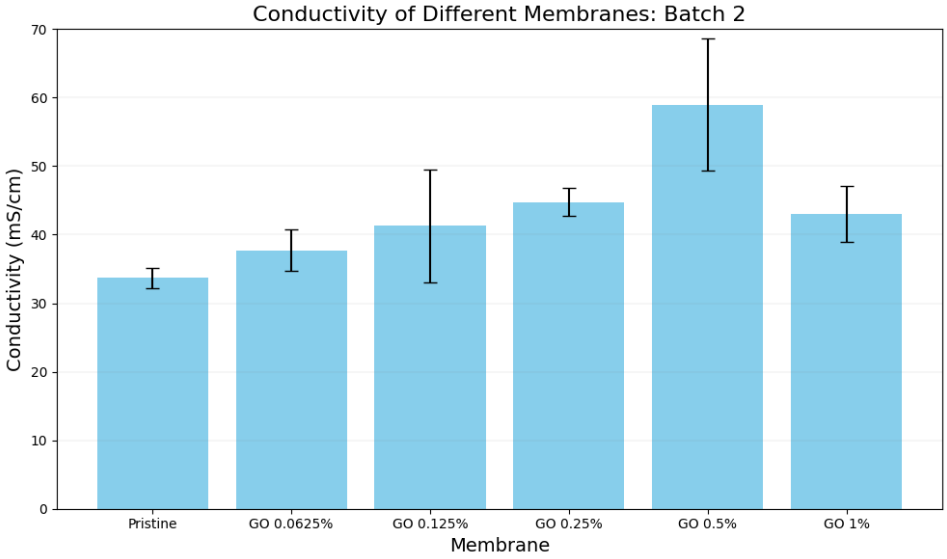

Figure 5.2: Conductivity of membranes.

The conductivity increases with GO concentration, starting from 33 mS/cm for the pristine membrane and reaching an average of 59 mS/cm at a loading of 0.5%, followed by a decrease at 1%.

This trend aligns with the anticipated outcome and is consistent with findings in literature for GO-filled AEMs. Multiple papers on the topic, in fact, report the same trend. A study conducted on Im-GO embedded in Im-PSF shows increased conductivity up to a 0.2% loading, rising from 10 mS/cm to 23 mS/cm, followed by a decrease attributed to agglomeration [77]. Similarly, research on IL-GO dispersed in Im-PPO reports an increase in conductivity from 20 mS/cm to 40 mS/cm with increasing GO concentration up to 0.5%, followed by a decrease at higher concentrations [126].

5.2.1. IEC

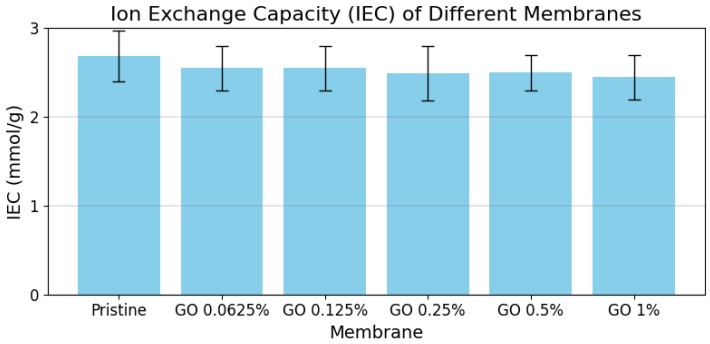

Figure 5.3: IEC of different membranes.

As shown in 5.3, the IEC values of the membranes show no significant differences when considering the error margins, though a slight decreasing trend is observed with increasing GO content. Specifically, IEC decreases from a pristine value of 2.7 mmol/g to 2.45 mmol/g at 1% GO content. The trend suggests a possible effect, though firm conclusions are difficult to establish within the error range. If

the trend holds, it may be attributed to the higher GO content lowering the relative polymer fraction, which carries the cation exchange sites being measured [21]. Additionally, as GO content increases, the partially negatively charged oxygenated groups of GO could potentially neutralize some cation exchange sites, leading to a reduction in effective IEC [100].

Literature on this topic presents widely varying trends in IEC with respect to GO filler concentration. Some studies functionalize both the polymer matrix and graphene oxide with cationic groups, others functionalize only the graphene oxide, and some only the matrix. These variations significantly impact the IEC trend. Even within these more specific groups, differences exist, highlighting the specificity of GO-polymer matrix interactions in each study. For example, a study on GO in quaternized polybenzimidazolium reported a decrease in IEC with increasing GO content [21], whereas studies that involve quaternized functionalization of GO generally show an increase in IEC, as seen in the addition of GGO to HPsf [75] or constant IEC with IL-GO in ImPPO [77].

Since the IEC does not increase with GO concentration, it cannot account for the observed conductivity trend. Typically, higher IEC values can cause dimensional instability due to the conductivity-stability trade-off in AEMs; however, here, conductivity is rising without any IEC increase [26].

Before exploring additional AEM parameters and hypothesizing about the structural impact of GO on the membrane and the mechanisms underlying the conductivity trend, the following section evaluates the membrane's performance in an AEM electrolytic cell, emphasizing its practical application.

5.3. Electrochemical Performance

Figure 5.4 shows the Current Density-Potential curves for one set of membranes (a) from Batch 2. This division is necessary due to variations in membrane thickness, which prevent generalization of current densities by GO loading class. Unlike conductivity, current density is not normalized for thickness, and, naturally, thicker membranes exhibit higher resistance, resulting in lower current densities [103]. The Current Density-Potential curves for set 2-b, and for Batch 1 are provided in the appendix D.2.

At first glance, the current densities appear not to follow the trend exhibited by OH^- conductivities. However, these curves are not directly comparable, as the membranes have varying thicknesses, as previously noted. The GO 0.5% membrane, which demonstrated significantly higher conductivity, now shows similar peak current densities: 176 mA/cm^2 for both GO 0.125% and GO 0.25%, and 173 mA/cm^2 for GO 0.5%.

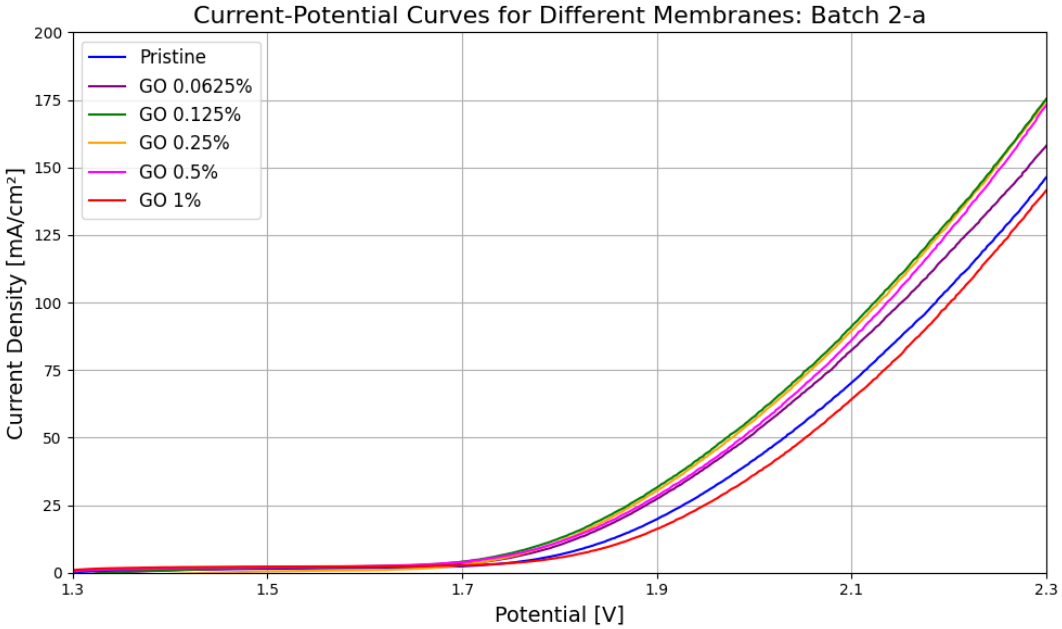

Figure 5.4: Current-Potential Curves of membranes: Batch 2-a.

The connection between conductivity and current-potential curves lies in the concept of conductance. In contrast to conductivity, conductance doesn't normalize for thickness. Therefore, to determine if, for example, the lower current density observed in the GO 0.5% membrane is attributable to its thickness or other factors, it is essential to verify whether conductance follows the same trend as the polarization curves.

Among the studies on GO as a filler for AEMs, only a few proceed to the final step of verifying membrane performance in practical applications, such as in electrolyzers or fuel cells. Most research instead focuses primarily on assessing material properties. However, this performance verification step is important to confirm that the improved conductivity, and thus reduced ohmic resistance, does not come with unintended consequences, such as an increase in other resistances [94]. Such increases could offset the benefits of improved conductivity, ultimately leading to reduced current densities and lower overall efficiency.

5.3.1. Conductance

The following equation calculates the conductance from the conductivity described in section 4.4.7:

$$G\,(\mathrm{mS/cm^2}) = \frac{\sigma}{d} = \frac{1}{R_{\text{membrane}} \cdot A_{\text{membrane}}} \tag{5.1}$$

Figure 5.5 presents the conductance of membranes in Batch 2-a, while the conductivity graph specific to set 2-a is available in the appendix D.2.1, along with the exact membrane thicknesses.

The trend shown in the conductance graph aligns with the current density curves: the GO 0.5%, GO 0.125%, and GO 0.25% membranes exhibit similar conductance levels, while GO 1% has the lowest conductance, but with relatively high standard deviations. Notably, the thicknesses vary, with 58 µm for GO 0.5%, 48 µm for GO 0.25%, and 40 µm for GO 0.125%. This indicates that the conductivity trend is indeed reflected in the current density trend, and the GO 0.5% membrane can achieves the highest conductivity and therefore optimal electrolyzer performance.

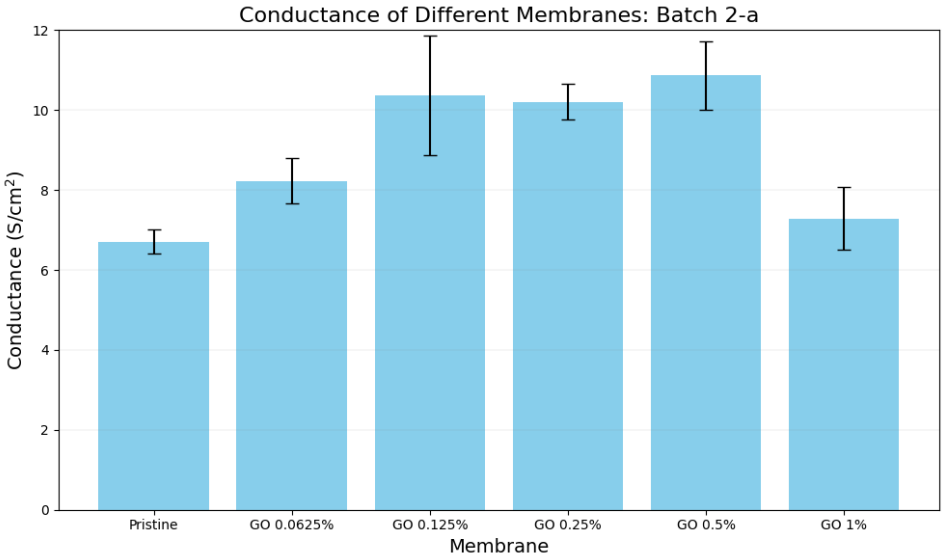

Figure 5.5: Conductance of membranes: Batch 2-a.

The error bars in figures 5.2 and 5.5, representing one standard deviation, are relatively large, particularly for certain membranes. Conductivity measurements were repeated multiple times on the same membrane, yet variability persisted across trials. This could be due to minor variations in the measurement setup, such as slight positional inconsistencies of the Luggin probes or differing levels of pressure applied when closing the cell. Additionally, combining data from the two sets within Batch 2 (2-a and 2-b) may have introduced further variability, possibly due to small differences in the actual GO loadings among membranes with the same nominal GO concentration.

The following sections will focus on analyzing additional AEM parameters to assess the integration of GO within the membrane, along with its effects on mechanical properties and dimensional stability, to determine if stability trade-offs are mitigated. This analysis will help establish a hypothesis regarding the structural impact of GO on the membrane and the mechanism underlying the conductivity trend.

5.4. Membrane Morphology

The membrane morphology was analyzed using SEM and AFM characterization techniques. The objective was to assess whether GO was homogeneously embedded in the membranes and to observe its overall effect on surface morphology.

5.4.1. SEM

Images (a) and (c) in figure 5.6 are taken in SED (Secondary Electron Detector) mode. This mode provides detailed topographical information, as it relies on secondary electrons from the outer shells of atoms, offering high-resolution surface details [47]. In SED mode, lighter areas may indicate regions of increased surface roughness, elevated features, or more conductive areas where secondary electron emission is enhanced. Comparing the images, no significant differences in morphology between the pristine and GO 0.5% membrane are detected, as both images exhibit lighter spots. Additionally, shadows seen in the images result from the low conductivity of the samples, which can affect SEM imaging quality [110].

BED (Backscatter Electron Detector) mode, used in images (d) and (d) in figure 5.6, uses higher-energy electrons deflected by the atomic nuclei, making it useful for identifying compositional variations based on atomic number and, sometimes, density [47]. However, identifying GO in these images is challenging due to the similarity in atomic number between GO's oxygen atoms and the nitrogen present in the pristine polymer, the heavier iodine atom residue from polymer synthesis and residual sulfur from incomplete DMSO evaporation, complicating identification.

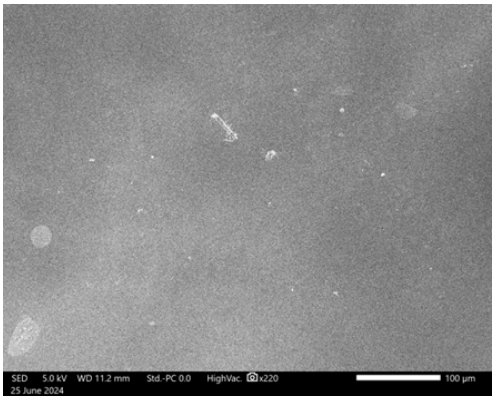

(a) Pristine membrane in SED mode

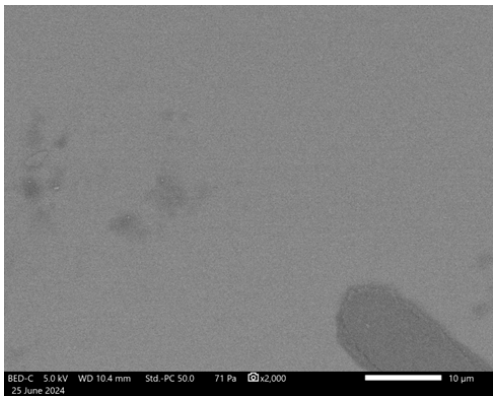

(b) Pristine membrane in BED mode

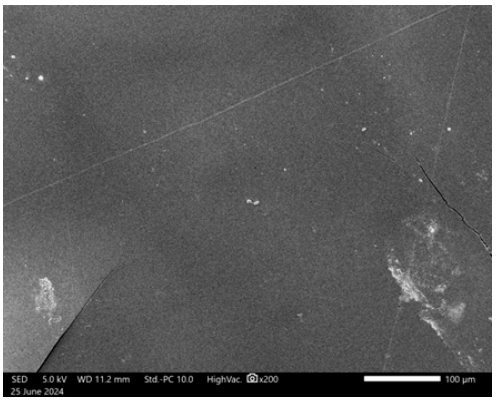

(c) GO 0.5% membrane in SED mode

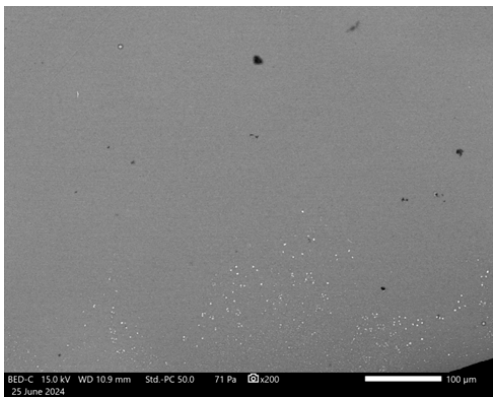

(d) GO 0.5% membrane in BED mode

Figure 5.6: SEM images of pristine and GO 0.5% membranes in SED and BED mode.

Both membranes exhibit occasional white spots, visible in both SED and BED modes, which are likely due to surface dust or other contaminants rather than intrinsic membrane features. Since no distinct surface differences between the pristine and GO 0.5% membranes were observed, it can be inferred that GO was embedded homogeneously, with no significant agglomeration or surface protrusions.
An attempt was made with EDS (Energy Dispersive Spectroscopy) to analyze compositional differences. However, this analysis, reported in appendix D.3, did not yield clear images for identifying variations in composition across the membrane surfaces.

Cross-sectional SEM analysis was performed on the membranes to visualize the internal structure where GO is embedded and to assess the distribution across different concentrations [19]. Figure 5.7 displays the cross-sectional images of the pristine, GO 0.125%, GO 0.5%, and GO 1% membranes. These images were obtained by fracturing the membrane samples in liquid nitrogen to create a brittle fracture. In each case, a textured area appears at the bottom, which is attributed to the fracturing process rather than a feature of the membrane. To confirm this, the membranes were fractured both from the side cast by the blade (e.g., in the GO 0.5% membrane image, where casting marks are visible on the top surface) and from the casting plate side (e.g., in the pristine membrane image).

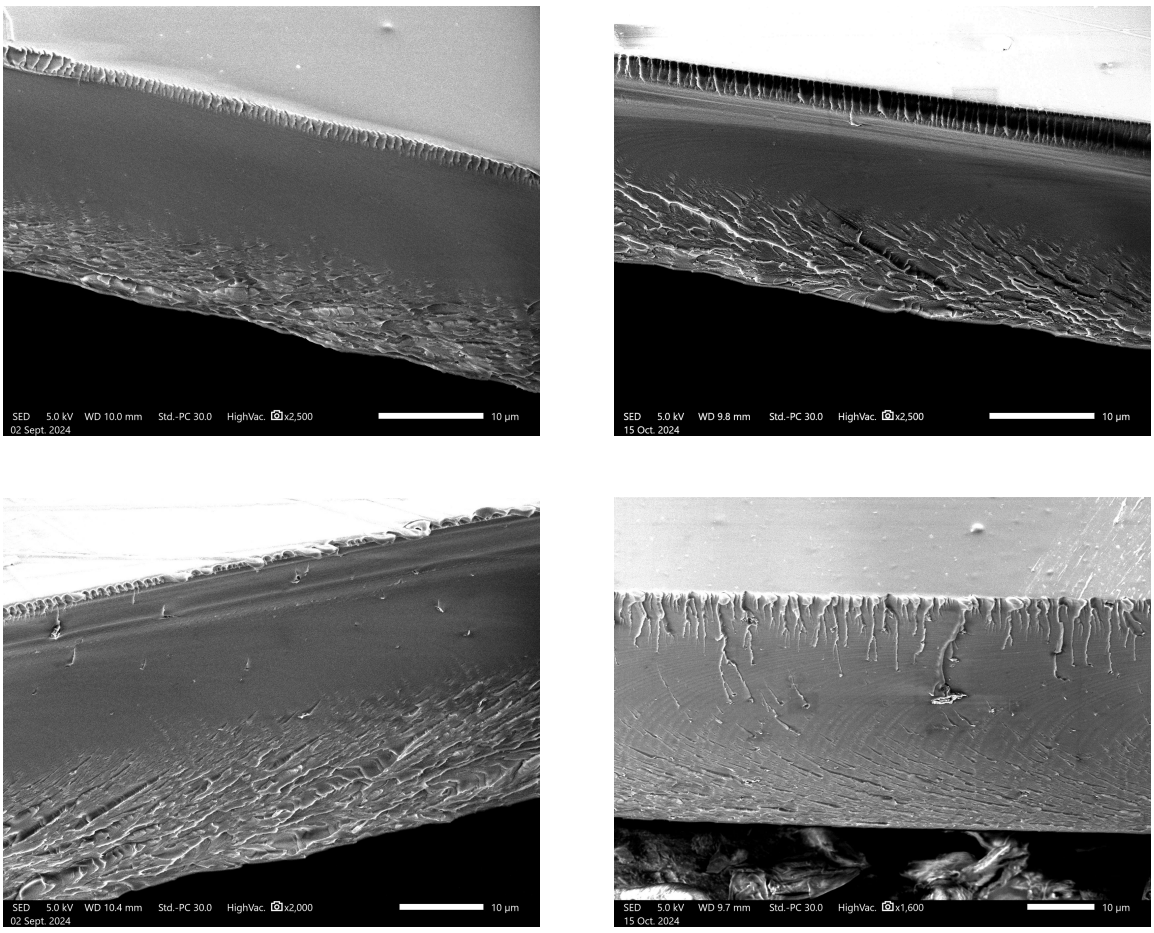

Figure 5.7: Cross-sectional SEM images of membranes: (Top left) Pristine, (Top right) GO 0.125%, (Bottom left) GO 0.5%, (Bottom right) GO 1%.

To compare the cross-sectional areas of the membranes, the smoother regions unaffected by the fracture were examined. The pristine membrane shows a smooth cross-section. The GO 0.125% membrane exhibits a few small, sporadic lighter spots, resembling minor defects. The GO 0.5% membrane shows more frequent small lighter spots. The GO 1% one exhibits larger chunk-like spots, probably some agglomeration. Given the increase in frequency and size of spots with rising GO concentration, they can likely be attributed to GO particles and the roughness they induced within the polymer matrix.

5.4.2. AFM

AFM analysis was conducted on the membranes to assess the effect of GO on surface topography [49]. Figure 5.8 shows the 3D and 2D AFM images of the pristine membrane and the GO 0.5% membrane. The pristine membrane has a relatively smooth surface, with general roughness noise reaching a maximum height of 12.4 nm. In contrast, the GO 0.5% membrane exhibits more pronounced surface bumps, with a maximum height of 42 nm. The marked difference in surface morphology suggests that these bumps in the GO 0.5% membrane can be attributed to the embedded GO particles, and not for example to surface dust. A similar variation in membrane topography observed in AFM images has been reported for an enhanced Fumion membrane with a 1% GO loading [6].

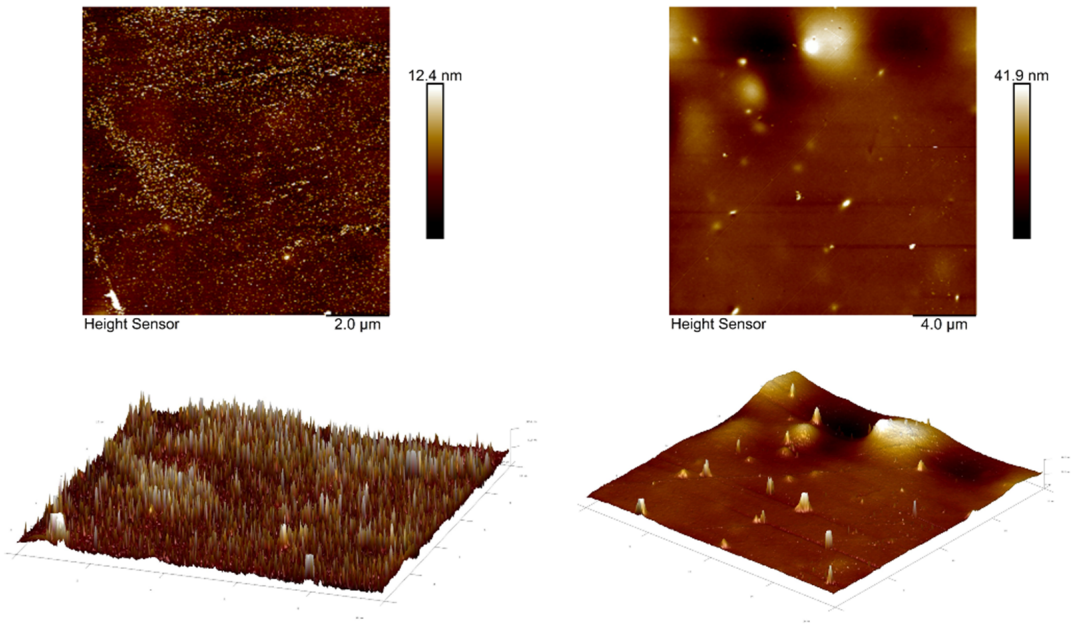

Figure 5.8: 2D and 3D AFM images of (Left) Pristine membrane (Right) GO 0.5% membrane.

5.5. Filler Concentration

TGA was conducted on membrane samples to assess GO's effect on thermal degradation and, most importantly, to verify whether the actual GO concentration in the membranes matched target values or at least followed the expected trend relative to each other [89, 84].

The polymer matrix, composing the pristine membrane, undergoes an initial mass loss due to moisture evaporation, followed by a significant weight loss stage between 250°C and 450°C, attributed to the decomposition of ammonium groups. A further final weight loss occurs above 500°C due to the degradation of the polymer backbone, as seen for the pristine membrane in 5.9 [14]. In contrast, graphene oxide exhibits two primary degradation stages: the first around 200°C and the second around 600°C, with slow continued degradation thereafter, depending on its level of oxygenation [85]. This makes GO less thermally stable than materials like graphite, making it less detectable in the polymer.

Figure 5.9 shows the thermal decomposition curves of the membranes. It is noticeable that the addition of graphene oxide does not significantly alter the degradation profile of the membrane, likely due to the low concentrations of GO used. However, by zooming in on the 500–600°C temperature range, where the polymer backbone decomposes, a clear trend corresponding to GO concentration can be observed, as seen in figure 5.10. As the GO content increases, the degradation step is delayed. For instance, at 560°C, the weight% residues for the membranes, from pristine to the highest 1% GO concentration, are as follows: 40.65%, 41.38%, 41.91%, 42.32%, 43.61%, and 44.32%. Similarly, the maximum peak temperatures of this degradation step, as observed in the derivative weight % curve (see appendix D.4), occur at 546.24°C, 547.40°C, 550.48°C, 554.81°C, and 559.81°C, respectively.
This trend of increasing GO loading and the small variations observed in the final polymer backbone decomposition step in the derivative weight % curve have also been highlighted in a study on QPPO/PSF

membranes embedded with GO, which reported similar findings across membranes with GO loadings of 0.5%, 1%, and 1.5% [83].

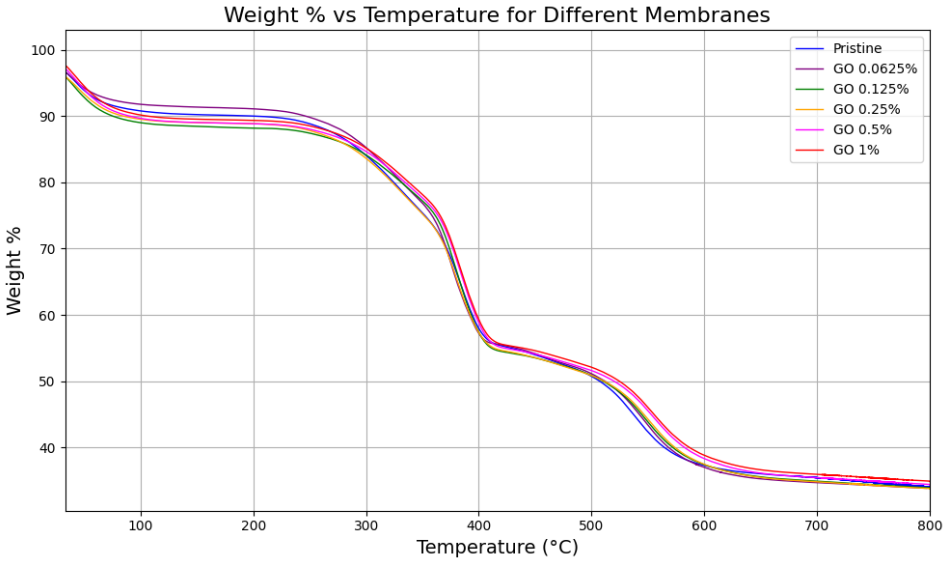

Figure 5.9: TGA weight% curves of membranes.

It must be noted that the samples tested for GO 1% did not consistently yield a curve following this trend. This inconsistency suggests that this concentration may exhibit agglomeration. When GO particles agglomerate, they no longer disperse uniformly throughout the polymer matrix, leading to localized regions with higher GO concentrations. This can disrupt the thermal behavior, resulting in irregular degradation profiles. A close-up figure with additional curves is presented in appendix D.4.

Although these variations are small, so are the concentrations of GO. This trend confirms that the procedure developed to produce the composite membranes was successful in creating homogeneous membranes with expected filler concentration, with uncertainty on the GO 1% one. Ensuring this correlation was crucial for validating that the trends observed at different GO contents are genuinely related to the filler concentration.

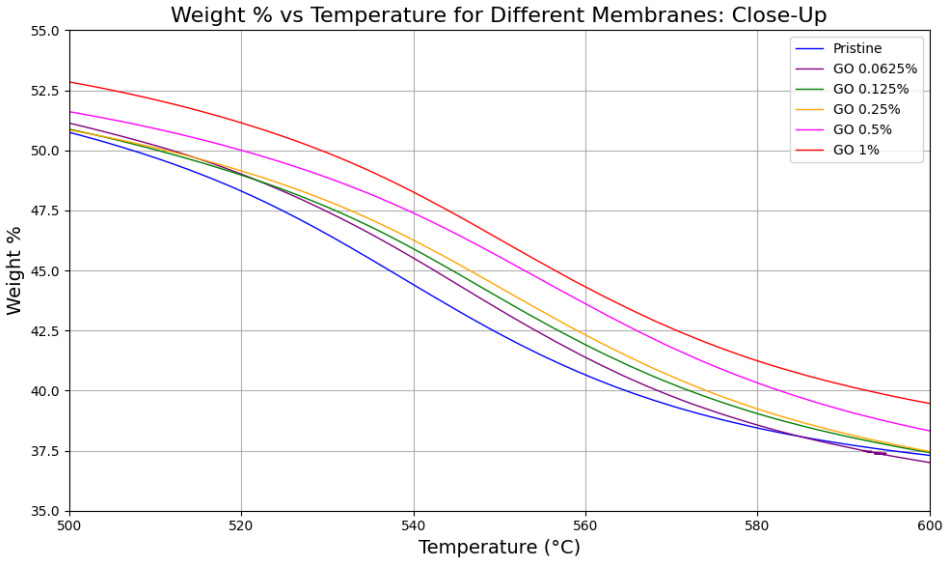

Figure 5.10: TGA weight% curves of membranes close up.

5.6. Nano-indentation

Nano-indentation was performed on the sample to assess the impact of adding different concentrations of graphene oxide on the membranes. The nano-indentation software calculates hardness and Young's modulus from the load-displacement data using the Oliver-Pharr method. More details on this can be found in appendix D.5.

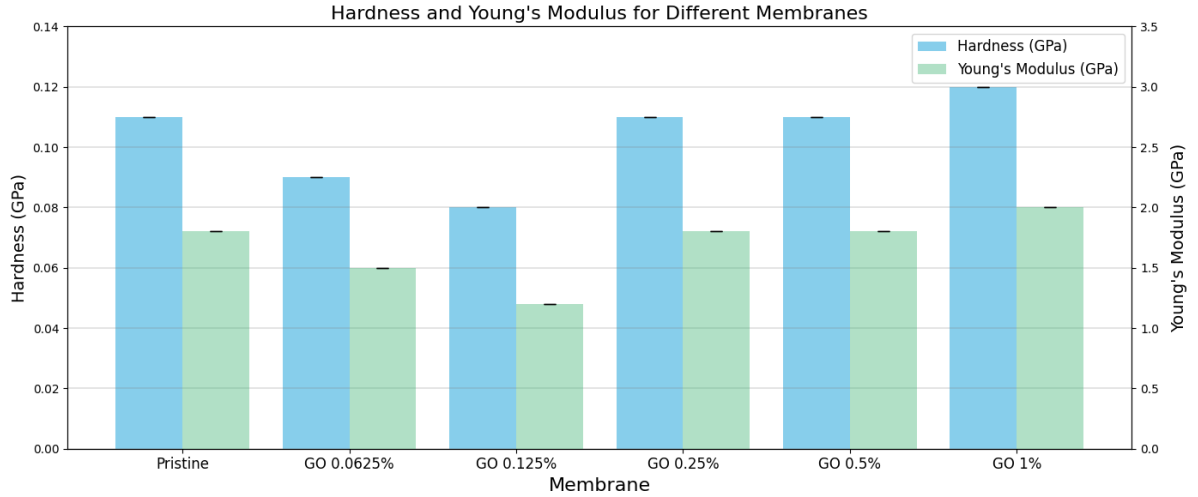

Figure 5.11: Hardness and Young's Modulus of membranes.

The main focus of this test was to verify the relative values of hardness and Young's modulus and observe trends depending on the GO concentration. Analyzing figure 5.11, a clear trend is evident: both hardness (H) and Young's modulus (E) follow a similar pattern and percentage of variation across the different GO membranes. A similar trend is reported in appendix D.5 for Batch 1. Starting from the values for the pristine membrane H=0.11 GPa and E=1.8 GPa, both H and E decrease up to GO 0.125%, reaching values of H=0.08 GPa and H=1.2 GPa. Then, with further increases in GO concentration, the values return to and then exceed the pristine values, reaching H=0.12 GPa and E=2 GPa at higher GO concentrations.

A hypothesis for the observed trend in mechanical properties at the structural level is as follows: at very low GO concentrations, the limited GO particles act as defects within the polymer structure, disrupting its crystallinity. These defects interfere with the natural packing of polymer chains without reinforcing the material's mechanical properties, due to the low concentration of GO. As a result, these particles behave more like structural defects, increasing free volume and allowing the polymer chains greater freedom of movement, thus reducing stiffness. A lower Young's modulus reflects reduced resistance to elastic deformation, meaning the material exhibits greater strain under the same stress. Essentially, the material becomes less stiff and more compliant, with polymer chains able to move more freely under stress. Hardness, in turn, is a surface property, indicating the material's resistance to permanent or plastic deformation from indentation, scratching, and other surface stresses. The lower hardness value suggests that the surface of the material has become less resistant to permanent deformation, potentially due to disrupted polymer matrix that lacks reinforcement.
As the GO concentration increases (0.25–1%), both Young's modulus and hardness rise again, suggesting a reversal of the initial structural disruption. The higher GO concentrations likely provide nucleation sites for crystallinity, a common effect with increased filler content, facilitating more organized regions within the polymer [87], [41]. This structural organization leads to greater stiffness and hardness, as the material becomes more orderly and GO forms continuous networks within the matrix. At these higher concentrations, GO may promote stronger interactions between polymer chains, enhancing mechanical properties. In this range, GO acts as a true reinforcement, increasing resistance to indentation and elastic deformation, thereby improving the material's mechanical performance, making it less elastic but with higher dimensional stability.

Other studies have investigated the effect of GO filler on the mechanical properties of membranes. In general, research on filling anion exchange membranes with GO does not necessarily focus on mechanical properties, as examined in this paragraph (E, H), but rather on those directly related to final application (WU, SR). Moreover, the minimum filler loading used in many studies is often higher than that used here, which is characteristic of lower mechanical property improvements. A study conducted on Nafion with sulfonated GO showed that at 0.1% GO, the hardness of the membrane decreased compared to the pristine one, then increased beyond this concentration, though no specific explanation was provided [65]. Another study on GO in polybenzimidazolium reported minimal variation in hardness, with Young's modulus showing an initial increase at 0.25% GO, followed by a decrease [21]. Additionally, a separate study showed a steady increase in E with increasing GO content from 0.25% to 1% of IL-GO in Im-PPO [126].

It is widely reported in the literature that fillers can enhance mechanical properties [87]. Fillers can reinforce the polymer matrix directly by providing a rigid framework that resists deformation, or through strong interfacial bonding between the polymer and filler, which helps transfer stress more efficiently across the matrix. Additionally, fillers can improve crystallinity [41], a property that generally increases values of Young's modulus and hardness.
On the other hand, fillers can also decrease crystallinity, particularly when they agglomerate and do not disperse uniformly within the polymer matrix, which can inhibit crystalline packing [80]. This disruptive effect has been observed even at very low filler concentrations. For example, in a study of GO in PVA, crystallinity decreased between 0.1% and 0.3% GO, after which it began to increase [128]. Naturally, these specific concentration values are unique to the GO and polymer matrix used and cannot be generalized, as they depend on the filler-polymer affinity and interaction.
The hypothesis that very low concentrations of GO act as defects, disrupting the crystalline structure and creating additional free volume without providing mechanical reinforcement, could aligns with these observations. This disruption results in a more compliant polymer chain, making the membrane less stiff and hard. At a threshold concentration, the filler begins to form a more interconnected network, enhancing crystallinity in the polymer structure and making the membrane stiffer and harder, as observed in the tested membrane samples.

5.7. Water Uptake and Swelling Ratio

Figures 5.12 and 5.13 show the WU and SR of the membranes, measured by weighing the mass (WU) and the thickness (SR) of the membranes before and after soaking for 48 hours in 1M KOH. Batch 1 graphs are reported in appendix D.6. The explanation and hypothesis for the observed trends are discussed below. The GO 0.125% concentration once again demonstrates threshold behavior.

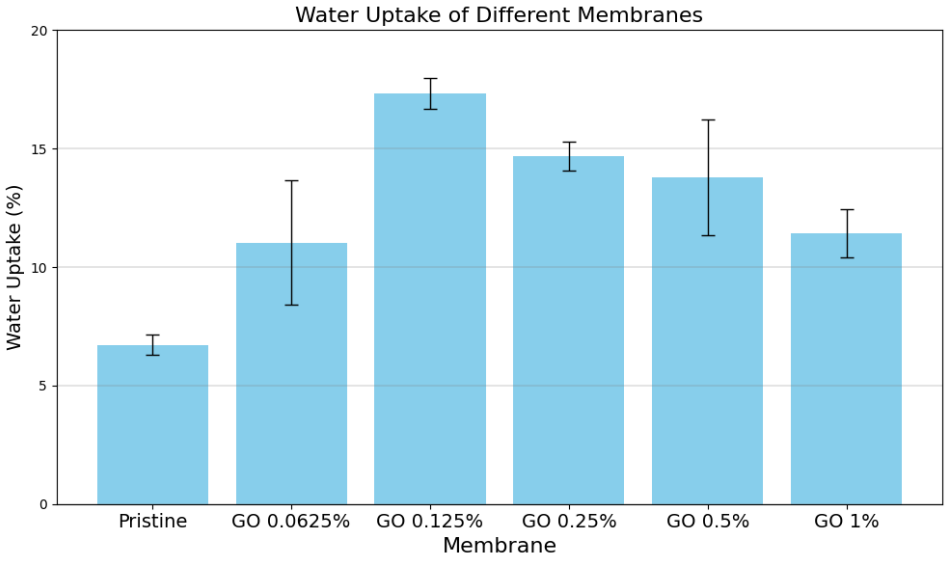

Figure 5.12: Water Uptake of membranes.

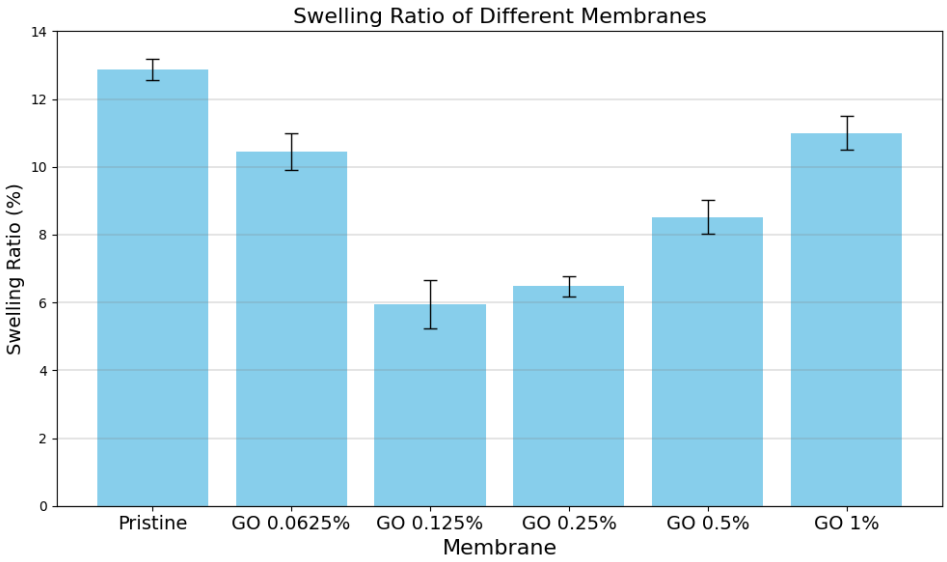

Figure 5.13: Swelling Ratio of membranes.

The trends observed from the figures indicate that water uptake initially increased with GO loading, peaking at 0.125%, before declining at higher concentrations, while the swelling ratio followed an opposite trend, decreasing initially until 0.125% GO and then rising. At 0.125% GO, both water uptake and dimensional stability were optimized, with a water uptake of approximately 17% (compared to 7% for the pristine membrane) and a swelling ratio of 6% (compared to 13% for the pristine membrane). This trend recurred across different batches and experimental sets, suggesting consistency in the behavior of the membranes under these conditions. Although the exact reasons behind these trends cannot be certain, several hypotheses are proposed, linking these observations to mechanical properties and IEC.

At lower GO concentrations (up to 0.125%), WU increases while the SR decreases. This can be attributed to GO's hydrophilicity, which attracts more water into the membrane and the increased compliance of the polymer structure. As previously mentioned, at these concentrations, GO likely disrupts the polymer structure and crystallinity, creating free volume, accommodating more water without excessive swelling. The increased mobility of polymer chains allows the structure to adjust, with GO forming uniform hydrophilic pathways that enable higher WU without significant swelling. Initially, the membrane structure consisted of a hydrophobic polymer backbone and cationic sites forming pathways, enhanced by phase separation from the block copolymer. The addition of GO creates a disrupted structure with a lower Young's modulus and hardness but greater WU and reduced swelling, as the hydrophilic channels efficiently manage water distribution and limit swelling despite the increased absorption.

As the GO concentration increases (0.25% and above), the WU decreases slightly, likely because GO shields the polymer's cationic sites responsible for water absorption. This coverage reduces the membrane's ability to take up water. Additionally, the membrane stiffens (as indicated by a higher modulus) and perhaps gains some crystallinity loosing free volume, limiting its ability to accommodate water. At even higher concentrations, such as 1%, agglomeration occurs, creating chunks of GO that reduce the available hydrophilic surface area and block ion channels.
Despite the reduction in WU, the SR still increases at higher GO concentrations. This could be due to the less uniform dispersion of GO, causing localized areas where water accumulates, leading to increased swelling, as shown in figure 5.14. The stiffer structure, due to the higher Young's modulus, prevents the membrane from evenly distributing water, which results in swelling. Furthermore, as GO content continues to rise and to agglomerate, blocked ion transport channels worse the inefficient water management, further contributing to swelling.

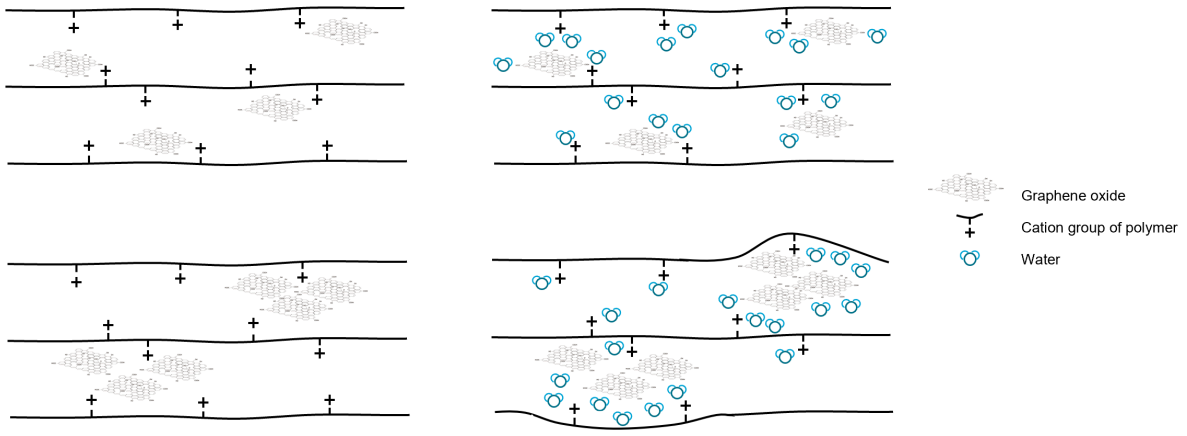

Figure 5.14: Effect of GO dispersion on swelling: (top) Homogeneously dispersed GO, (bottom) Non-homogeneously dispersed GO.

Literature on AEMs filled with GO presents widely varying results for WU and SR values. A study on IL-GO in an Im-PPO matrix showed the following trend: an increase in IEC with increasing GO percentages, accompanied by an initial increase and then a decrease in both WU and SR [126]. Other studies on GO in a polybenzimidazolium matrix reported a decrease in IEC with increasing GO, an initial increase in WU followed by a decrease, and an initially constant SR that later increased [21]. Another study on ImPSF with ImGO showed a constant IEC, with both WU and SR decreasing [77]. These trends are highly dependent on the specific interactions between the matrix and GO. Furthermore, most studies in the literature present results without proposing hypotheses to explain these observed trends. Comparing the WU and SR values from this study with those in the literature is not straightforward. Additionally, while the general measurement procedures for WU and SR are similar across research papers and studies, small variations, such as whether excess surface water is fully removed before measuring, can lead to significant differences in reported WU and SR values.

5.7.1. Post Electrolyzer

In addition to the standard swelling ratio (SR) and water uptake (WU) measurements taken after a 48-hour soaking period in 1M KOH, further parameters were evaluated for the membranes used in the electrolyzer. Specifically, membranes were remeasured for mass and thickness following electrolysis and compared to their pre-electrolysis, soaked state. This enabled the calculation of SR and WU post-electrolysis, which, though not commonly assessed in studies on novel AEMs, provided valuable insights into membrane behavior under operational conditions.

While the SR and WU post-electrolysis are calculated relative to the pre-electrolysis soaked state, the total SR and WU graphs present all values normalized to the same reference of dry membrane state, allowing direct comparison with the initial swelling and uptake measurements and offering a complete picture of membrane behavior across different conditions.

Figures 5.15 and 5.16 show the SR post electrolyser and the total SR of Batch 2. The same graphs are reported in appendix D.6.1 for Batch 1.

The observed difference in swelling and the significantly higher values post-electrolysis compared to swelling after soaking suggest two distinct conditions affecting water transport. During soaking, water uptake and swelling occur through passive diffusion, driven primarily by osmotic gradients. Membranes with lower Young's modulus, such as those with 0.0625% and 0.125% GO loadings, likely have more compliant polymer chains, increased free volume, and a more homogeneous GO dispersion. This structure allows these membranes to absorb and accommodate water efficiently while controlling excessive swelling.
In contrast, during electrolysis, an applied electric field provides an additional driving force. As solvated hydroxide ions travel from the cathode to the anode via migration, they drag water molecules along through electro-osmotic flow [26]. Under these conditions, stiffer membranes with higher GO content (0.25% and above) are better able to maintain their structural integrity, limiting swelling to around 27%

compared to 37% for the pristine membrane when comparing post-electrolysis to pre-electrolysis states. Softer membranes (0.0625% and 0.125% GO) exhibit somewhat greater swelling during electrolysis; however, they still perform better than the pristine membrane. This may be due to their previously observed ability to accommodate water more efficiently within their matrix.

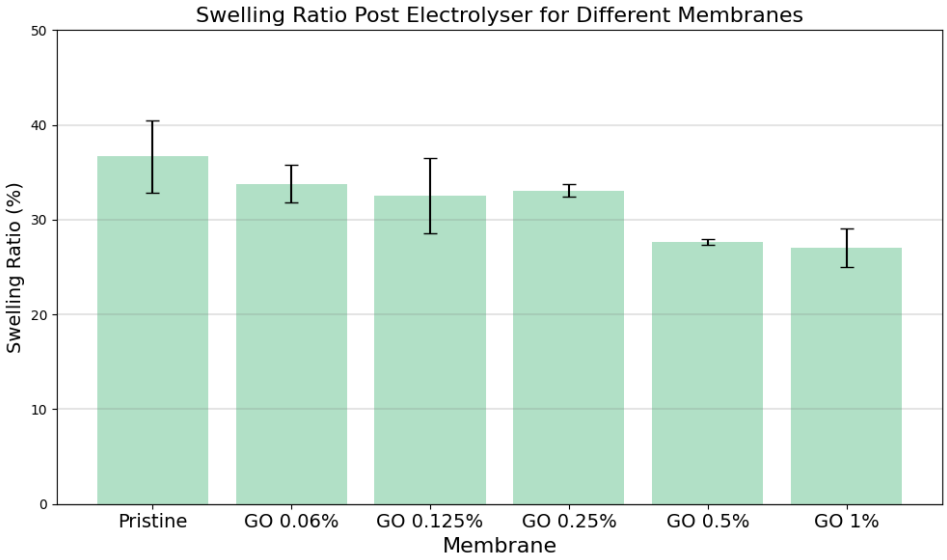

Figure 5.15: Swelling Ratio of membranes post-electrolyzer, calculated relative to the pre-electrolysis soaked state.

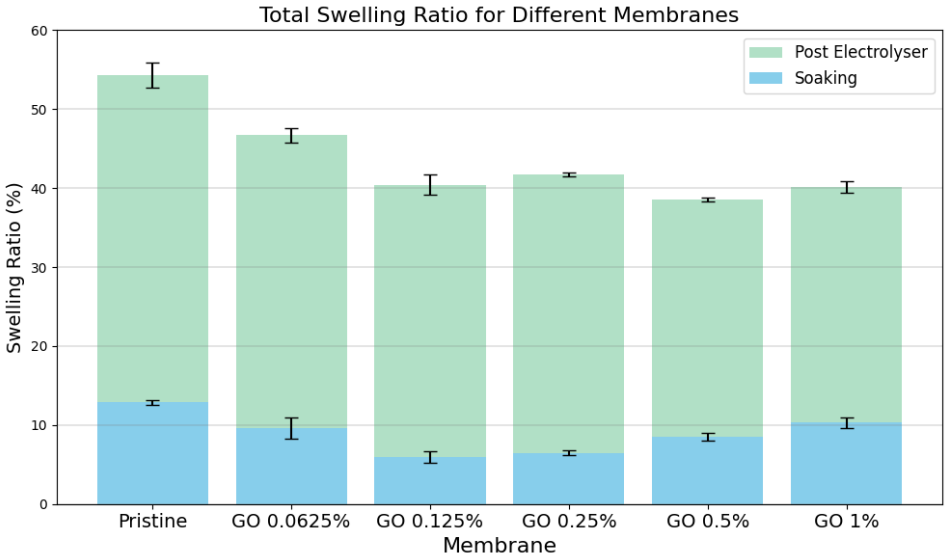

Figure 5.16: Total Swelling Ratio of membranes, normalized to the dry state.

Figure 5.16 reflects the combined effect of both tests, soaking and electrolysis, on the membranes, providing a complete view of the swelling behavior across the membrane's lifecycle. This includes the initial activation process (conversion from the iodine to hydroxide form) and subsequent operation under electrolysis conditions. While the 0.25% GO membrane shows the lowest swelling after soaking alone, the 0.5% GO membrane exhibits less swelling under electrolysis, where swelling is generally more pronounced. As a result, the 0.5% GO membrane achieves the lowest total swelling across both conditions, reducing total swelling from approximately 55% for the pristine membrane to 38%.

Figures 5.17 and 5.18 show the WU post electrolyzer and the total WU of Batch 2. The same graphs are reported in appendix D.6.1 for Batch 1.

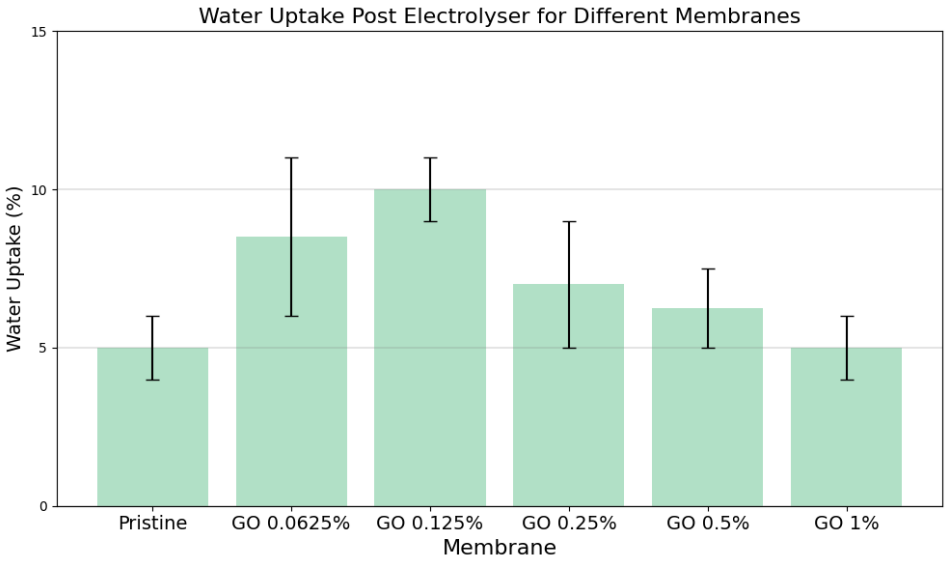

Figure 5.17: Water Uptake post electrolyzer of membranes, calculated relative to the pre-electrolysis soaked state.

The water uptake values post-electrolysis did not exhibit the substantial increases observed in the swelling ratio, indicating a more stable water content despite elevated swelling levels. This suggests that hydroxide ion migration and electro-osmotic drag primarily induce structural deformation rather than additional water retention within the membrane. Since the membranes are already hydrated following the soaking phase, they do not absorb significantly more water; instead, hydroxide migration through the polymer matrix results in increased expansion.

It should be noted that the differences in WU and SR after soaking in 1M KOH and post-electrolyzer are likely greater than represented. When the dry membrane is initially soaked in 1M KOH, it starts in its iodine form from synthesis; during soaking, it absorbs water, and iodine is exchanged for hydroxide ions. Since iodine ions are significantly larger and heavier than hydroxide ions, the actual thickness and mass variations after soaking in KOH are greater than measured. In contrast, for the membrane analysis pre- and post-electrolyzer, the membrane is already in its KOH form, providing a more precise measure of swelling and water uptake.

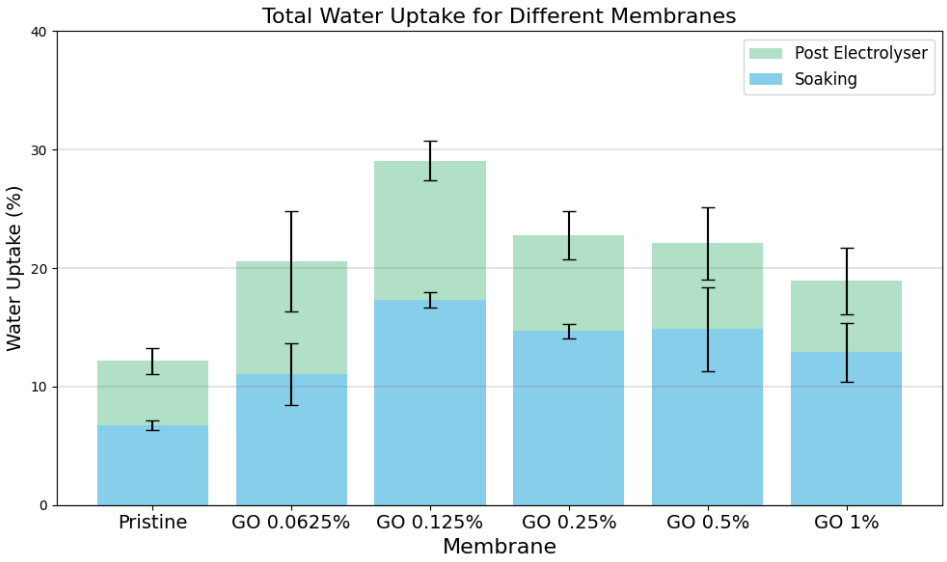

Figure 5.18: Total Water Uptake of membranes, normalized to the dry state.

5.8. Mechanism of Conductivity Enhancement

The previously reported tests provided insights into the effects of GO on membrane structure. SEM and AFM analyses explored surface and bulk morphology, nano-indentation examined surface and bulk mechanical properties, and water uptake and swelling ratio measurements assessed hydrophilicity and dimensional stability. Together, these trends informed the development of a hypothesis regarding the structural effects of GO on the membrane.
Based on these analyses, the following interpretation links the observed structural and mechanical changes to the conductivity behavior of the membranes, revealing GO's multifaceted impact on AEM.

Conductivity increases with GO loading up to 0.5%. Initially, this trend (up to 0.125%) is straightforward: higher water uptake boosts conductivity, as additional water enhances ion mobility [74]. Beyond 0.125%, however, the decrease in water uptake alongside improved ion conduction suggests that the existing water is being used more efficiently for transport, indicating GO's role in optimizing conduction mechanisms. Additionally, the observed increase in crystallinity, reflected by the rise in Young's modulus and Hardness after 0.125% GO, suggests a more organized structure, which may support more efficient ionic pathways and enhanced solvation shells for OH^- ions [41, 77].

The hydrophilic and oxygenated functional groups in GO can form hydrogen bonds with surrounding water molecules, facilitating ion hopping via the Grotthuss mechanism and expanding the hydrogen bond network that transports negative charge [83]. Furthermore, GO can act as a bridge between cationic sites, promoting OH^- conduction by providing an additional solvation network for vehicular transport [112]. The dual effect of structural organization and efficient water utilization underscores GO's role in optimizing conduction. Figure 5.19 illustrates GO's impact on hydroxide conduction, not only increasing water uptake due to its hydrophilicity but also utilizing this water more efficiently for transport.

At 1% GO, however, conductivity declines, likely due to GO agglomeration, which can block ion channels and disrupt the continuity of ion conduction pathways, thereby hindering transport efficiency [87].

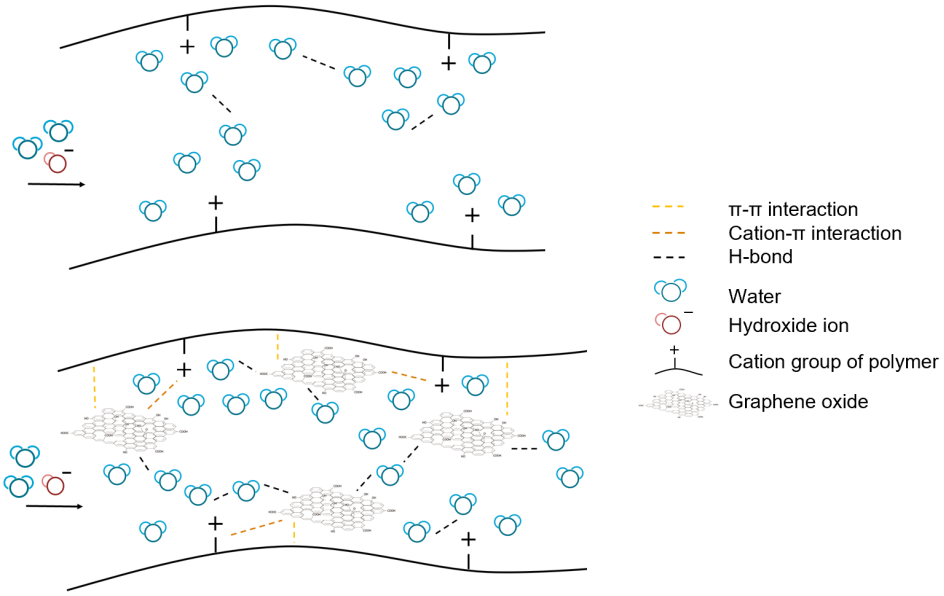

Figure 5.19: GO's effect on hydroxide ion conduction: (top) Ion pathway without GO, (bottom) Ion pathway with GO.

6

Conclusion

This research aimed to enhance the AEM properties of a poly(co-aryl piperidinium) polymer by incorporating GO as a nanofiller. The goal was to determine an optimal GO concentration that would improve the membrane's hydroxide ion conductivity and mechanical stability, advancing AEMWE's feasibility at scale.

A reproducible casting method for composite membranes required considerable optimization of solvent composition, drying conditions, and mixing techniques. Key improvements included using a 5% water-DMSO co-solvent to enhance polymer matrix-GO interaction and implementing a gentler thermal treatment to prevent phase separation. This refined procedure enabled consistent membrane fabrication across different GO loadings, ensuring reproducibility and reliable testing.

The conductivity testing revealed a marked improvement with the addition of GO, peaking at a concentration of 0.5%. Conductivity increased from 33 mS/cm in the pristine membrane to 59 mS/cm at the optimal GO concentration, before declining at 1% loading. This trend suggests that optimal filler loadings enhance hydroxide conductivity by actively supporting efficient ion-conducting pathways, while agglomeration at higher concentrations reduces effectiveness.

The IEC showed little significant variation across different GO concentrations, though a slight decrease was observed as GO content increased, likely due to GO replacing portions of the polymer that contain cationic sites and GO's oxygenated groups partially neutralizing some of these sites. Despite this, the observed conductivity gains suggest that GO improves the membrane's structural and actively contributes to efficient water management properties.

Electrolyzer performance testing showed that current densities followed the trends observed in conductivity, though thickness variations across different GO loadings influenced absolute values. Membranes with higher conductivity also demonstrated improved current densities when normalized for conductance, emphasizing the role of optimized ion transport pathways in overall AEMWE performance.

Microscopic and thermal analyses (SEM, AFM, and TGA) confirmed that GO was homogeneously embedded at low to moderate concentrations, creating a smooth morphology without visible agglomeration. At higher concentrations (1%), however, agglomeration was observed, which likely contributed to the decline in conductivity and dimensional stability.

Nano-indentation results showed an initial decrease in hardness and Young's modulus at low GO concentrations (0.0625% to 0.125%), with both parameters increasing at higher loadings (0.5% to 1%). This trend might suggest that low GO concentrations may disrupt the polymer structure, introducing free volume and reducing stiffness, whereas higher GO loadings provide structural reinforcement and promote crystallinity.

Water uptake initially increased with GO loading, peaking at 0.125%, before declining at higher concentrations, while the swelling ratio followed an opposite trend, decreasing initially and then rising. At 0.125% GO, both water uptake and dimensional stability were optimized, likely due to a more homo-

geneous dispersion and compliant membrane structure allowing efficient water management. Post-electrolysis, swelling increased across samples, though this effect lessened at higher GO loadings, where swelling was most effectively controlled. Stable water uptake and limited swelling at higher GO content indicate that these membranes maintain dimensional stability more effectively under operational conditions.

In conclusion, this research successfully developed a reproducible casting procedure for incorporating GO as a nanofiller in poly(co-aryl piperidinium) membranes. Testing demonstrated that ion conductivity and mechanical stability were significantly enhanced with GO integration. At a 0.125% loading, the membrane achieved optimal swelling ratio and water uptake values, increasing water uptake from 7% to 17% and reducing swelling from 13% to 6% compared to the pristine membrane. The 0.5% GO loading yielded the highest electrolyzer performance, nearly doubling hydroxide conductivity from 33 mS/cm in the pristine membrane to 59 mS/cm, while also minimizing the post-electrolysis swelling ratio to 27% compared to 37% in the pristine membrane, establishing this composition as a promising candidate for efficient AEMWE applications.

7

Recommendations and Outlook

This research demonstrated the potential of GO as a filler to enhance poly(co-aryl piperidinium) membranes for AEMWE applications, specifically improving ion conductivity and mechanical stability. Building on these findings, future work could be divided into areas that could further refine the current study and broader directions that expand on the approach and technique for GO-enhanced AEMs in general.

Immediate extensions to the current study

- **Evaluating alkaline stability:** While this study focused on enhancing ion conductivity and mechanical stability, another essential property for AEM performance in AEMWE applications is long-term alkaline stability. As a next step, verifying improvements in alkaline stability with GO integration would provide a more comprehensive performance assessment. Conductivity retention tests after extended KOH exposure (10–200 hours) would provide essential benchmarks. Studies on QPPO/PSF with GO have indicated promising retention rates, with up to 90% conductivity maintained after 200 hours for 2% GO compared to lower rates for pristine membranes, suggesting GO's role in enhancing longevity [83].
- **Testing at operational temperatures with catalysts:** Conducting electrochemical cell testing at typical operational temperatures (e.g., 60°C) with an integrated catalyst layer would provide performance data more representative of industrial conditions. This approach would allow for a direct assessment of the membrane's behavior under realistic working environments, enabling meaningful comparisons with existing literature and industry benchmarks.
- **Mechanical characterization in operational conditions:** Evaluating the mechanical properties of KOH-activated, wet-state membranes via nano-indentation before electrolyzer testing would provide a more realistic assessment of operational behavior. Additionally, post-electrolyzer SEM cross-sectional analysis could reveal structural changes, clarifying swelling and water uptake mechanisms.
- **Structural analysis for crystallinity:** Further analysis to assess changes in polymer structure and crystallinity induced by GO integration would clarify the underlying performance improvements. Techniques such as X-ray diffraction (XRD) and wide-angle X-ray scattering (WAXS) would perhaps be effective for assessing crystallinity changes.
- **Testing with recycled polymer:** Lastly, in today's society, recyclability is an increasingly valued attribute in material design. During the development of a successful casting procedure for GO-enhanced poly(co-aryl piperidinium) membranes, recycled polymer was also used, as detailed in the appendix B, with the procedure demonstrating effectiveness for this polymer source as well. To determine if recycled pristine membranes could be viable for future applications of these GO-filled membranes, it would be essential to test their performance and evaluate if they retain the desired properties.

Broader directions for future research

- **Functionalization of GO for enhanced polymer interaction:** Functionalizing GO with aromatic chains would improve π-π interactions with the poly(co-aryl piperidinium) matrix, enabling higher GO loadings without agglomeration and enhancing conductivity. Additionally, cationic functional groups, such as imidazolium-functionalized GO, could also increase IEC without excessive swelling, further enhancing conductivity and dimensional stability [77, 126].
- **Use of monolayer GO for increased surface area:** Employing monolayer GO instead of multilayered forms would increase the surface-area-to-volume ratio, promoting better dispersion within the polymer. This could support higher loadings while minimizing agglomeration, allowing for further conductivity improvements.
- **Integration with electric field-assisted casting:** Combining electric field-assisted casting with GO-enhanced membranes could facilitate ion channel alignment, further boosting conductivity. GO's moderate electrical conductivity allows compatibility with this technique, potentially enhancing ion transport pathways while preventing short-circuiting risks.
- **Impedance spectroscopy to analyze resistance components:** If observed current densities do not correspond with expected conductivity values, impedance spectroscopy could provide valuable insights into the various resistive components in the system [118]. This technique could help determine if, for instance, ohmic resistance is decreasing while other resistances, such as charge transfer or interfacial resistances, are increasing.
- **Evaluation of gas crossover and selectivity:** Future studies could assess gas crossover to measure efficiency and hydrogen purity in AEMWE, using techniques such as gas chromatography. While primarily a focus in fuel cell research, gas selectivity also benefits AEMWE by potentially enhancing hydrogen purity. Prior studies indicate that GO reduces methanol permeability in fuel cell applications and increases permselectivity in electrodialysis, suggesting similar benefits in AEMWE [83, 21].

References

[1] Michael M Aba, Ildo Luís Sauer, and Nilton Bispo Amado. “Comparative review of hydrogen and electricity as energy carriers for the energy transition”. In: *International Journal of Hydrogen Energy* 57 (2024), pp. 660–678.

[2] Vira Agieienko, Vadim Neklyudov, and Ayrat Dimiev. “Solvent-induced changes in the graphene oxide absorption spectrum. The case of dimethylsulfoxide/water mixtures”. In: *Journal of Molecular Liquids* 287 (2019), p. 110942.

[3] Rana Tariq Mehmood Ahmad et al. “Water-assisted stable dispersal of graphene oxide in non-dispersible solvents and skin formation on the GO dispersion”. In: *Carbon* 98 (2016), pp. 188–194.

[4] Juan Amaro-Gahete et al. “A comparative study of particle size distribution of graphene nanosheets synthesized by an ultrasound-assisted method”. In: *Nanomaterials* 9.2 (2019), p. 152.

[5] Kalaivanan Shanmugam Anandan. “Anion Exchange Membrane Optimization: Applying AC Electric Field to Create ”Ion Highways””. Supervised by Dr. H. Hazyar, Dr. D. A. Vermaas, and Dr. A. Hunt. Master of Science Thesis. Delft, Netherlands: Delft University of Technology, May 2024.

[6] Iyappan Arunkumar et al. “Enhanced fumion nanocomposite membranes embedded with graphene oxide as a promising anion exchange membrane for fuel cell application”. In: *International Journal of Hydrogen Energy* (2022).

[7] Ramesh Bhandari and Niroj Adhikari. “A comprehensive review on the role of hydrogen in renewable energy systems”. In: *International Journal of Hydrogen Energy* 82 (2024), pp. 923–951.

[8] Alexander Buttler and Hartmut Spliethoff. “Current status of water electrolysis for energy storage, grid balancing and sector coupling via power-to-gas and power-to-liquids: A review”. In: *Renewable and Sustainable Energy Reviews* 82 (2018), pp. 2440–2454.

[9] T Capurso et al. “Perspective of the role of hydrogen in the 21st century energy transition”. In: *Energy Conversion and Management* 251 (2022), p. 114898.

[10] Marian Chatenet et al. “Water electrolysis: from textbook knowledge to the latest scientific strategies and industrial developments”. In: *Chemical society reviews* 51.11 (2022), pp. 4583–4762.

[11] Chen Chen et al. “Hydroxide solvation and transport in anion exchange membranes”. In: *Journal of the American Chemical Society* 138.3 (2016), pp. 991–1000.

[12] et al. Chen. “Investigating Graphene Oxide Sheets”. In: *Scientific Reports* 13.1 (2023), p. 33350. DOI: 10.1038/s41598-023-33350-5.

[13] Junlang Chen et al. “Molecular insights into the dispersion stability of graphene oxide in mixed solvents: Theoretical simulations and experimental verification”. In: *Journal of colloid and interface science* 571 (2020), pp. 109–117.

[14] Nanjun Chen et al. “Poly(fluorenyl aryl piperidinium) membranes and ionomers for anion exchange membrane fuel cells”. In: *Nature Communications* 12.1 (2021), pp. 1–9. DOI: 10.1038/s41467-021-22612-3.

[15] Nanjun Chen et al. “Chemically & physically stable crosslinked poly (aryl-co-aryl piperidinium) s for anion exchange membrane fuel cells”. In: *Journal of Membrane Science* 638 (2021), p. 119685.

[16] Nanjun Chen et al. “Di-piperidinium-crosslinked poly (fluorenyl-co-terphenyl piperidinium) s for high-performance alkaline exchange membrane fuel cells”. In: *Journal of Materials Chemistry A* 10.7 (2022), pp. 3678–3687.

[17] Nanjun Chen et al. “High-performance anion exchange membrane water electrolyzers with a current density of 7.68 A cm- 2 and a durability of 1000 hours”. In: *Energy & environmental science* 14.12 (2021), pp. 6338–6348.

[18] Nanjun Chen et al. “Poly (alkyl-terphenyl piperidinium) ionomers and membranes with an outstanding alkaline-membrane fuel-cell performance of 2.58 W cm- 2”. In: *Angewandte Chemie International Edition* 60.14 (2021), pp. 7710–7718.

[19] Ji Young Chu et al. “Graphene-mediated organic-inorganic composites with improved hydroxide conductivity and outstanding alkaline stability for anion exchange membranes”. In: *Composites Part B: Engineering* 164 (2019), pp. 324–332.

[20] Jonathan Clayden et al. *Organic Chemistry*. 2nd. Oxford University Press, 2012.

[21] Levente Cseri et al. “Graphene oxide–polybenzimidazolium nanocomposite anion exchange membranes for electrodialysis”. In: *Journal of Materials Chemistry A* 6 (2018), pp. 24728–24739. DOI: 10.1039/C8TA09160A.

[22] Ronald P. D’Amelia and Brandon Khanyan. “An Experimental Review: Evaluation of the Flory-Fox Equation for the Relationship of Glass Transition Temperature (Tg) vs Molar Mass of Polystyrene Using Differential Scanning Calorimetry (DSC)”. In: *Journal of Polymer and Biopolymer Physics Chemistry* 10.1 (2022), pp. 10–17. DOI: 10.12691/jpbpc-10-1-2.

[23] RD Deegan, O Bakajin, TF Dupont, et al. “Capillary flow as the cause of ring stains from dried liquid drops”. In: *Nature* 592 (2021), E12. DOI: 10.1038/s41586-021-03444-z.

[24] University of Washington Department of Electrical Engineering. *Electro-optic Modulator*. Accessed: 2024-09-30. 2024. URL: https://depts.washington.edu/eooptic/.

[25] Madushani Dharmarwardana et al. “Strong π-stacking causes unusually large anisotropic thermal expansion and thermochromism”. In: *Proceedings of the National Academy of Sciences* 118.44 (2021), e2106572118.

[26] Naiying Du et al. “Anion-exchange membrane water electrolyzers”. In: *Chemical reviews* 122.13 (2022), pp. 11830–11895.

[27] Wencheng Du et al. “Graphene oxide in aqueous and nonaqueous media: Dispersion behaviour and solution chemistry”. In: *Carbon* 158 (2020), pp. 568–579.

[28] Hanzhao Duan et al. “Achieving high conductivity at low ion exchange capacity for anion exchange membranes with electrospun polyelectrolyte nanofibers”. In: *ACS Applied Energy Materials* 3.11 (2020), pp. 10660–10668.

[29] Jasna Đurović. “Development of Novel Anion Exchange Membranes for Alkaline Water Electrolysis with Employment of DC Electric Field”. Supervised by Asst. Prof. Hanieh Bazyar and Postdoc Thanos Papageorgiou. Master of Science Thesis. Delft, Netherlands: Delft University of Technology, Faculty of Applied Sciences, June 2024.

[30] Sina Ebnesajjad. *Chemical Resistance of Engineering Thermoplastics*. Plastics Design Library. Introduction to Plastics. Elsevier, 2016, pp. xiii–xxv. DOI: 10.1016/B978-0-323-47357-6.00021-0.

[31] Sina Ebnesajjad. “Surface and material characterization techniques”. In: *Handbook of adhesives and surface preparation*. Elsevier, 2011, pp. 31–48.

[32] Vijayakumar Elumalai and Dharmalingam Sangeetha. “Synergic effect of ionic liquid grafted titanate nanotubes on the performance of anion exchange membrane fuel cell”. In: *Journal of Power Sources* 412 (2019), pp. 586–596.

[33] European Commission. *Progress on Climate Action*. Accessed: 2024-10-25. 2023. URL: https://climate.ec.europa.eu/eu-action/climate-strategies-targets/progress-climate-action_en.

[34] European Commission. *Renewable Energy Directive Targets and Rules*. Accessed: 2024-10-25. 2023. URL: https://energy.ec.europa.eu/topics/renewable-energy/renewable-energy-directive-targets-and-rules/renewable-energy-directive_en.

[35] European Environment Agency. *Share of Energy Consumption from Renewable Sources in Europe*. Accessed: 2024-10-25. 2022. URL: https://www.eea.europa.eu/en/analysis/indicators/share-of-energy-consumption-from.

[36] University of Hamburg Faculty of Chemistry. *Solvents*. Accessed: 2024-09-30. 2024. URL: https://www-archiv.fdm.uni-hamburg.de/b-online/library/newton/Chy251_253/Lectures/Solvents/Solvents.html.

[37] Usaid R Farooqui, Abdul Latif Ahmad, and NA Hamid. "Graphene oxide: A promising membrane material for fuel cells". In: *Renewable and Sustainable Energy Reviews* 82 (2018), pp. 714–733.

[38] Silvia Favero, Ifan EL Stephens, and Maria-Magdalena Titirci. "Anion Exchange Ionomers: Design Considerations and Recent Advances-An Electrochemical Perspective". In: *Advanced Materials* 36.8 (2024), p. 2308238.

[39] Fabrizia Foglia et al. "Disentangling water, ion and polymer dynamics in an anion exchange membrane". In: *Nature Materials* 21.5 (2022), pp. 555–563.

[40] Florian Frieden and Jens Leker. "Future costs of hydrogen: a quantitative review". In: *Sustainable Energy & Fuels* (2024).

[41] Xiao Fu et al. "Graphene oxide as a promising nanofiller for polymer composite". In: *Surfaces and Interfaces* 37 (2023), p. 102747.

[42] Wei Gao. "The chemistry of graphene oxide". In: *Graphene oxide: reduction recipes, spectroscopy, and applications* (2015), pp. 61–95.

[43] Chunli Gong et al. "Hierarchical layered double hydroxide coated carbon nanotube modified quaternized chitosan/polyvinyl alcohol for alkaline direct methanol fuel cells". In: *Journal of Power Sources* 441 (2019), p. 227176.

[44] Taylor & Francis Group. *CRC Press*. Printed in the United States of America on acid-free paper. Boca Raton, FL: Taylor & Francis Group, LLC, 2011. ISBN: 978-1-4200-6930-3.

[45] Rui Guo et al. "Hydrogen Bond Regulating Miscibility of Graphene Oxide and Nonionic Water-Soluble Polymers". In: *Nanoscale* (2024).

[46] Kimberly FL Hagesteijn, Shanxue Jiang, and Bradley P Ladewig. "A review of the synthesis and characterization of anion exchange membranes". In: *Journal of materials science* 53.16 (2018), pp. 11131–11150.

[47] Anwar Ul-Hamid. *A Beginners' Guide to Scanning Electron Microscopy*. 1st. Springer, 2018. ISBN: 9783319984810. DOI: 10.1007/978-3-319-98482-7.

[48] Yingting Hang et al. "Mechanical properties and interfacial adhesion of composite membranes probed by in-situ nano-indentation/scratch technique". In: *Journal of Membrane Science* 494 (2015), pp. 205–215.

[49] A. Hirohata et al. "Non-destructive imaging of buried interfaces using decelerated electron-beam in scanning electron microscopy". In: *Non-Destructive Material Characterization Methods*. Elsevier, 2024, pp. 127–149.

[50] Maša Hren et al. "Alkaline membrane fuel cells: anion exchange membranes and fuels". In: *Sustainable Energy & Fuels* 5.3 (2021), pp. 604–637.

[51] Chuan Hu et al. "Effects of hydrophobic side chains in poly (fluorenyl-co-aryl piperidinium) ionomers for durable anion exchange membrane fuel cells". In: *Journal of Materials Chemistry A* 11.4 (2023), pp. 2031–2041.

[52] Daxing Hua et al. "Development of anion exchange membrane water electrolysis and the associated challenges: a review". In: *ChemElectroChem* 10.1 (2023), e202200999.

[53] Infinitab Lab. *Three Methods to Determine Polymer Hardness*. Accessed: 2024-10-25. 2023.

[54] Institute for Energy Research. *2023 Set Records in Global Fossil Fuel Use and Carbon Dioxide Emissions*. Accessed: 2024-10-25. 2023. URL: https://www.instituteforenergyresearch.org/international-issues/2023-set-records-in-global-fossil-fuel-use-and-carbon-dioxide-emissions/.

[55] International Energy Agency. *Global Hydrogen Review 2023: Executive Summary*. Accessed: 2024-10-25. 2023. URL: https://www.iea.org/reports/global-hydrogen-review-2023/executive-summary.

[56] International Energy Agency. *World Energy Outlook 2023: Pathways for the Energy Mix*. Accessed: 2024-10-25. 2023. URL: https://www.iea.org/reports/world-energy-outlook-2023/pathways-for-the-energy-mix.

[57] Hiroshi Ito et al. “Properties of Nafion membranes under PEM water electrolysis conditions”. In: *International journal of hydrogen energy* 36.17 (2011), pp. 10527–10540.

[58] E Jaafar et al. “Study on morphological, optical and electrical properties of graphene oxide (GO) and reduced graphene oxide (rGO)”. In: *Materials Science Forum*. Vol. 917. Trans Tech Publ. 2018, pp. 112–116.

[59] Jae-Hun Kim et al. “Preparation of high-conductivity QPPO (quaternary-aminated poly (2, 6-dimethyl-1, 4-phenyleneoxide)) membranes by electrical treatment”. In: *Journal of Membrane Science* 553 (2018), pp. 82–89.

[60] Dimitrios Konios et al. “Dispersion behaviour of graphene oxide and reduced graphene oxide”. In: *Journal of colloid and interface science* 430 (2014), pp. 108–112.

[61] S Shiva Kumar and Hankwon Lim. “An overview of water electrolysis technologies for green hydrogen production”. In: *Energy reports* 8 (2022), pp. 13793–13813.

[62] S. Kwon et al. “The Effect of Thickness and Chemical Reduction of Graphene Oxide on Nanoscale Friction”. In: *The Journal of Physical Chemistry B* 122.2 (2017), pp. 543–547. DOI: 10.1021/acs.jpcb.7b04609.

[63] Van Thanh Le et al. “Effects of ultrasonication on graphene oxide: A study on lateral size, thickness and degree of oxidation”. In: *Separation and Purification Technology* 209 (2019), pp. 307–316. DOI: 10.1016/j.seppur.2018.07.016.

[64] HJ Lee et al. “The mechanical properties of thin polymer film for nanoimprinting lithography by nanoindentation”. In: *2003 Third IEEE Conference on Nanotechnology, 2003. IEEE-NANO 2003.* Vol. 2. IEEE. 2003, pp. 546–549.

[65] Sangmin Lee et al. “Nanoindentation of annealed Naf ion/sulfonated graphene oxide nanocomposite membranes for the measurement of mechanical properties”. In: *Journal of membrane science* 451 (2014), pp. 40–45.

[66] Sol A Lee et al. “Anion exchange membrane water electrolysis for sustainable large-scale hydrogen production”. In: *Carbon Neutralization* 1.1 (2022), pp. 26–48.

[67] Markus Lehner et al. *Power-to-gas: technology and business models*. Springer, 2014.

[68] Wen-Hua Li et al. “Conductive MOFs”. In: *EnergyChem* 2.2 (2020), p. 100029.

[69] Xiaodong Li and Bharat Bhushan. “A review of nanoindentation continuous stiffness measurement technique and its applications”. In: *Materials characterization* 48.1 (2002), pp. 11–36.

[70] Cong Liu et al. “Towards basic ionic liquid-based hybrid membranes as hydroxide-conducting electrolytes under low humidity conditions”. In: *Chemical Communications* 51.63 (2015), pp. 12629–12632.

[71] L. Liu et al. “Enhanced properties of quaternized graphenes reinforced polysulfone based composite anion exchange membranes for alkaline fuel cell”. In: *Journal of membrane science* 487 (2015), pp. 99–108.

[72] Lingdi Liu et al. “Novel quaternized mesoporous silica nanoparticle modified polysulfone-based composite anion exchange membranes for alkaline fuel cells”. In: *RSC Advances* 5.54 (2015), pp. 43381–43390.

[73] Lizhao Liu et al. “Mechanical properties of graphene oxides”. In: *Nanoscale* 4.19 (2012), pp. 5910–5916.

[74] Lu Liu et al. “Recent Advances and Challenges in Anion Exchange Membranes Development/Application for Water Electrolysis: A Review”. In: *Membranes* 14.4 (2024), p. 85.

[75] Yanxiang Liu et al. “Hybrid anion exchange membrane of hydroxyl-modified polysulfone incorporating guanidinium-functionalized graphene oxide”. In: *Ionics* 23 (2017), pp. 3085–3096.

[76] Malvern Panalytical. *Dynamic Light Scattering: An Introduction in 30 minutes*. Accessed: 2024-10-02. 2020. URL: https://www.malvernpanalytical.com/en/learn/knowledge-center/technical-notes/TN101104DynamicLightScatteringIntroduction.

[77] Xunli Mao et al. “Enhancing hydroxide conductivity of anion exchange membrane via incorporating densely imidazolium functionalized graphene oxide”. In: *Solid State Ionics* 333 (2019), pp. 83–92.

[78] Peter Mardle, Binyu Chen, and Steven Holdcroft. “Opportunities of Ionomer Development for Anion-Exchange Membrane Water Electrolysis: Focus Review”. In: *ACS Energy Letters* 8.8 (2023), pp. 3330–3342.

[79] McKinsey & Company. *Global Energy Perspective 2023: Hydrogen Outlook*. Accessed: 2024-10-25. 2023. URL: https://www.mckinsey.com/industries/oil-and-gas/our-insights/global-energy-perspective-2023-hydrogen-outlook.

[80] Yongqiang Ming et al. “Polymer Nanocomposites: Role of modified filler content and interfacial interaction on crystallization”. In: *European Polymer Journal* 162 (2022), p. 110894.

[81] Félix Mouhat, François-Xavier Coudert, and Marie-Laure Bocquet. “Structure and chemistry of graphene oxide in liquid water from first principles”. In: *Nature communications* 11.1 (2020), p. 1566.

[82] Adrian P Mouritz. “Mechanical and durability testing of aerospace materials”. In: *Introduction to aerospace materials. Woodhead Publishing* (2012), pp. 91–127.

[83] Phumlani F Msomi et al. “Quaternized poly (2.6 dimethyl–1.4 phenylene oxide)/Polysulfone anion exchange membrane reinforced with graphene oxide for methanol alkaline fuel cell application”. In: *Journal of polymer research* 25 (2018), pp. 1–12.

[84] Omid Nabinejad et al. “Determination of filler content for natural filler polymer composite by thermogravimetric analysis”. In: *Journal of Thermal Analysis and Calorimetry* 122 (2015), pp. 227–233.

[85] F Najafi and M Rajabi. “Thermal gravity analysis for the study of stability of graphene oxide–glycine nanocomposites”. In: *International Nano Letters* 5 (2015), pp. 187–190.

[86] Têko W. Napporn et al. “Electrochemical Measurement Methods and Characterization on the Cell Level”. In: *Fuel Cells and Hydrogen: From Fundamentals to Applied Research*. Elsevier, 2018, pp. 175–214. DOI: 10.1016/B978-0-12-811459-9.00009-8.

[87] Riccardo Narducci et al. “Anion exchange membranes with 1D, 2D and 3D fillers: A review”. In: *Polymers* 13.22 (2021), p. 3887.

[88] National Center for Biotechnology Information. *PubChem Compound Summary for CID 679, Dimethyl sulfoxide (DMSO)*. Accessed: 2024-10-01. 2024. URL: https://pubchem.ncbi.nlm.nih.gov/compound/Dimethyl-Sulfoxide#section=CSL-Reaction-Information.

[89] H. M. Ng et al. “Thermogravimetric Analysis of Polymers”. In: *Encyclopedia of Polymer Science and Technology* (2018). URL: https://doi.org/10.1002/0471440264.pst667.

[90] Joel S Olsson, Thanh Huong Pham, and Patric Jannasch. “Poly (arylene piperidinium) hydroxide ion exchange membranes: synthesis, alkaline stability, and conductivity”. In: *Advanced Functional Materials* 28.2 (2018), p. 1702758.

[91] Our World in Data. *Energy Mix*. Accessed: 2024-10-25. 2023. URL: https://ourworldindata.org/energy-mix.

[92] Ramón Pamies et al. “Determination of intrinsic viscosities of macromolecules and nanoparticles. Comparison of single-point and dilution procedures”. In: *Colloid and Polymer Science* 286 (2008), pp. 1223–1231.

[93] Grzegorz Pawelec. *Hydrogen Europe Presentation: Item 6 - Hydrogen Costs and Market Dynamics*. Accessed: 2024-10-25. United Nations Economic Commission for Europe. 2023.

[94] Shengjie Peng. *Electrochemical Hydrogen Production from Water Splitting: Basic, Materials and Progress*. Springer Nature, 2023.

[95] Robert Phillips and Charles W Dunnill. “Zero gap alkaline electrolysis cell design for renewable energy storage as hydrogen gas”. In: *RSC advances* 6.102 (2016), pp. 100643–100651.

[96] Aude Pommeret and Katheline Schubert. “Optimal energy transition with variable and intermittent renewable electricity generation”. In: *Journal of Economic Dynamics and Control* 134 (2022), p. 104273.

[97] Philippe Poulin et al. “Superflexibility of graphene oxide”. In: *Proceedings of the National Academy of Sciences* 113.40 (2016), pp. 11088–11093.

[98] Ming Qiu et al. “Preparation of anion exchange membrane with enhanced conductivity and alkaline stability by incorporating ionic liquid modified carbon nanotubes”. In: *Journal of Membrane Science* 573 (2019), pp. 1–10.

[99] Christopher J Quarton et al. “The curious case of the conflicting roles of hydrogen in global energy scenarios”. In: *Sustainable energy & fuels* 4.1 (2020), pp. 80–95.

[100] Marya Raji et al. “Chemical Preparation and Functionalization Techniques of Graphene and Graphene Oxide”. In: *Functionalized Graphene Nanocomposites and Their Derivatives*. Elsevier, 2019. Chap. 1, pp. 1–20. DOI: 10.1016/B978-0-12-814548-7.00001-5.

[101] Somayyeh Rakhshani et al. “Electrospinning of Polysulphone to Fabricate Anion Exchange Membrane for Cost-Effective Water Electrolysis”. In: *2023 IEEE International Conference on Environment and Electrical Engineering and 2023 IEEE Industrial and Commercial Power Systems Europe (EEEIC/I&CPS Europe)*. IEEE. 2023, pp. 1–4.

[102] K Rambabu et al. “ZrO2 incorporated polysulfone anion exchange membranes for fuel cell applications”. In: *International journal of hydrogen energy* 45.54 (2020), pp. 29668–29680.

[103] Asha Raveendran, Mijun Chandran, and Ragupathy Dhanusuraman. “A comprehensive review on the electrochemical parameters and recent material development of electrochemical water splitting electrocatalysts”. In: *RSC advances* 13.6 (2023), pp. 3843–3876.

[104] Seungbo Ryu et al. “Investigation of the effects of electric fields on the nanostructure of Nafion and its proton conductivity”. In: *Journal of Materials Chemistry A* 6.42 (2018), pp. 20836–20843.

[105] George Sakellariou, Aikaterini Siakali-Kioulafa, and Nikos Hadjichristidis. “Synthesis, chain flexibility, and glass-transition temperature of poly (2, 2-diphenylethyl methacrylate)”. In: *International Journal of Polymer Analysis and Characterization* 8.4 (2003), pp. 269–277.

[106] Carlo Santoro et al. “What is next in anion-exchange membrane water electrolyzers? Bottlenecks, benefits, and future”. In: *ChemSusChem* 15.8 (2022), e202200027.

[107] Prabhu Saravanan et al. “An overview of water electrolysis technologies for the production of hydrogen”. In: *New Dimensions in Production and Utilization of Hydrogen* (2020), pp. 161–190.

[108] Mostafa El-Shafie. “Hydrogen production by water electrolysis technologies: A review”. In: *Results in Engineering* (2023), p. 101426.

[109] Jinfeng Shao. “Evaluation of π-π interactions in proteins using Trp analogs: From protein labeling to quantitating the energies involved”. PhD thesis. Groningen: University of Groningen, 2016. ISBN: 978-90-367-9207-3. URL: https://doi.org/10.33612/diss.920206.

[110] Neeraj Sharma et al. “Study of optical and electrical properties of graphene oxide”. In: *Materials Today: Proceedings* 36 (2021), pp. 730–735.

[111] Tom Smolinka et al. “The history of water electrolysis from its beginnings to the present”. In: *Electrochemical power sources: fundamentals, systems, and applications*. Elsevier, 2022, pp. 83–164.

[112] N. S. Suhaimin et al. “Nanocomposite membrane by incorporating graphene oxide in sulfonated polyether ether ketone for direct methanol fuel cell”. In: *Materials Today: Proceedings* 46 (2021), pp. 2084–2091.

[113] Agilent Technologies. *An Introduction to Gel Permeation Chromatography and Size Exclusion Chromatography*. Guide No. 5990-6969EN. 2009. URL: https://www.agilent.com/library/primers/public.

[114] Ramato A Tufa et al. “Transport and Conductive Mechanisms in Anion Exchange Membranes”. In: *Alkaline Anion Exchange Membranes for Fuel Cells: From Tailored Materials to Novel Applications* (2024), pp. 125–142.

[115] United Nations Framework Convention on Climate Change. *Key Aspects of the Paris Agreement*. Accessed: 2024-10-25. 2015. URL: https://unfccc.int/most-requested/key-aspects-of-the-paris-agreement.

[116] Mark R VanLandingham et al. “Nanoindentation of polymers: an overview”. In: *Macromolecular symposia*. Vol. 167. 1. Wiley Online Library. 2001, pp. 15–44.

[117] Immanuel Vincent and Dmitri Bessarabov. “Low cost hydrogen production by anion exchange membrane electrolysis: A review”. In: *Renewable and Sustainable Energy Reviews* 81 (2018), pp. 1690–1704.

[118] Immanuel Vincent, Eun-Chong Lee, and Hyung-Man Kim. “Comprehensive impedance investigation of low-cost anion exchange membrane electrolysis for large-scale hydrogen production”. In: *Scientific reports* 11.1 (2021), p. 293.

[119] Ho Hyun Wang et al. “Reinforced poly (fluorenyl-co-terphenyl piperidinium) anion exchange membranes for fuel cells”. In: *Journal of Membrane Science* 644 (2022), p. 120160.

[120] Xiuqin Wang. “Poly(arylene piperidinium)-based anion exchange membranes for water electrolysis”. PhD Thesis. PhD thesis. Enschede: University of Twente, 2022. ISBN: 978-90-365-5427-5. URL: https://research.utwente.nl/en/publications/polyarylene-piperidinium-based-anion-exchange-membranes-for-water-electrolysis.

[121] Gede Herry Arum Wijaya, Kwang Seop Im, and Sang Yong Nam. “Advancements in commercial anion exchange membranes: A review of membrane properties in water electrolysis applications”. In: *Desalination and Water Treatment* (2024), p. 100605.

[122] Xingyu Wu et al. “Branched poly (aryl piperidinium) membranes for anion-exchange membrane fuel cells”. In: *Angewandte Chemie* 134.7 (2022), e202114892.

[123] Renxuan Xie et al. “Glass transition temperature from the chemical structure of conjugated polymers”. In: *Nature communications* 11.1 (2020), p. 893.

[124] Fei Xu, Yue Su, and Bencai Lin. “Progress of alkaline anion exchange membranes for fuel cells: the effects of micro-phase separation”. In: *Frontiers in materials* 7 (2020), p. 4.

[125] Qiucheng Xu et al. “Anion exchange membrane water electrolyzer: electrode design, lab-scaled testing system and performance evaluation”. In: *EnergyChem* 4.5 (2022), p. 100087.

[126] Qian Yang et al. “Poly (2, 6-dimethyl-1, 4-phenylene oxide)/ionic liquid functionalized graphene oxide anion exchange membranes for fuel cells”. In: *Journal of membrane science* 552 (2018), pp. 367–376.

[127] Bidattul Syirat Zainal et al. “Recent advancement and assessment of green hydrogen production technologies”. In: *Renewable and Sustainable Energy Reviews* 189 (2024), p. 113941.

[128] Shengchang Zhang et al. “Preparation of poly (vinyl alcohol)-grafted graphene oxide/poly (vinyl alcohol) nanocomposites via in-situ low-temperature emulsion polymerization and their thermal and mechanical characterization”. In: *Applied Surface Science* 396 (2017), pp. 1098–1107.

A

Supplementary Information on Theoretical Background

A.1. Water Electrolysis Technologies

Table A.1: Advantages and disadvantages of typical water electrolysis technologies [117, 61].

Technology	Advantages	Disadvantages
Alkaline WE	• Noble metal-free catalysts • Cost-effectiveness • Long-term stability	• Limited current densities • Gas crossover • Highly concentrated 5M KOH
AEMWE	• Noble metal-free catalysts • Low concentrated 1M KOH • High purity gases	• Limited alkaline stability • Limited OH^- conduction • Sub-optimal current densities
PEM WE	• Higher current densities • High purity gases • Compact system design • Quick response	• Cost of cell components • Noble metal catalysts • Fluorinated polymers

A.2. AEM

Anode	Cathode	Membrane	Electrolyte	Temp. (°C)	Current dens. (A cm^{-2} at V)
Fe-NiMo-NH_3/H_2	NiMo-NH_3/H_2	X37-50 Grade T	1 M KOH	80	1.0 (1.57)
IrO_2	Pt/C	PFTP-13	1 M KOH	80	7.68 (2)
IrO_2	Pt/C	Orion TM1	1 M KOH	30	2.75 (1.9)
CuCoO	NiCoO-NiCo/C	X37-50 Grade T	1 M KOH	50	0.504 (1.85)
IrO_2	Pt black	PiperION	1 M KOH	50	1.0 (1.9)
NiFeV LDH	Pt/C	X37-50 Grade T	1 M KOH	50	2.1 (1.8)
Ir black	Pt/C	AF1-HNN8-25	1 M KOH	60	2.0 (1.82)
$NiMn_2O_4$	Pt/C	FAA3-50	1 M KOH	80	0.53 (2)
NiFe	NiFeCo	X37-50 Grade T	1 M KOH	60	1.0 (1.9)
Acta 3030	Acta 4030	FAA-3	1 M KOH	60	0.4 (1.91)
IrO_2	Pt/C	A201	DI water	50	0.399 (1.8)
IrO_2	Pt/C	FAA-3-PK-75	0.5 M KOH	90	1 (1.8)
NiAl	NiAlMo	HMT-PMBI	1 M KOH	60	2.0 (2.086)
NiCu mixed oxide	Ir black	FAA-3-50	1 M KOH	50	1.85 (2)
Ni foam	$NiFe_2O_4$	Dowex Marathon A	10 wt% KOH	50	0.125 (1.85)
$NiCo_2O_4$	$Fe_{60}Co_{20}Si_{10}B_{10}$	PSEBS-CM-TMA	10 wt% KOH	50	0.36 (2)
$Cu_{0.81}Co_{2.19}O_4$	Co_3S_4	X37-50	1 M KOH	40	0.431 (2)
NiCoFeOx	Pt black	FAA-3-130	DI water	50	1 (2.492)
NiFe-LDH	Pt/C	X37-50 Grade T	1 M KOH	50	1 (1.69)
NiFe-LDH	Pt/C	X37-50 Grade T	1 M KOH	80	1 (1.59)
Cu_xCo_3-xO_4	Ni	FAA-3-50	1 M KOH	70	0.11 (2.2)
NiFe	PtRu/C	HTMA-DAPP	1 M NaOH	60	5.32 (1.8)
BSCF	Pt	A201	0.1 M KOH	50	0.2 (1.78)
$(NiCo)_3S_4$	Pt/C	X37-50	1 M KOH	60	1 (1.75)

Table A.2: Catalysts, membranes, and operation conditions of key AEMWE research [66].

B

Optimization of the Composite Membrane Casting Procedure

The fabrication procedure for composite membranes required optimization, as the process initially used for pristine polymer membranes could not be directly applied. A new approach was necessary to achieve stability and homogeneity of the membranes with graphene oxide (GO) as filler.

B.1. Initial Composite Membrane Casting

B.1.1. Qualitative GO-DMSO Stability Assessment

The first step was to assess the stability of the selected GO concentrations in DMSO (solvent dimethylsulfoxide). To qualitatively evaluate this, GO was dispersed in 1 mL of DMSO and sonicated for 3 hours. After sonication, the dispersion was inspected for visible homogeneity and left at room temperature overnight to check if it remained stable. Once the GO dispersion was confirmed to be homogeneous and stable overnight, three membranes were cast with GO filler loadings of 0.5%, 1%, and 2%.

B.1.2. Solution Preparation and Casting

For each membrane, a constant polymer mass of 0.7 g was used, dissolved in DMSO to form a 22% polymer solution. To achieve the GO loadings of 0.5%, 1%, and 2%, corresponding masses of 3.5 mg, 7 mg, and 14 mg of GO were added, respectively. These GO concentrations were selected based on literature, which commonly reports the use of GO in the range of 0.1% to 2% when analyzing its incorporation into polymer based anion exchange membranes [83, 19].

The sonication time of 3 hours for GO-DMSO dispersions was chosen based on established procedures in literature [71]. Directly adding GO to the 22% polymer solution was avoided due to a lack of evidence supporting its effectiveness in achieving a homogeneous mixture. Instead, separate solutions for the polymer in DMSO and GO in DMSO were prepared before mixing [112, 83, 75, 77, 71, 19].

The decision to use 1 mL of DMSO for the GO dispersion was a compromise between achieving a sufficiently low GO concentration in DMSO for better dispersion and preventing excessive viscosity in the initial polymer solution. A 22% polymer solution in DMSO with 0.7 g of polymer requires 2.48 g of DMSO, approximately 2.25 mL, given a density of 1.1 g/mL. After allocating 1 mL of DMSO for GO dispersion, which would be added to the solution after sonication, the remaining polymer solution had 1.25 mL of DMSO, resulting in an initial polymer concentration of 33.7%. Further reducing the amount of DMSO would have made the initial polymer solution too viscous for effective mixing. The use of 1 mL of DMSO proved effective, as the initial polymer-DMSO solution was already highly viscous, and any further reduction in solvent would have hindered magnetic stirring. Meanwhile, the GO-DMSO dispersion looked stable with 1 mL of DMSO.

After sonication, the GO-DMSO dispersion was added dropwise to the polymer-DMSO solution, followed by magnetic stirring for an additional 3 hours to ensure thorough mixing. Membranes were cast

following the procedure established for pristine membranes in earlier phases of the project. The membranes were cast onto stainless steel plates and placed in an oven at 80°C overnight. The next day, the membranes were transferred to a vacuum oven at 40°C and dried overnight.

B.1.3. Results and Defect Analysis

The resulting membranes displayed significant defects, as seen in figure B.2 and B.1. The cast membranes showed areas of extreme thinness and inhomogeneity, along with regions containing thick, dark, and fractured pieces. This indicated instability in the cast solution, particularly during the thermal treatment phase, where the membranes appeared to separate and crack.

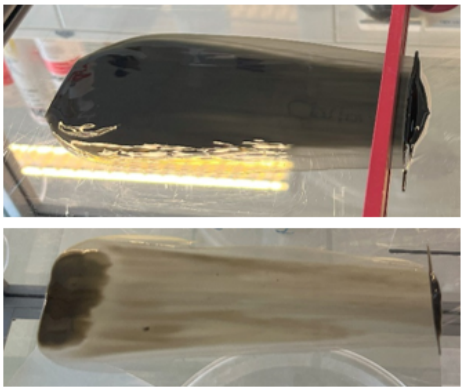

Figure B.1: First batch of membrane casting using Dr Blade (top: 2% GO, bottom: 1% GO).

Figure B.2: First batch of membrane casting after oven treatment (from left to right: 0.5%, 1%, and 2% GO).

SEM-EDS (Energy-Dispersive X-ray Spectroscopy) was conducted on the samples to investigate potential compositional differences across different areas of the membranes. Table B.1 summarizes the results of this analysis, which was performed on a pristine polymer membrane, a section of the GO 2% membrane (shown earlier), and a broken, dark piece from the same membrane.

A key observation from the EDS data is the elevated oxygen content in the broken dark piece compared to the intact area of the GO 2% membrane. The increased oxygen content in the GO 2% membrane relative to the pristine membrane is attributed to the oxygen-containing functional groups present in GO. The baseline oxygen detected in the pristine polymer membrane (2.90%) likely results from the instrument's sensitivity or from residual from polymer synthesis or solvent. In contrast, the GO 2% membrane shows a higher oxygen content at 3.40%, indicating the addition of GO while making the composite membrane. Notably, the broken piece of the GO 2% membrane exhibits an even higher

oxygen content at 5.29%, suggesting the accumulation of GO in these regions. Regarding sulfur, the content remains relatively consistent between the pristine membrane (0.16%) and the GO 2% membrane (0.15%). However, in the broken piece of the GO 2% membrane, the sulfur content increases significantly to 1.48%. These rises could indicate that during thermal treatment, GO and DMSO may have concentrated in specific areas, causing instability and phase separation, leading to the breaking of the membrane.

	Atom%		
Element	**Pristine**	**GO 2%**	**GO 2%: broken piece**
C	93.41 ± 0.40	93.64 ± 0.41	90.61 ± 0.46
O	2.90 ± 0.18	3.40 ± 0.20	5.29 ± 0.23
Al	1.32 ± 0.05	0.30 ± 0.03	0.33 ± 0.03
S	0.16 ± 0.02	0.15 ± 0.02	1.48 ± 0.05
I	2.21 ± 0.05	2.50 ± 0.05	2.29 ± 0.05

Table B.1: Atomic percentage of elements across the three samples.

B.2. Refining the Casting Procedure through System Evaluation

Given the results from the EDS analysis, further investigation into the interactions between the system's components was required, leading to adjustments to the membrane casting procedure. The key components under study are the polymer poly(co-aryl piperidinium), graphene oxide (GO), and the solvent DMSO. The process of preparing the final composite polymer solution involves two stages: the preparation of separate GO-DMSO and polymer-DMSO solutions, followed by their combination. Ensuring homogeneity in both individual solutions, as well as in the final mixture, is crucial. Therefore, it was essential to optimize the interactions between GO and DMSO, as well as between GO and the polymer, to improve dispersion and ensure the stability of the final membrane.

B.2.1. Solvent Selection

The solubility of the poly(co-aryl piperidinium) is best in solvents such as DMSO, DMF, NMP, and DMA, with DMSO being chosen for its lower toxicity and ease of processing [14].

However, while DMSO is an optimal solvent for the polymer, it is not ideal for dispersing GO. Studies suggest that solvents such as DMF, NMP, ethylene glycol, THF, and water are more effective for dispersing GO [27]. As shown in Figure B.3, the stability of GO dispersions in different solvents can be observed after 1 hour of sonication and again after 3 weeks [27].

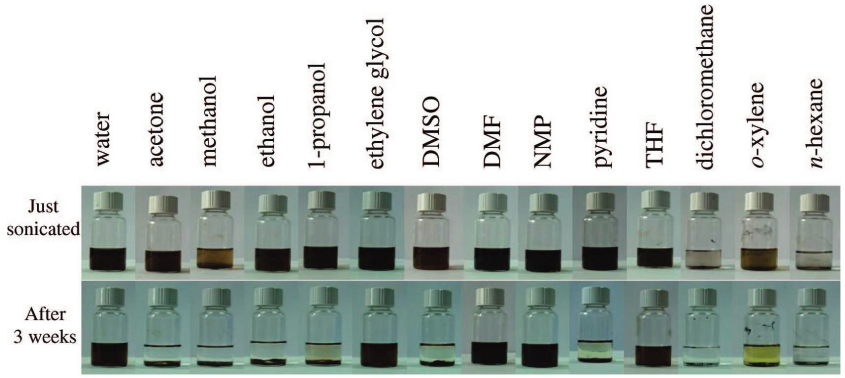

Figure B.3: GO dispersions with different solvents just sonicated and after 3 weeks [27].

Solvents that exhibit a high affinity for GO facilitate the solvation of GO sheets, overcoming inter-sheet attraction and forming stable dispersions. This affinity is influenced by physical properties such as dielectric constant, dipole moment, surface tension, and the Hildebrand solubility parameter [27]. Figure B.4 illustrates these parameters for various solvents, highlighting their differences and suitability for dispersing GO.

One of the most important parameters is the dielectric constant (ε_r), which reflects the solvent polarity and its ability to reduce the electrostatic forces between the charged particles. Generally speaking, with a higher dielectric constant than 30, better stabilization for GO dispersions could be provided as a result of the reduction of inter-sheet attractions [27]. Water, for instance, has a dielectric constant of around 80, hence making it a good solvent for GO, while DMSO with a relatively lower value of 46.7 is still able to give some stability to GO [24].

Another important factor is the dipole moment, which reflects the polarity of the solvent molecules themselves. The larger the dipole moment, the stronger the interactions with polar solutes, such as GO. Water has a dipole moment of 1.85 Debye, whereas DMSO has a higher value of 3.96 Debye [36].

Another critical factor is the surface tension and Hildebrand solubility parameters. When dispersing a 2D material like GO, the enthalpy of mixing per unit volume of solvent (ΔH_{mix}) is related to the difference in surface energies and solubility parameters among the materials involved [27]. The closer the Hildebrand parameter and surface tension of the solvent to those of GO, the less energy it takes to mix, making the solution more stable. GO has a surface tension of 62.1 mJ/m^2 and a Hildebrand parameter of 25.4 MPa$^{1/2}$. DMSO has a Hildebrand parameter (δ_T) of 26.7 MPa$^{1/2}$, closer to GO's, whereas water has a larger Hildebrand parameter of 47.9 MPa$^{1/2}$. While the surface tension of water, 72.8 mN/m, is closer to GO's, compared to that of DMSO with 43.54 mN/m [60].

Hydrogen bonding also plays an important role in the dispersion of GO. GO has hydroxyl, carboxyl, and epoxy functional groups that can participate in hydrogen bonding with solvents capable of providing suitable donors and acceptors. Water, in particular, would be an effective solvent, featuring strong donor capabilities with hydrogen bonding along with acceptors to provide extra stability for GO in dispersion [45]. DMSO is a strong hydrogen bond acceptor but a poor donor, and thus it is less effective than water in this respect [88].

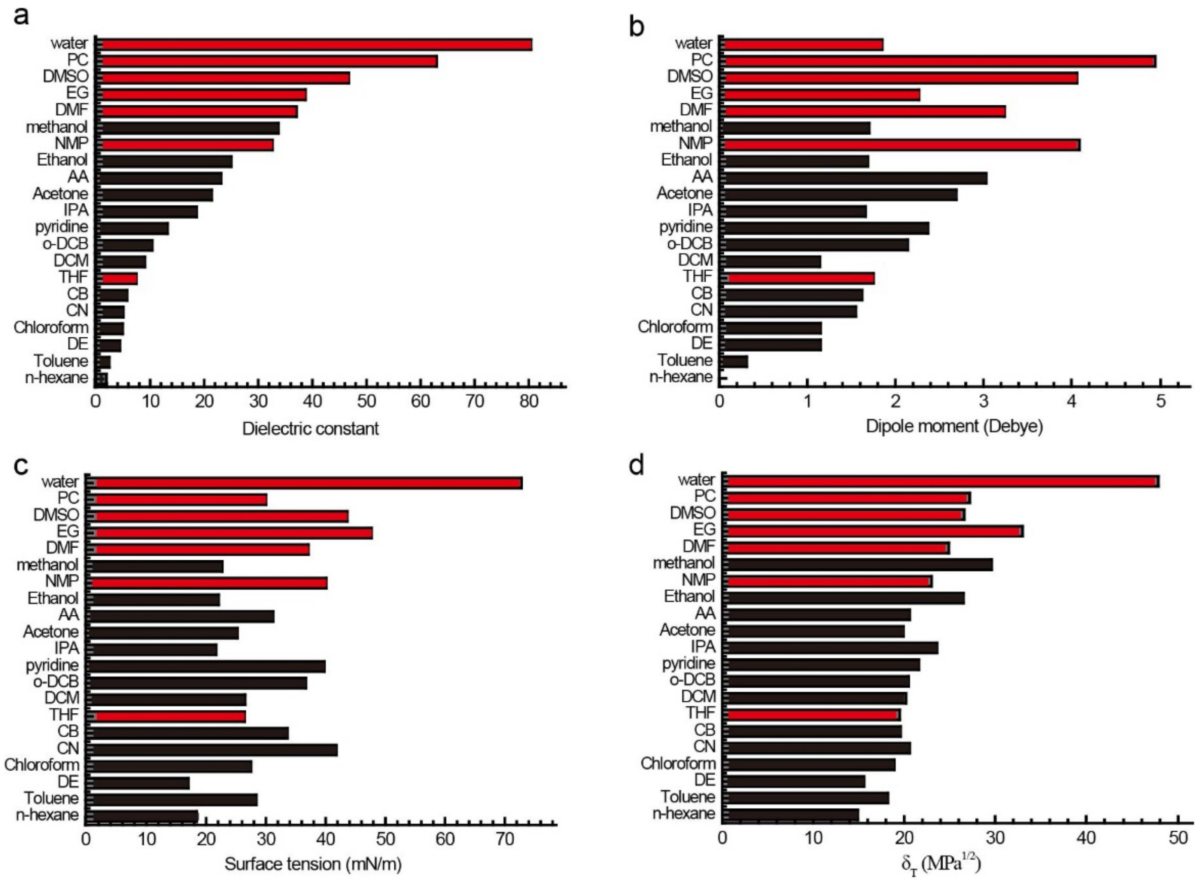

Figure B.4: (a) Dielectric constant, (b) dipole moment, (c) surface tension and (d) Hildebrand parameters (δT) of good (red) and poor solvents (black) for GO [27].

Despite DMSO not being the ideal solvent for GO, it was chosen due to its compatibility with poly(co-aryl piperidinium) and the specific requirements of the partner company regarding membrane casting process.

B.2.2. Interactions in the System

The structure of poly(co-aryl piperidinium) consists of a hydrophobic, non-polar aromatic backbone, with hydrophilic, polar regions formed by piperidinium groups that promote water transport. This polymer can engage in $\pi - \pi$ interactions between aromatic rings and electrostatic interactions, such as ion-dipole, with other components.

Graphene oxide (GO) consists of one or more layers of aromatic graphene sheets functionalized with oxygen-containing groups, including hydroxyl, carboxyl, and epoxy groups, predominantly located at the edges of the sheets. GO possesses hydrophobic, non-polar sections (aromatic sheets) as well as hydrophilic, polar regions (oxygenated functional groups). It can form dipole interactions via its hydroxyl, carboxyl, and epoxy groups, and act as both a hydrogen bond donor and acceptor. Furthermore, GO can participate in $\pi - \pi$ interactions with the aromatic structure of poly(co-aryl piperidinium), as well as cation$-\pi$ interactions with the piperidinium group. The GO sheets typically aggregate due to strong van der Waals and $\pi - \pi$ stacking between their aromatic domains. These forces result in attraction between the GO sheets, complicating the achievement of stable dispersions. To overcome these attractive forces, an efficient solvent system is necessary to provide steric or electrostatic stability [100].

DMSO, a polar aprotic solvent known for its hygroscopic nature, can participate in dipole interactions and acts as a hydrogen bond acceptor [88].

However, DMSO is not the most effective solvent for dispersing GO due to a suboptimal balance across key dispersion parameters, as well as its limited hydrogen bonding capacity, as previously seen. Furthermore, the interaction between poly(co-aryl piperidinium) and GO is restricted, as it primarily relies on weaker $\pi - \pi$ interactions, with the polymer lacking functional groups for more robust hydrogen bonding. Hydrogen bonds typically range from 2 to 10 kcal/mol, depending on the system, while $\pi - \pi$ interactions between two atoms generally exhibit lower strengths, usually below 5 kcal/mol, similar to van der Waals forces. However, the strength of $\pi - \pi$ stacking can increase significantly in larger aromatic systems, sometimes reaching up to 20 kcal/mol [25, 109]. But $\pi - \pi$ interactions generally remain weaker than hydrogen bonding. In fact, many composite membranes reported in the literature for water electrolysis that use GO as a filler rely on polymer matrices with oxygen atoms in their backbone, which facilitate hydrogen bonding, enhancing compatibility and dispersion with GO [112, 83, 75, 77, 71, 19].

B.2.3. Ethanol as Co-Solvent and Decreased Oven Temperature

Given the suboptimal dispersion of GO in DMSO and the weak interaction between GO and the polymer, a small percentage of a co-solvent was introduced to improve dispersion. Ethanol was selected as the co-solvent, as it had previously been used in the company's polymer processing without issues. Ethanol acts as both a hydrogen bond donor and acceptor, facilitating better dispersion of GO in DMSO. Additionally, it reduces the viscosity of the overall solution (GO-DMSO-polymer), improving homogeneity during mixing and helping in preventing GO particle agglomeration.

In addition to this, the oven temperature of 80°C for the thermal treatment of the membrane after casting, was lowered to 50°C, to allow for a gentler thermal treatment and help avoiding phase separation between the polymer and GO.

Dynamic Light Scattering Evaluation

To confirm whether adding ethanol as a co-solvent would indeed facilitate a homogeneous dispersion, dynamic light scattering (DLS) measurements were conducted using the Malvern Zetasizer Nano series. DLS was used to assess the dispersion quality of GO in the DMSO and ethanol-DMSO mixtures by measuring particle size in solution. DLS is a commonly employed technique for determining particle size. It uses light intensity fluctuations to assess the Brownian motion of particles in a fluid and then applies the Stokes-Einstein equation to determine the relationship between the diffusion coefficient and the hydrodynamic diameter of particles [76]. The technique presupposes that the particles are spherical, which poses limitations when addressing non-spherical and polydisperse particles like GO. However, the use of DLS to approximately measure the size of GO has been reported as a simple and fast method

of characterization, yielding valuable estimations regarding its dispersion and agglomeration [4].

In this case, DLS was used to compare the particle sizes of GO dispersed in pure DMSO with those dispersed in a mixture of DMSO and ethanol. A reduction in particle size would indicate a more stable dispersion with less agglomeration. Indeed, as can be seen from the results, the particle size was much finer for GO particles prepared using ethanol as a co-solvent, which suggested better dispersibility.

Table B.2 summarizes the results of DLS analysis on dispersions of GO 0.5%, GO 1%, and GO 2%, which would eventually be used in a 0.7 g polymer DMSO solution at 22%, corresponding to masses of 3.5 mg, 7.07 mg, and 14.29 mg of GO in 1 mL DMSO. Figure B.5 shows the three tested GO wt% dispersions after 3 hours of sonication, before DLS measurements, where differences in color and aggregation are already noticeable. The data show that with increasing GO wt% in DMSO, the particle size increases, which in any case is relatively high, with values in the range of 2 to 3 µm. Additionally, the polydispersity (PDI) of the solutions is high, increasing with GO concentration, which indicates a broad particle size distribution and potential aggregation. These very high PDI values could also result from using DLS to analyze non-spherical GO particles.

	Mean and Standard Deviation		
Parameter	**GO 0.5%**	**GO 1%**	**GO 2%**
Diameter (nm)	2300.937 ± 132.928	2344.812 ± 294.605	3156.727 ± 480.596
PDI	0.316 ± 0.07	0.495 ± 0.44	1 ± 0.0

Table B.2: Intensity-weighted average hydrodynamic diameter and PDI for GO 0.5%, GO 1%, GO 2% in 1 mL DMSO.

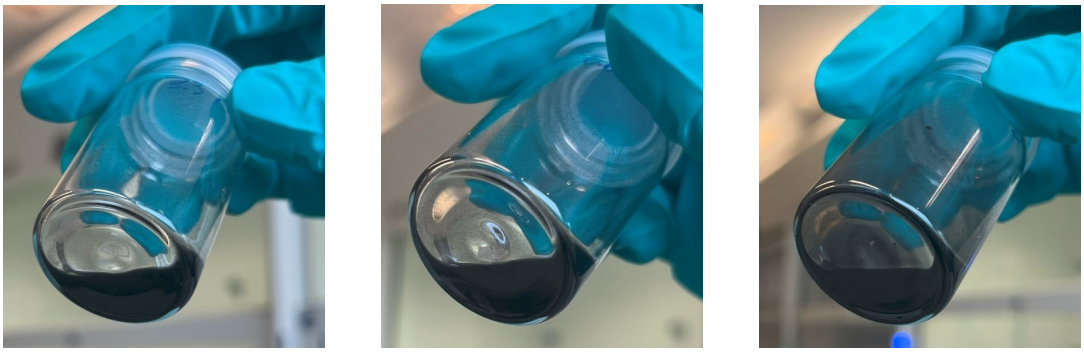

Figure B.5: 0.5%, 1%, 2% GO dispersions in DMSO.

Following, similar testing was conducted on 2 mg of GO dispersed in 1 mL solutions of DMSO with varying ethanol concentrations (2%, 5%, 10%, and 20%), after 2 and 3 hours of sonication. The results from this analysis are reported in Table B.3. The purpose of this experiment was to compare the particle size of GO in ethanol-DMSO solutions with that in pure DMSO, identify a suitable ethanol concentration, and assess whether the commonly used 3-hour sonication time reported in literature was necessary.

	2 hour sonication		**3 hours sonication**	
DMSO-EtOH wt%	**Diameter (nm)**	**PDI**	**Diameter (nm)**	**PDI**
2	298.1 ± 9.065	1 ± 0	550.8 ± 478.8	0.7608 ± 0.4143
5	439.6 ± 217.6	0.3819 ± 0.5393	276.2 ± 3.901	1 ± 0
10	536.7 ± 166.8	0.8753 ± 0.216	520.722± 32.158	0.438 ± 0.01
20	184.5 ± 8.337	0.1815 ± 0.1103	181.3 ± 1.394	0.2613 ± 0.02179

Table B.3: Intensity-weighted average hydrodynamic diameter and PDI for GO dispersions in DMSO with varying ethanol concentrations, measured after 2 hour and 3 hours of sonication.

The mean hydrodynamic diameters across the four ethanol concentrations are approximately 364 nm after 2 hours of sonication and 382 nm after 3 hours of sonication. The data suggests only marginal variation in particle size with extended sonication, indicating that increasing the sonication time provides no

significant benefit. In fact, unnecessarily prolonging sonication may lead to unwanted effects, as after a certain point, further sonication may fail to break particles apart and instead promote re-agglomeration. This could occur due to localized heating and increased particle collisions. Therefore, it was concluded that 2 hours of sonication is sufficient to achieve a stable dispersion, making the membrane casting process more efficient.
Additionally, during these experiments, it was concluded that it was necessary to change the sonication bath every 30 minutes, as the temperature would rise excessively and the solutions showed signs of agglomeration. This could lead to the evaporation of ethanol (boiling point of 78.37°C at standard atmospheric pressure), reducing its stabilizing effect on the solution, or promote particle agglomeration due to increased Brownian motion. Therefore, the bath was changed every 30 minutes to ensure the temperature remained below 40°C. This strategy proved effective.

The selected ethanol concentration was 10 wt%, resulting in a solution composed of 0.9 mL DMSO and 100 µL ethanol. This percentage was also previously used as co-solvent with a reinforced poly(co-aryl piperidinium) in another study [119]. Figure B.6 shows the DMSO-ethanol 10% solution with 2 mg of GO. This concentration was chosen because it exhibited a relatively stable particle size across different sonication times (536.7 nm after 2 hours, 520.7 nm after 3 hours), providing a more consistent and controlled procedure. Although the particle size at 2 hours was the highest among the ethanol concentrations tested, no clear correlation between ethanol concentration and particle size in solution was observed. Additionally, higher ethanol concentrations were avoided because of the polymer not being soluble in ethanol.

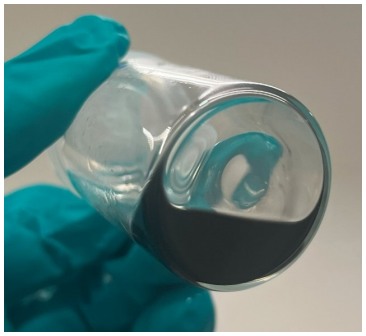

Figure B.6: DMSO-ethanol 10% dispersion of 2 mg of GO.

It should be noted that the GO particle size measured by DLS was within the expected range based on the material's characteristics. The GO used, consisting of fifteen to twenty-layer flakes, has an estimated thickness value of 15 nm. In fact, functional groups and interlayer spacing make the GO layers reach a thickness of about 0.8 nm, more than the theoretical thickness a single layer of graphene (around 0.34 nm) [62]. As a 2D material, GO's lateral size is also of interest. Commercially available GO is generally around 2 µm in lateral size [12]. However, the sonication process reduces both the sheet and lateral size of GO. Indeed, it has been reported that after 120 minutes of ultrasonication, size is reduced to 54.55% in an ultrasonic bath, and to 86.36% in a probe sonicator [63]. By these considerations, the DLS measurements for the hydrodynamic diameter of the GO particles are consistent with expectations.

B.2.4. Updated Casting Procedure

Recycled Polymer

Due to a shortage of polymer in the first phase of the project and the failure of the initial casting attempt, the subsequent attempt was made using recycled polymer. This involved taking pristine membranes cast in earlier phases of the project and re-dissolving them in DMSO, rather than using fresh polymer powder. A total of 0.7 g of dry pristine polymer membranes was dissolved in the right amount of DMSO to create a final 22% polymer solution. While 0.9 mL of DMSO was reserved for sonication with GO, along with 100 µL of ethanol. The sonication time was kept at 2 hours and the oven temperature at 50°C. The cast membrane with GO 0.5% using this procedure is shown in Figure B.7, and the attempt proved successful.

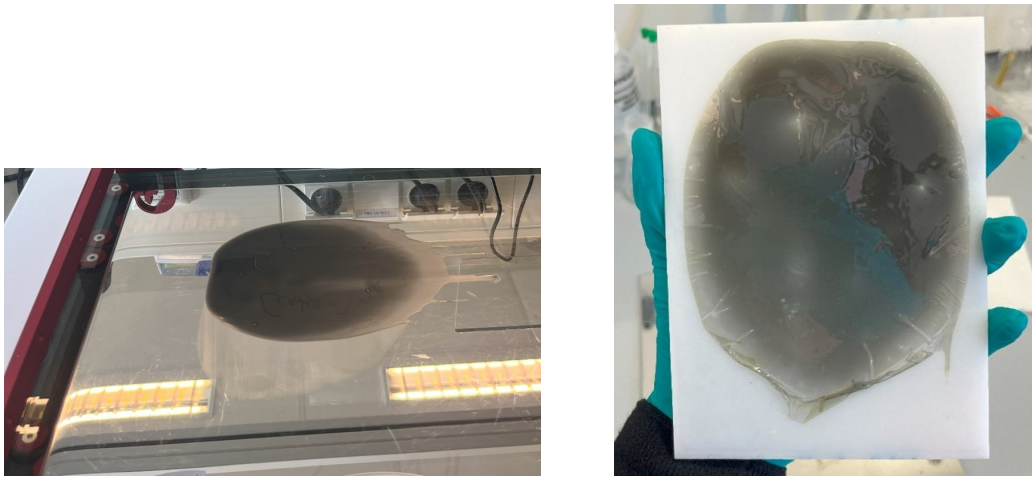

Figure B.7: Cast membrane (left) and dry membrane (right), produced with recycled polymer and GO 0.5% with DMSO-ethanol 10% dispersion.

This procedure demonstrated that the introduction of GO into this type of polymer membrane was indeed possible, and revealed the successful reutilization of pristine membranes. In a world where waste reduction becomes ever more important, such recyclability is a definite advantage. For example, one highly useful point would be a comparison of properties of membranes manufactured from recycled polymer against those prepared using fresh polymer powder, as this could offer insights into both performance and sustainability.

Fresh Polymer Powder

The same successful procedure was then applied to fresh polymer powder for three membranes with GO concentrations of 0.5%, 0.25%, and 0.125%. The GO concentrations were reduced to promote better dispersion and avoid agglomeration, given the weaker interactions at play. However, the attempt was again unsuccessful. Figure B.8 shows the resulting membranes after drying.

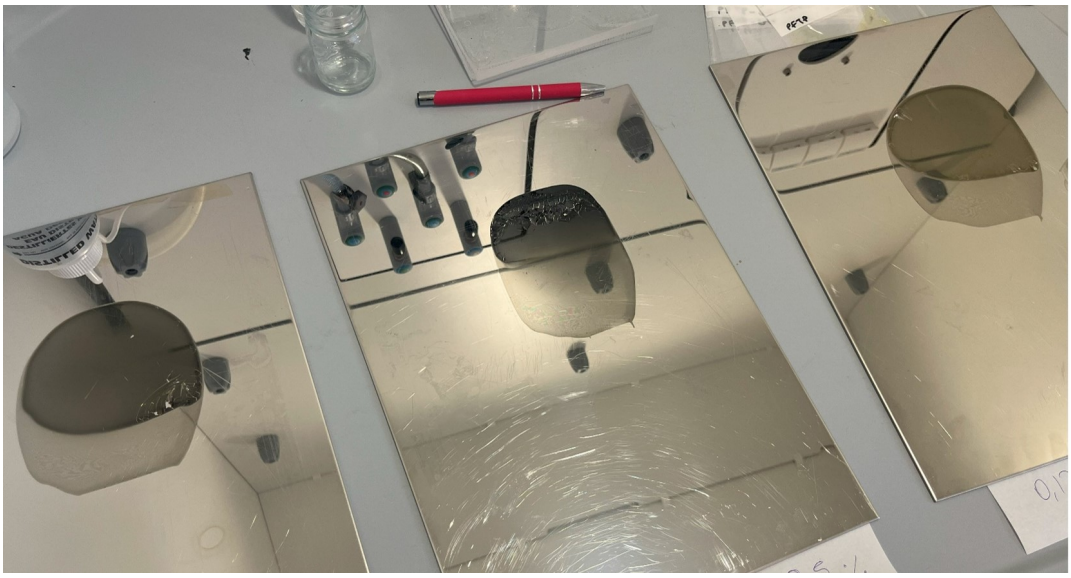

Figure B.8: Dry membranes with GO 0.25% (left), GO 0.5% (center), and GO 0.125% (right) in DMSO-ethanol 10% dispersion.

The membranes produced in this attempt with the modified procedure appeared better than the first attempt using only DMSO, but they still broke when being removed from the stainless steel plate, resulting in broken, darker pieces. In contrast, the same procedure proved effective with the recycled

membranes, even after multiple tries.
Therefore the next step was to identify the variable in the recycled membranes that made this possible. The key differences identified were: (1) the potential use of a different polymer batch in casting the older membranes, possibly having a different molecular weight and thus a different polymer chain length; (2) a lower actual polymer percentage in the casting solution, as the weight of the recycled membranes likely included some residual DMSO that had not fully evaporated in the oven; and (3) the fact that the recycled membranes had been stored for several months, allowing them to absorb moisture from the environment, introducing a non-negligible percentage of water that may have aided dispersing GO.

B.2.5. Water as Co-Solvent

Option 3 was explored. Initially, water was dismissed as a potential co-solvent for the GO-DMSO dispersion due to the polymer's insolubility in water, similar to ethanol. However, ethanol had previously been used in polymer processing without any issues [119]. Ethanol was favored over water because of its lower polarity and dielectric constant (24.3 for ethanol versus 80 for water [27]), which reduces the likelihood of disrupting the hydrophobic backbone of the polymer. Additionally, ethanol's lower Hildebrand solubility parameter compared to water enhances its compatibility with the polymer during membrane casting, allowing for better interaction between the polymer and GO.
On the other hand, water is a superior solvent for GO due to its stronger hydrogen bonding capacity and better balance of solubility properties, as discussed previously. These properties enable water to interact more effectively with the oxygen-containing functional groups of GO. Despite this advantage, water's high polarity could potentially interfere with the polymer matrix, making it less suitable in this case.
Inspired by the success of the recycled polymer membranes, a small quantity of water was added in a subsequent experiment. Furthermore, the use of mixed solvents, particularly water and DMSO, has been explored in literature for stabilizing GO dispersions [2, 13]. Research has demonstrated that adding small amounts of water to solvents where GO typically exhibits poor dispersibility significantly improves its colloidal stability [3]. The aim was to enhance the dispersion of GO in DMSO without compromising the solubility of the polymer. This adjustment sought to balance the strengths of water in stabilizing GO with its potential impact on the polymer's integrity.

Dynamic Light Scattering Evaluation

Similar to the experiments with ethanol, tests were conducted using 2 mg of GO dispersed in 1 mL DMSO solutions with varying water concentrations (1%, 2%, 5%, 10%) after 2 and 3 hours of sonication. The results from this analysis are summarized in Table B.4.

	3-hour sonication		2-hour sonication	
DMSO-H_2O wt%	**Diameter (nm)**	**PDI**	**Diameter (nm)**	**PDI**
1	349.4 ± 117.4	0.3892 ± 0.2416	322.6 ± 4.121	1 ± 0
2	246.6 ± 46.84	0.6864 ± 0.5432	677.8 ± 24.98	1 ± 0
5	307.2 ± 8.687	1 ± 0	298.2 ± 1.568	1 ± 0
10	426.8 ± 134.3	0.6994 ± 0.5206	347.1 ± 8.546	1 ± 0

Table B.4: Intensity-weighted average hydrodynamic diameter and PDI for GO dispersions in DMSO-H_2O with varying water concentrations, measured after 3-hour and 2-hour sonication.

The mean hydrodynamic diameters for the GO dispersions after 2-hour and 3-hour sonication were 332.5 nm and 411.425 nm, respectively. Although the PDI values in the measurements were broad, the 5% water dispersion exhibited the most consistent particle size and, on average, the smallest value. Therefore, 5% water was chosen as the optimal concentration. In the previous case, 10% ethanol was selected; however, water is potentially more challenging for the polymer system. Thus, selecting a lower concentration of 5% water balanced dispersion while minimizing its impact on the polymer.

Results

This decision resulted in a solution composed of 0.95 mL DMSO and 50 µL water with the required amount of GO for the final concentration. Figure B.9 shows the resulting membrane made with 0.25% GO in a DMSO-H_2O 5% solution and always 22% of powder polymer content. As can be seen, the

improvement is significant and the procedure proved successful in producing a good membrane. The membrane's shape is similar to the pristine cast membranes, with an oval shape and a very thin outer part. The coffee-ring effect on the membrane with the GO filler is clearly visible.

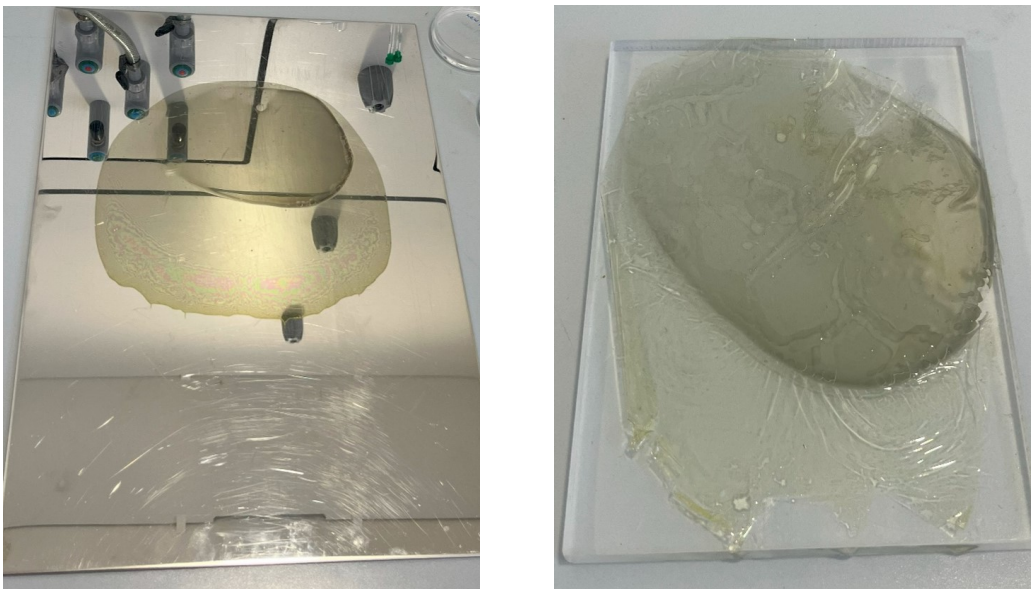

Figure B.9: (Left) Dried membrane with GO 0.25% in DMSO-H_2O 5% solution. (Right) Membrane separated from the stainless steel plate.

The phenomenon that occurs when a liquid containing suspended particles evaporates off a surface is known as the coffee-ring effect [23]. As the solvent evaporates, the droplet's contact line remains pinned due to surface heterogeneity, and contact angle hysteresis prevents the droplet from contracting. This establishes a flow from the droplet's center to its perimeter to replace the lost liquid, with the flow along the perimeter faster than in the core. This transports the suspended particles outward and deposits them at the perimeter in a ring-like configuration, similar to the pattern observed in a dried coffee droplet. In the membrane seen in the figure B.9, GO particles have migrated to the borders, resulting in a larger concentration of particles at the perimeter and consequently not homogeneously filled cast membranes.
Besides, the uneven height of the 400 µm Dr Blade contributes to inhomogeneity in GO concentration and thickness within the membrane. To address this, the membrane samples for testing were cut from areas that appeared more uniform and not too close to the edges to avoid brittle regions. Consequently, the actual concentration of cut membrane sections may not align precisely with the anticipated concentration of the prepared solution.

To conclude, a series of dispersions with varying sonication times, solvent concentrations, and drying temperatures were tested to identify optimal conditions for producing a homogeneous GO-polymer membrane. The final successful procedure was as follows: 2 hours of GO-DMSO-water 5% sonication, followed by gradual drop-by-drop addition to a polymer-DMSO mixed solution, then a 3-hour mixing period, casting, and drying at 50°C in an oven overnight, followed by 40°C in a vacuum oven overnight. This procedure will be used throughout the project and is detailed in the main text under Experimental Methodology 4.1.

C

Polymer Batches

C.1. Intrinsic viscosity

The polymer powder used for membrane casting was obtained in two distinct batches, Batch 1 and Batch 2. After drying both batches in an oven to remove residual moisture and solvent, solutions were prepared by dissolving the polymer in DMSO at identical concentrations. Initial observations revealed noticeable differences in viscosity between the two batches, indicating potential variations in polymer characteristics, specifically molecular weight. After conducting H-NMR and FT-IR analyses on both polymer batches, differences in chemical structure were excluded [20, 44]. Since polymers with higher molecular weight tend to exhibit superior film-forming properties, while those with lower molecular weight often result in limited film formation, any variations in molecular weight between batches could introduce variability into the experiments [14]. Therefore, it was necessary to characterize these differences before proceeding with membrane testing at various GO concentrations.

Typically, polymer molecular weight is determined through techniques such as gel permeation chromatography (GPC), which allows for precise analysis of polymer chain lengths by comparison to calibration standards [113]. However, due to the complex structure of the polymer, being a block copolymer and carrying a charge, GPC yielded inconsistent results in previous parts of the project [29].

To address these challenges, intrinsic viscosity was selected as an alternative indicator of molecular weight [122, 90]. Widely cited in the literature, intrinsic viscosity measurements correlate with the viscosity-average molar mass M_v via the Mark-Houwink-Sakurada equation [105]:

$$[\eta] = KM_v^a$$

where K and a are empirical Mark-Houwink parameters that depend on the polymer-solvent system and temperature. Given that this polymer is newly developed, established values for K and a were unavailable, precluding the calculation of an absolute M_v. Instead, intrinsic viscosity values were used to qualitatively compare molecular weights between batches, as higher intrinsic viscosity generally correlates with larger molecular weight and polymer chain length.

To determine intrinsic viscosity, measurements were conducted in the dilute concentration regime, where polymer chains are sufficiently spaced to minimize intermolecular interactions. In this regime, polymer coils move independently, avoiding entanglements or overlapping that could impact viscosity measurements [92]. Following the Huggins equation [92]:

$$\frac{\eta_{sp}}{c} = [\eta] + k_H[\eta]^2 c$$

where $\eta_{sp} = \frac{\eta - \eta_0}{\eta_0}$ is the specific viscosity, c is the polymer concentration in g/dL, and k_H is the Huggins constant. At low concentrations, the $k_H[\eta]^2 c$ term becomes negligible, simplifying the relationship between viscosity and concentration. Thus, we can express this as:

$$\lim_{c \to 0} \frac{\eta_{sp}}{c} = [\eta]$$

indicating that, as the concentration c approaches zero, the reduced viscosity $\frac{\eta_{sp}}{c}$ converges to the intrinsic viscosity $[\eta]$, a measure that reflects the polymer's contribution to the solution viscosity in the absence of chain interactions.

Using the definition of specific viscosity, we can rewrite this in terms of the ratio of the polymer solution viscosity η to the solvent viscosity η_0:

$$\frac{\eta}{\eta_0} = 1 + [\eta] \cdot c$$

Using the rheometer, the ratio $\frac{\eta}{\eta_0}$ of the polymer solution viscosity η to the solvent viscosity η_0 was measured across decreasing polymer concentrations. By plotting this ratio against concentration c, the slope of the linear fit in the dilute concentration range provides the intrinsic viscosity $[\eta]$.

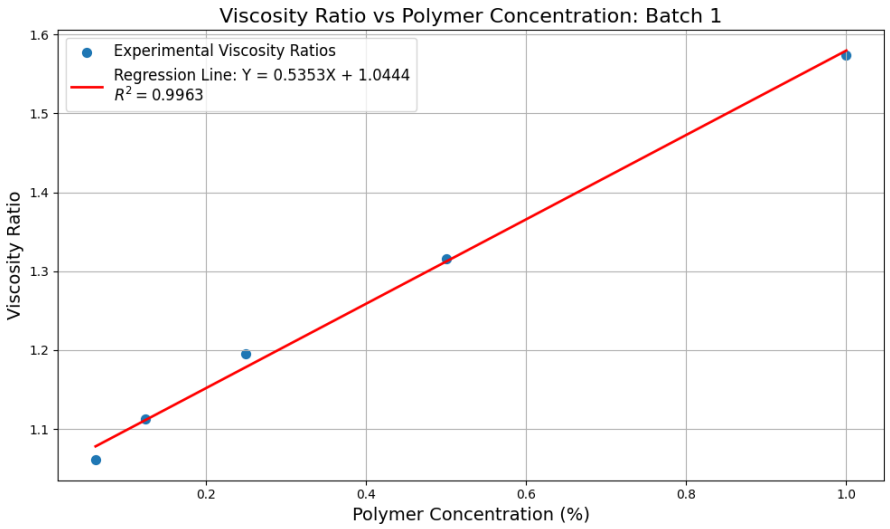

Figure C.1: Viscosity Ratio for polymer Batch 1.

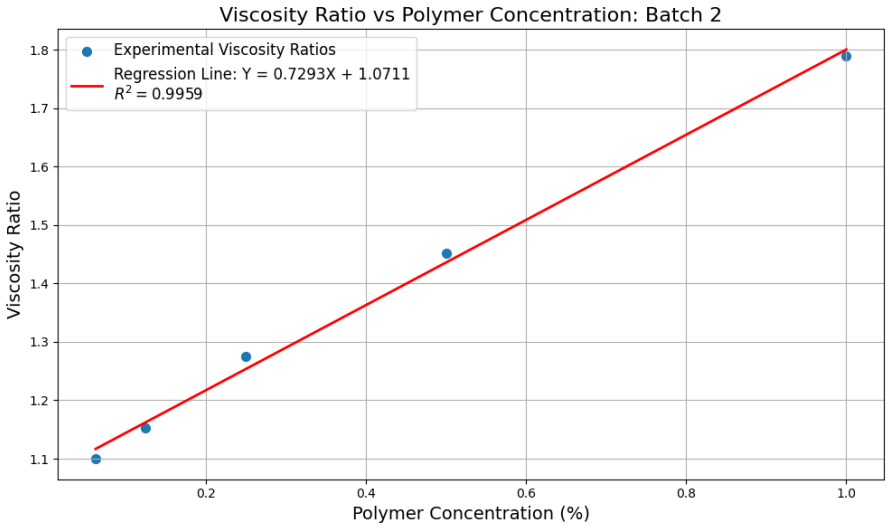

Figure C.2: Viscosity Ratio for polymer Batch 2.

From Figures C.1 and C.2, the intrinsic viscosities of the two polymer batches were extrapolated: 0.7 dl/g for Batch 2 and 0.5 dl/g for Batch 1, with Batch 2 showing a 40% higher intrinsic viscosity compared to Batch 1. This observation aligns with the viscosity differences noted during solution preparation for membrane casting: at the same polymer concentration, the solution prepared with Batch 2 appeared more viscous than that with Batch 1.

According to the Mark-Houwink theory, a higher intrinsic viscosity suggests a higher molecular weight, indicating that the polymer chains in Batch 2 may be longer than those in Batch 1. This difference impacts overall membrane casting, influencing how the polymer interacts with GO and ultimately affecting the results of subsequent tests [14].

C.2. TGA

Thermogravimetric analysis (TGA) provides additional insights into the thermal stability of the two polymer batches. Figures C.3 and C.4 show the weight loss and derivative weight loss (DTG) curves as a function of temperature for Batch 1 and Batch 2.

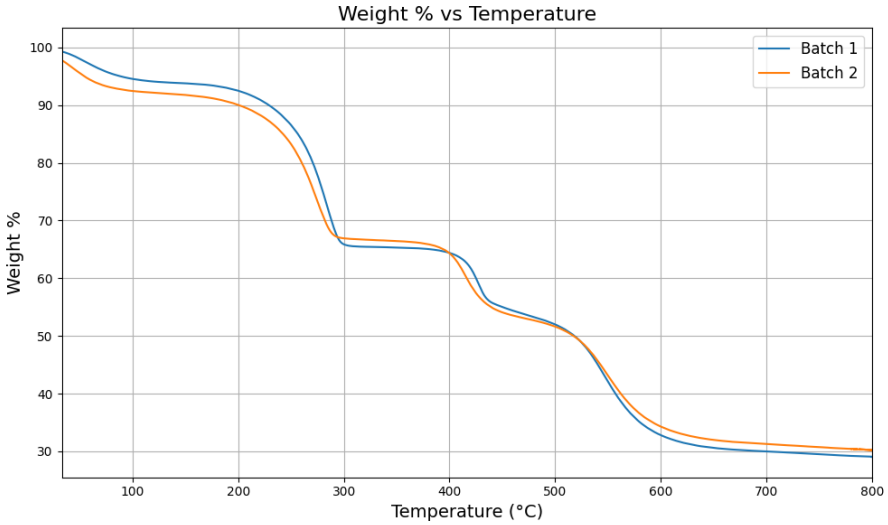

Figure C.3: TGA weigth % curves for different polymer batches.

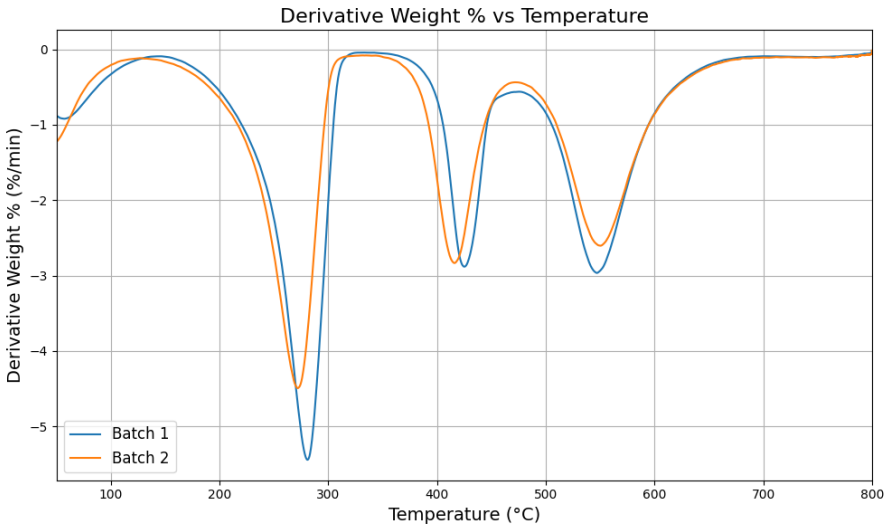

Figure C.4: TGA derivative weigth % curves for different polymer batches.

In the TGA weight loss curve, both batches exhibit very similar thermal stability trends. Batch 2 shows a larger weight loss at lower temperatures, which is attributed to moisture content. This trend is also observed in the DTG curve, where the degradation peaks for both batches occur at comparable temperatures, indicating that the thermal degradation behavior of both batches is largely similar. The polymer doesn't present melting during analysis, suggesting a very amorphous structure. A more detailed analysis of TGA curves is performed on polymer and polymer-GO membranes in the main text 5.5.

C.3. DSC

Differential Scanning Calorimetry (DSC) was performed on the samples to investigate the hypothesis suggested by intrinsic viscosity results. Molecular weight influences the glass transition temperature (T_g) of polymers, which reflects the transition of the amorphous regions from a rigid, glassy state to a flexible, rubbery state [30]. Higher molecular weight polymers typically have increased T_g due to greater chain entanglement, which restricts molecular mobility [123]. Additionally, lower molecular weight polymers, with more chain ends, have increased free volume, allowing chain segments in the amorphous regions to move more freely and transition to a flexible state at lower temperatures, thus reducing T_g [22].

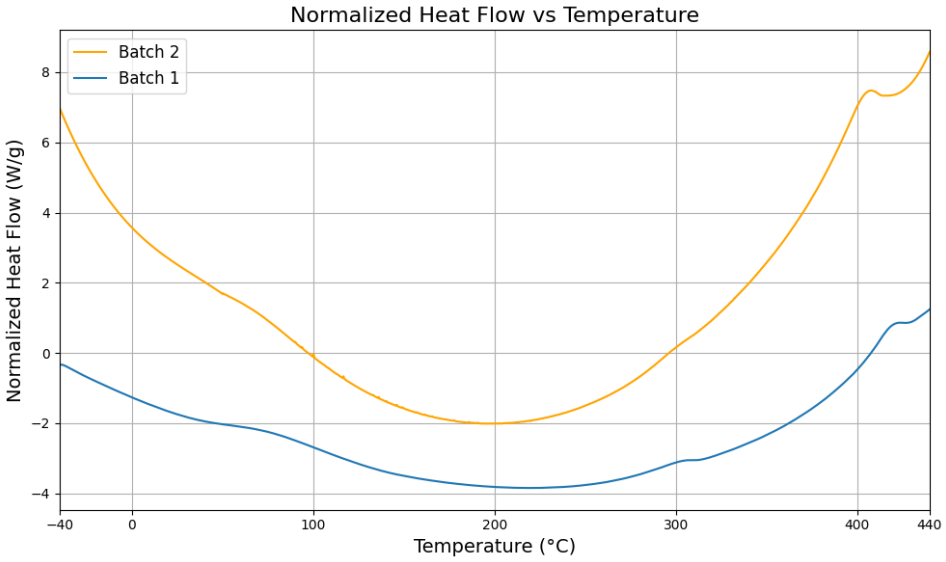

Figure C.5: DSC normalized heat flow for different polymer batches.

Figure C.5 shows the normalized heat flow curves of Batch 1 and Batch 2. The curves exhibit similar trends, with three small exothermic peaks: one before 110°C, one around 300°C, and one after 400°C. The latter two are likely due to rearrangements in the crystalline structure, while the first was further analyzed as the probable T_g. Figure C.6 presents a close-up of the curves around the possible T_g; the peaks are indeed minimally prominent and close in temperature. However, when taking the midpoint of both ranges, Batch 1 appears to peak at 60°C, while Batch 2 peaks later at 80°C, consistent with a higher molecular weight.

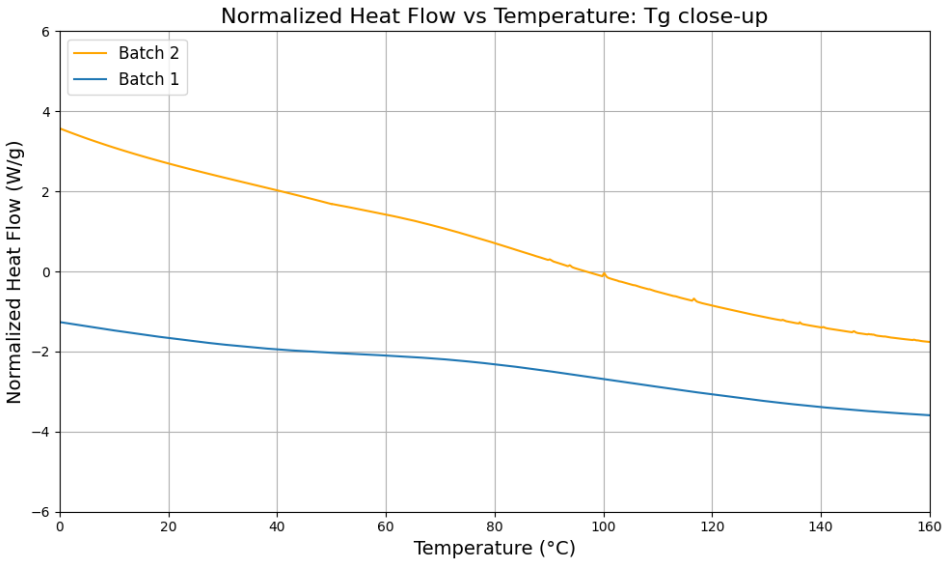

Figure C.6: DSC normalized heat flow for different polymer batches: Tg close-up.

D

Extra Results

D.1. Conductivity

Figure 5.2 in the main text presents the conductivity trend for batch 2, while figure D.1 displays the results for batch 1, where one set of six membranes was analyzed. The trend appears overall similar, with the pristine membrane starting at 27 mS/cm and reaching a peak value of 65 mS/cm at GO 0.5%. The conductivity increments between the different GO concentrations are more pronounced, and the conductivity at GO 1% is notably lower than that of batch 2.

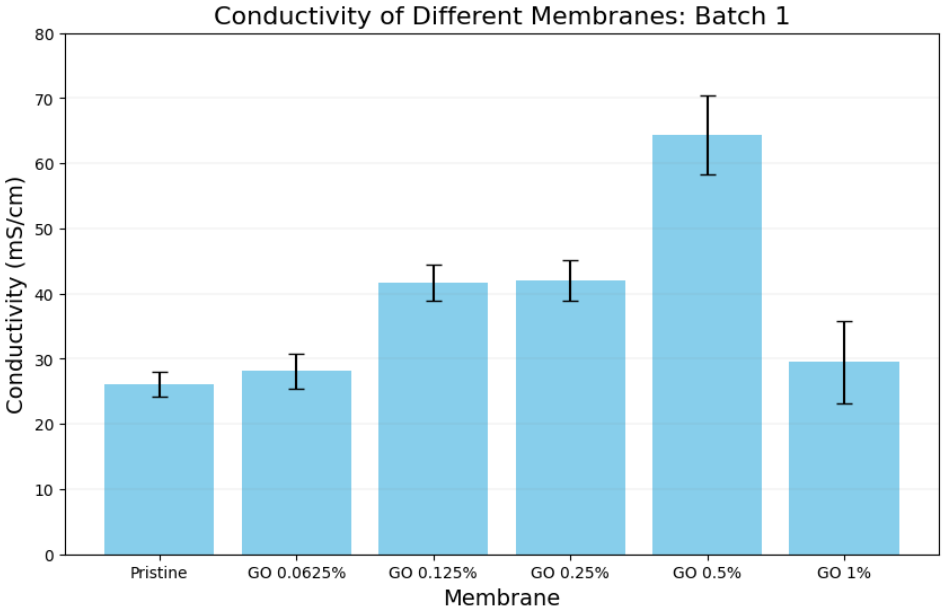

Figure D.1: Conductivity of membranes: Batch 1.

D.2. Electrolyser

D.2.1. Batch 2-a

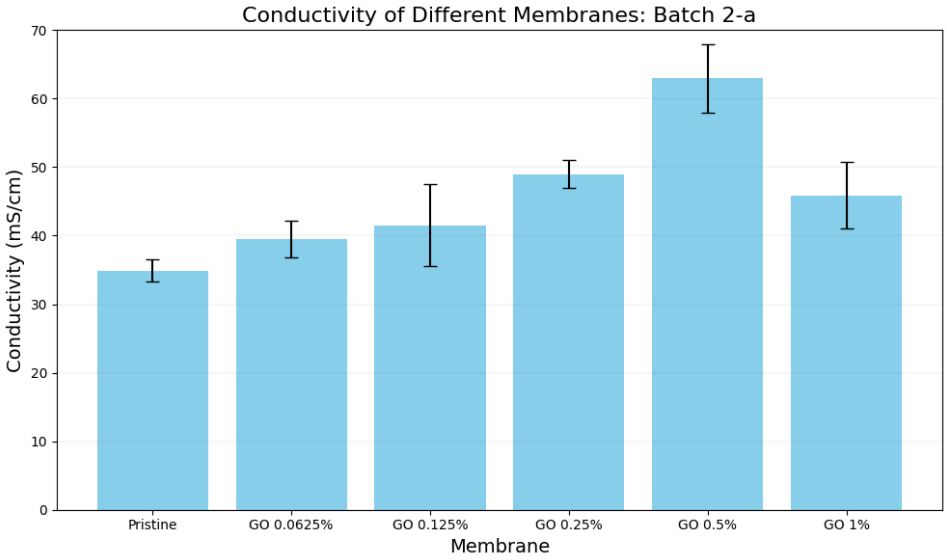

Figure D.2: Conductivity of membranes: Batch 2-a.

Table D.1: Membrane Thicknesses for Batch 2-a

Membrane	Wet Thickness (µm)
Pristine	52
GO 0.0625%	48
GO 0.125%	40
GO 0.25%	48
GO 0.5%	58
GO 1%	63

D.2.2. Batch 2-b

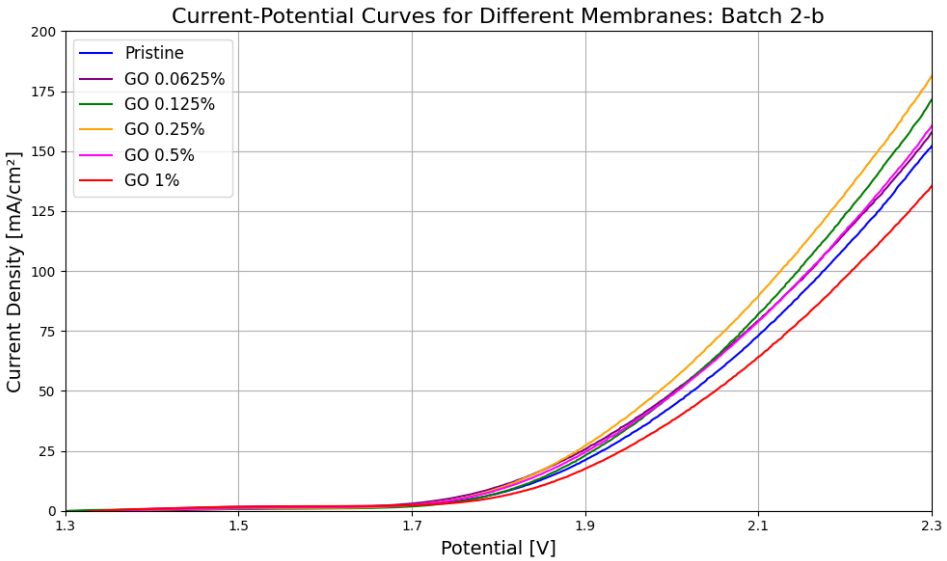

Figure D.3: Current-Potential Curves of membranes: Batch 2-b.

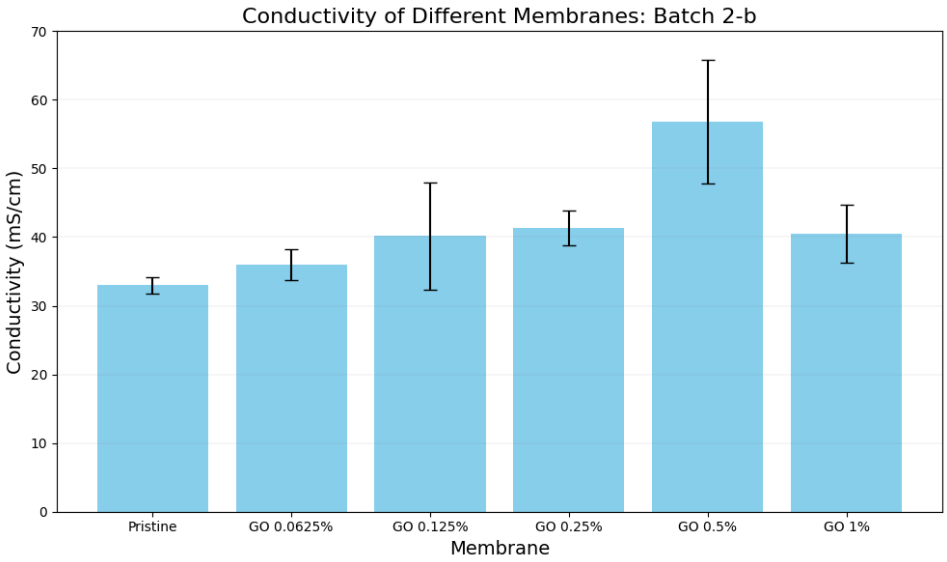

Figure D.4: Conductivity of membranes: Batch 2-b.

Table D.2: Membrane Thicknesses for Batch 2-b

Membrane	Wet Thickness (µm)
Pristine	39
GO 0.0625%	40
GO 0.125%	33
GO 0.25%	32
GO 0.5%	59
GO 1%	56

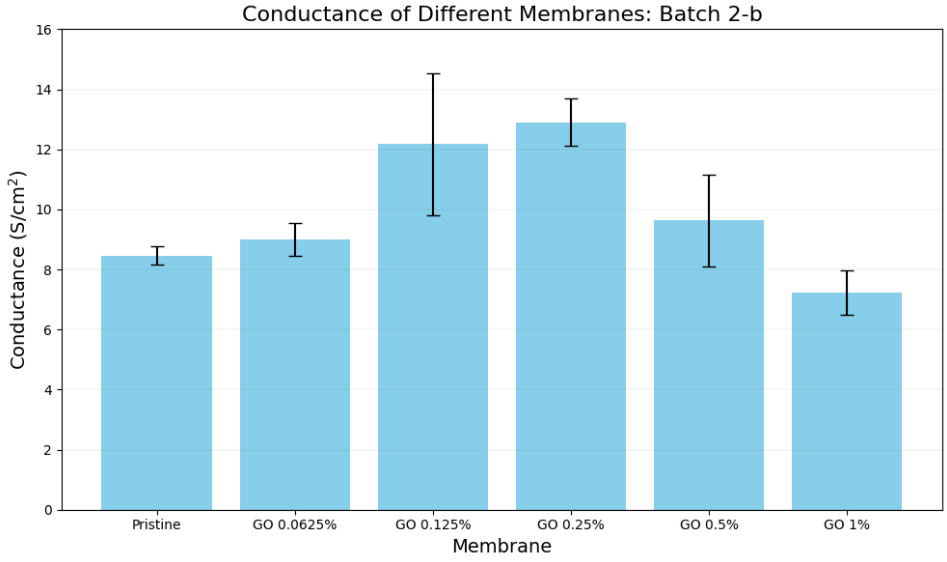

Figure D.5: Conductance of membranes: Batch 2-b.

D.2.3. Batch 1

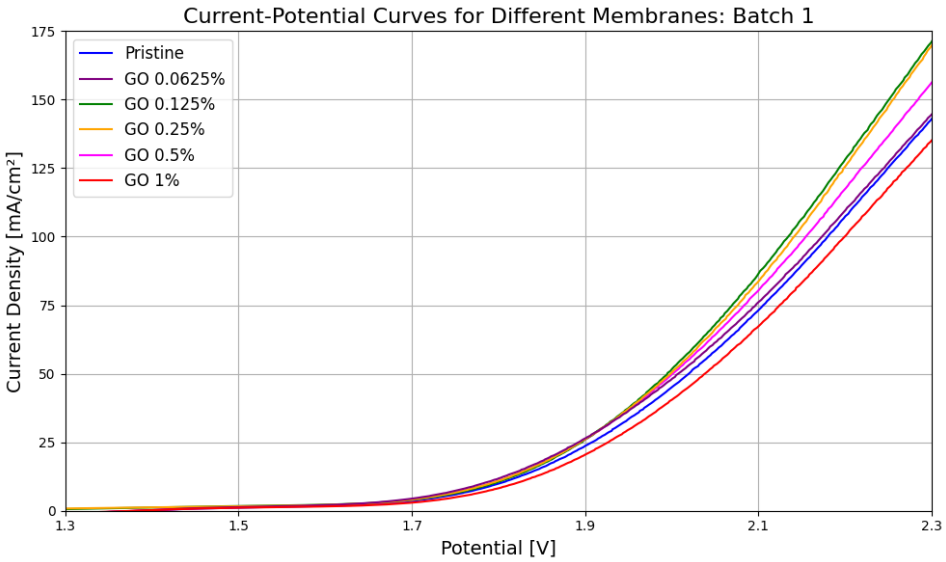

Figure D.6: Current-Potential Curves of membranes: Batch 1.

Table D.3: Membrane Thicknesses for Batch 1

Membrane	Wet Thickness (µm)
Pristine	40
GO 0.0625%	38
GO 0.125%	31
GO 0.25%	32
GO 0.5%	54
GO 1%	53

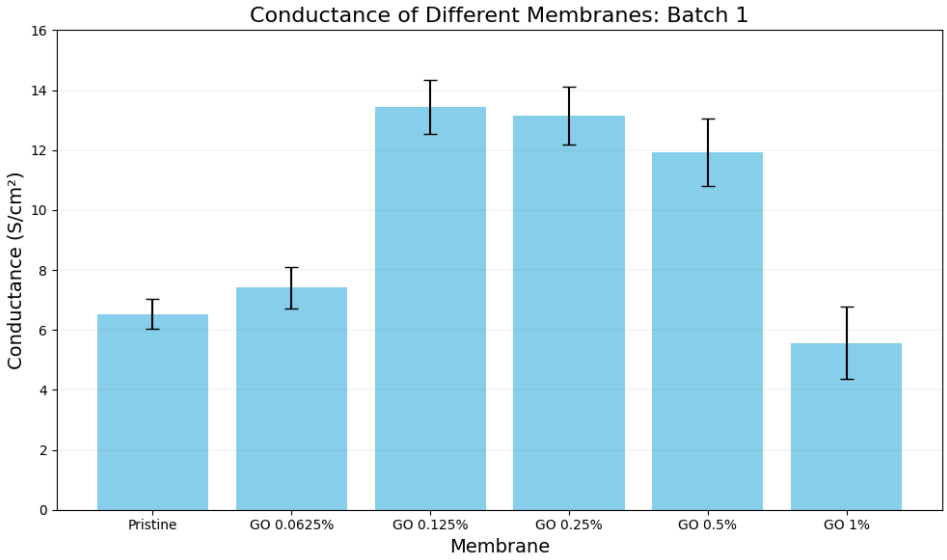

Figure D.7: Conductance of membranes: Batch 1.

D.3. SEM

Figure D.8 presents EDS images of a GO 0.5% membrane sample during cross-sectional analysis. The edge of the cross-section is visible in the top-left image. Although there is a particularly bright spot in the oxygen analysis, which could be attributed to the oxygenated groups in GO, and a corresponding darker spot in the carbon analysis, the results remain inconclusive.

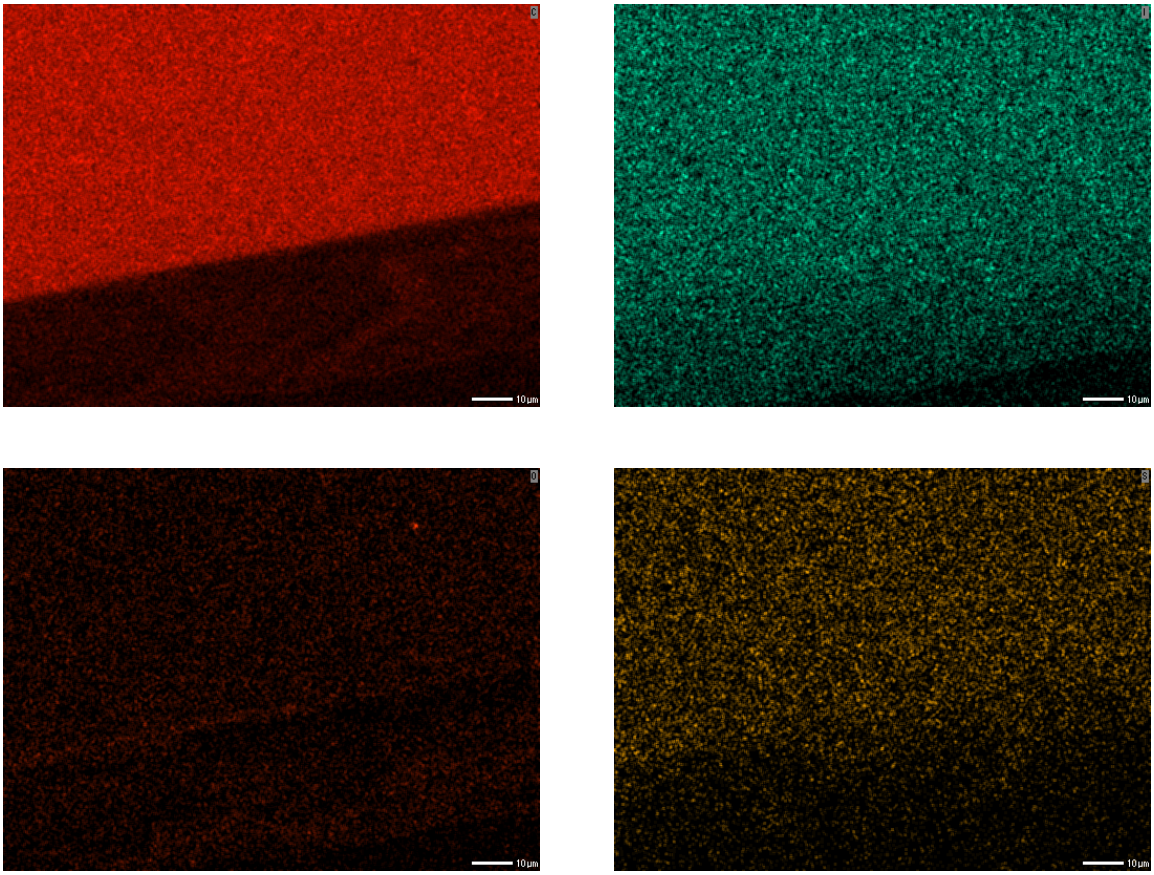

Figure D.8: EDS analysis attempt: (Top left) Carbon, (Top right) Iodine, (Bottom left) Oxygen, (Bottom right) Sulfur.

D.4. TGA

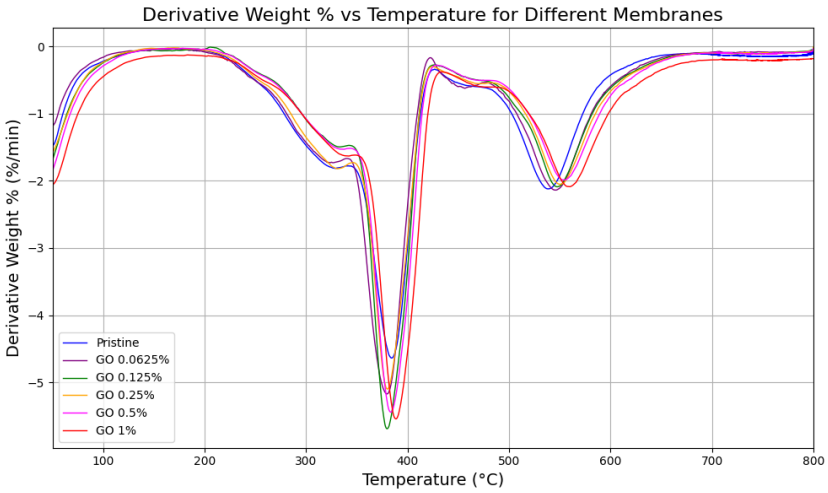

Figure D.9: TGA derivative weight% curves of membranes.

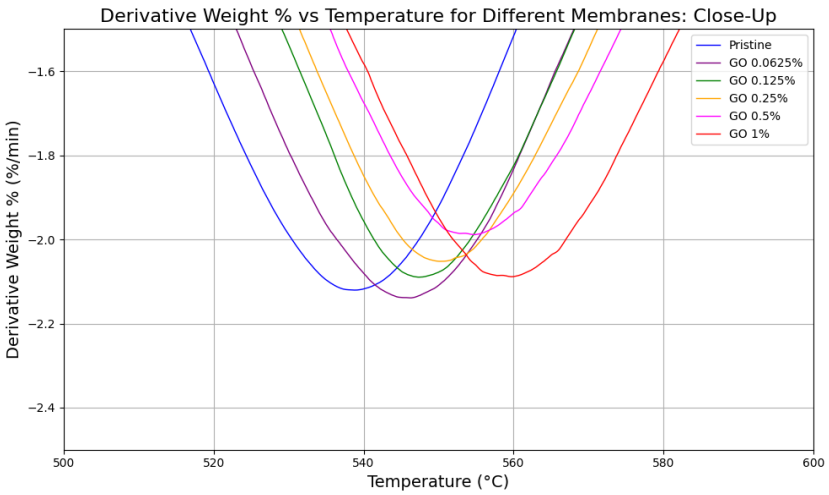

Figure D.10: TGA derivative weight% curves of membranes: close-up

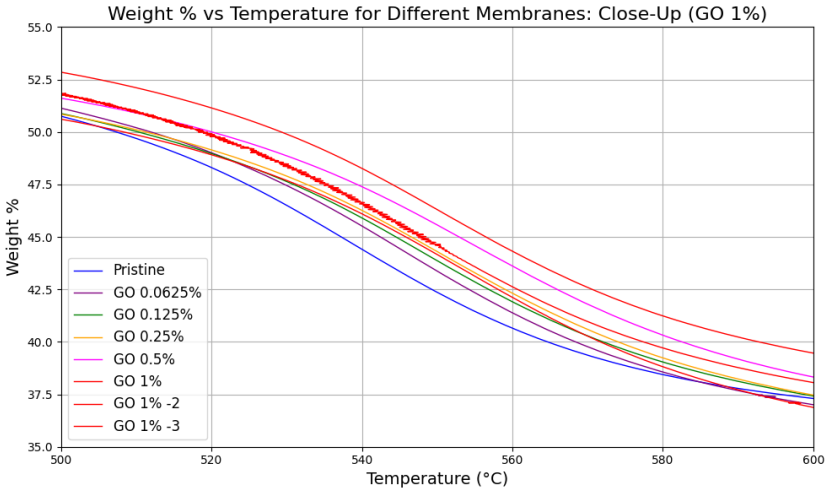

Figure D.11: TGA derivative weight% curves of membranes: close-up.

D.5. Nano-Indentation

In polymers, hardness (H) is typically measured using methods such as the Shore hardness test, the Rockwell hardness test, or nano-indentation. The Shore and Rockwell hardness tests both apply a standardized force or set load, with hardness determined by the final depth of indentation; greater indentation depth indicates a softer material [53]. In contrast, nano-indentation offers more precise measurements at micro- and nano-scales. This technique uses a sharp, calibrated indenter tip that penetrates the material's surface. Nano-indentation can be performed by setting either a maximum depth or a maximum load as the test limit. For thin films, a depth limit is generally preferred to avoid substrate effects [21], [69]. After indentation, the machine analyzes the load-unload curve to determine mechanical properties hardness and Young's modulus.
Young's modulus (E) can also be measured using techniques and machines such as tensile testing machines (e.g., UTM) and dynamic mechanical analysis (DMA). Each method provides insights into material elasticity, with nano-indentation being particularly useful for small-scale or thin-film applications where conventional tensile testing is impractical. Challenges include the need for precise punching to create samples of the correct shape without introducing defects that could alter the breaking characteristics, as well as the difficulty in securely clamping very thin materials in the machine.

Hardness (H) in the Oliver-Pharr method is defined as the maximum applied load (P_{max}) divided by the projected contact area (A_c) of the indentation at peak load, with the following formula [48]:

$$H = \frac{P_{\text{max}}}{A_c}$$

where P_{max} is the maximum load applied during indentation, measured at the end depth of the loading curve, as seen in figure D.12. A_c is the projected contact area of the indentation at maximum depth, which depends on the geometry of the indenter (Berkovich in this case) and is calculated as a function of indentation depth, tip geometry, and contact stiffness.

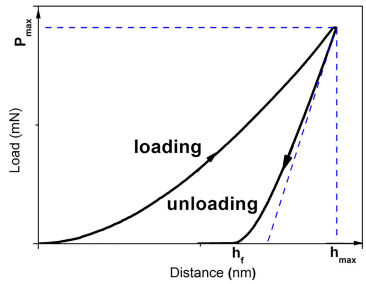

Figure D.12: Loading-Displacement nano-indentation curve.

Young's modulus (E) is calculated from the reduced modulus (E_r), accounting for the elastic properties of both the indenter and the sample. E_r is calculated from the following formula:

$$E_r = \frac{S}{2\sqrt{\pi A_c}}$$

where S is the contact stiffness, or the initial slope of the unloading curve, focusing on the elastic recovery phase. The Young's modulus E of the material can then be obtained by compensating for the indenter's modulus E_i and Poisson's ratio ν_i, as well as the material's Poisson's ratio ν, with the following formula:

$$\frac{1}{E_r} = \frac{1-\nu^2}{E} + \frac{1-\nu_i^2}{E_i}$$

The Poisson's ratio (ν) is a material property that describes the ratio of lateral (transverse) strain to axial (longitudinal) strain when a material is subjected to uniaxial stress. It measures how much a material contracts in directions perpendicular to the direction of stretching or compressing. It is calculated with the following formula [82]:

$$\nu = -\frac{\text{lateral strain}}{\text{axial strain}}$$

The Poisson's ratio (0.34) from polybenzimidazolium was used, as reported in the research paper from which this method was adopted, due to the similarity in testing conditions with a thin anion exchange polymer film embedded with varying concentrations of GO [21]. Polybenzimidazolium likely has a stiffer structure than PFTP due to its rigid molecular configuration, suggesting that PFTP, with its potentially more flexible structure, could have a Poisson's ratio higher than 0.34. However, the primary purpose of this test was to observe relative differences in properties with increasing GO content, in order to compare structural effects, rather than to analyze absolute values of the material properties.

In this study, the continuous stiffness measurement (CSM) mode was employed in nano-indentation. CSM enables dynamic stiffness measurements as the indenter penetrates the material, generating a profile of mechanical properties such as hardness and modulus across various depths. By using CSM, depth-specific and more accurate mechanical property data can be obtained. The CSM method essentially produces multiple smaller load-unload curves at different depths, then averages the values obtained to determine the material properties accurately [69].

It has been reported that, to perform nano-indentation tests on thin polymer films, the indentation depth should be set to a value less than 10% of the total membrane thickness to avoid substrate influence on the measurement. In our case, the membranes had a minimum thickness of 30 µm, so 10% would be 3 µm, making a limit of 1 µm entirely acceptable [64]. However, the measurement should not be too close to the surface, as this would introduce noise and defects, typically leading to an overestimation of the Young's modulus. Additionally, Young's modulus values obtained from nano-indentation tests are generally higher than those measured with DMA [116].

Figure 5.11 in the main text, shows the nano-indentation results for membranes produced from powder polymer from batch 2 of, while figure D.13 shows the nano-indentation results for membranes from batch 1. The higher values for the GO 0.0625% membrane are attributed to the sample being positioned with the casting side facing up, where the properties were measured. This was confirmed through optical microscopy, as casting lines were clearly visible on this side. In contrast, the other samples were carefully oriented with the opposite side facing up, to prevent any roughness from the casting plate lines from affecting the measurements. The higher measurement for GO 0.0625% could be due to this unusual surface roughness or potentially to a higher concentration of GO near the casting side due to gravity during curing. While the values differ slightly from those in figure 5.11, excluding the outlier for GO 0.0625% and considering the standard deviation for GO 1%, the observed trend remains valid.

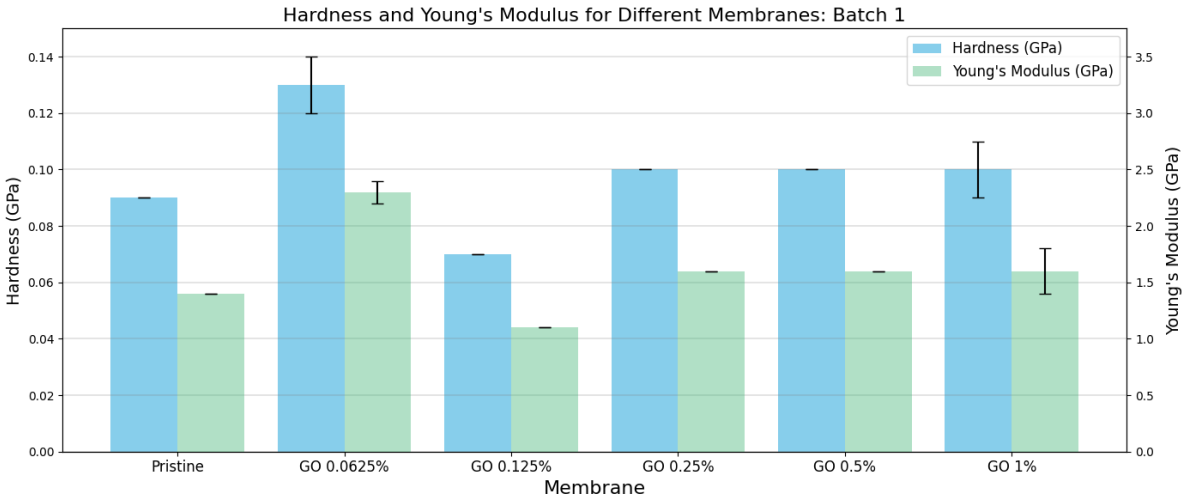

Figure D.13: Hardness and Young's Modulus of membranes: Batch 1.

D.6. WU - SR

Figures 5.12 and 5.13 in the main text report the WU and SR of membranes from batch 2. The following figures D.14 and D.15 present the data for batch 1, which was kept separate from batch 2 due to differences in intrinsic viscosity and, potentially, molecular weight, adding an extra variable to the analysis.

The trends are very similar to those observed for batch 2, but with overall higher values of WU and a higher initial SR for the pristine membrane, followed by lower SR values for membranes with small GO concentrations. According to the hypothesis presented in the main text, this could be attributed to the shorter polymer chains in batch 1, which are less densely entangled and have more free volume. This allows batch 1 to take in more water generally, and exhibit greater swelling in the pristine state. When GO is added, the defects created disrupt crystallinity and increase free volume, making the polymer chains more compliant. This effect is more pronounced with shorter chains, resulting in an even lower SR at 0.125% GO. In fact, even the values of the mechanical properties in figure 5.11 are lower.

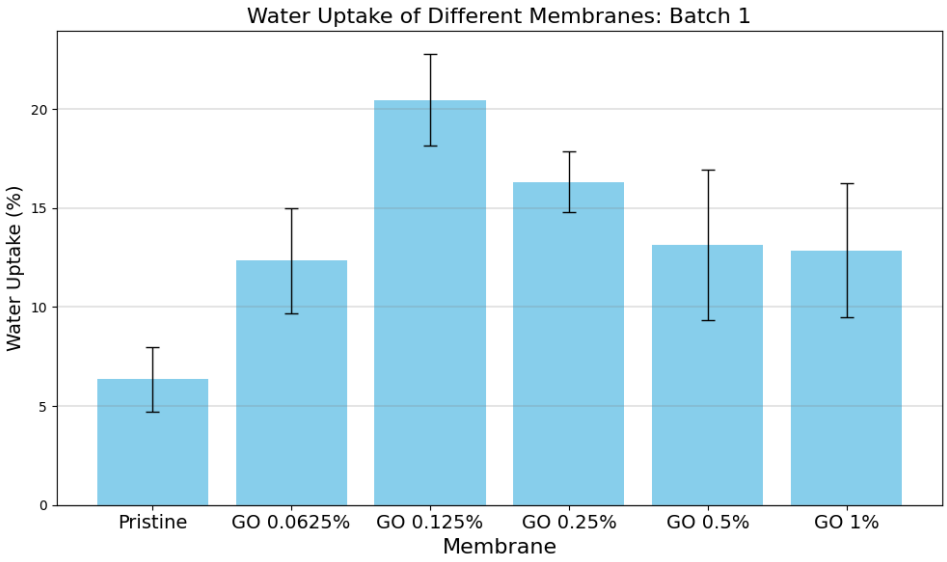

Figure D.14: Water Uptake of membranes: Batch 1.

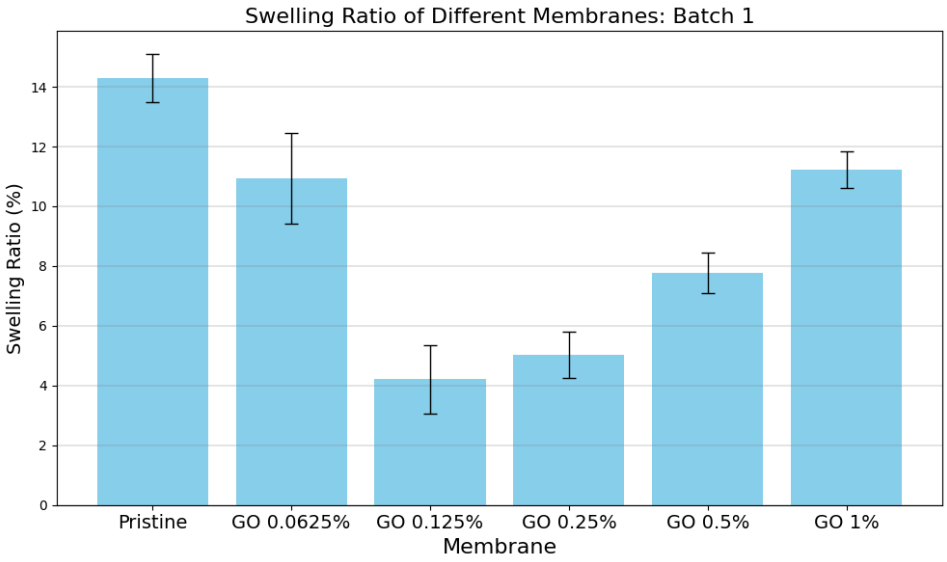

Figure D.15: Swelling Ration of membranes: Batch 1.

D.6.1. Post Electrolyser

Figures D.16 and D.17 show the SR post electrolyser and the total SR of batch 1. While figure D.20 shows an image of a swollen membrane after electrolyser use.

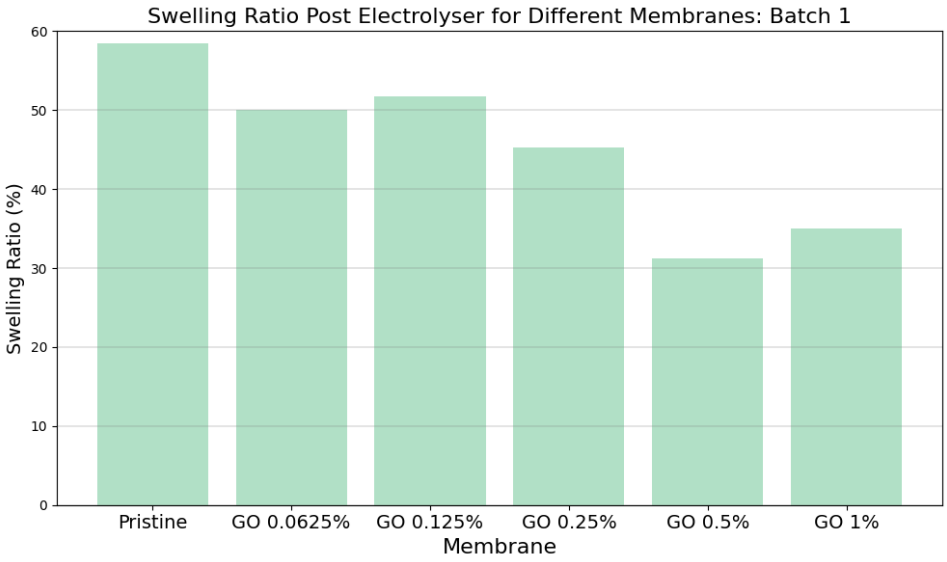

Figure D.16: Swelling Ration post electrolyser of membranes: Batch 1, calculated relative to the pre-electrolysis soaked state.

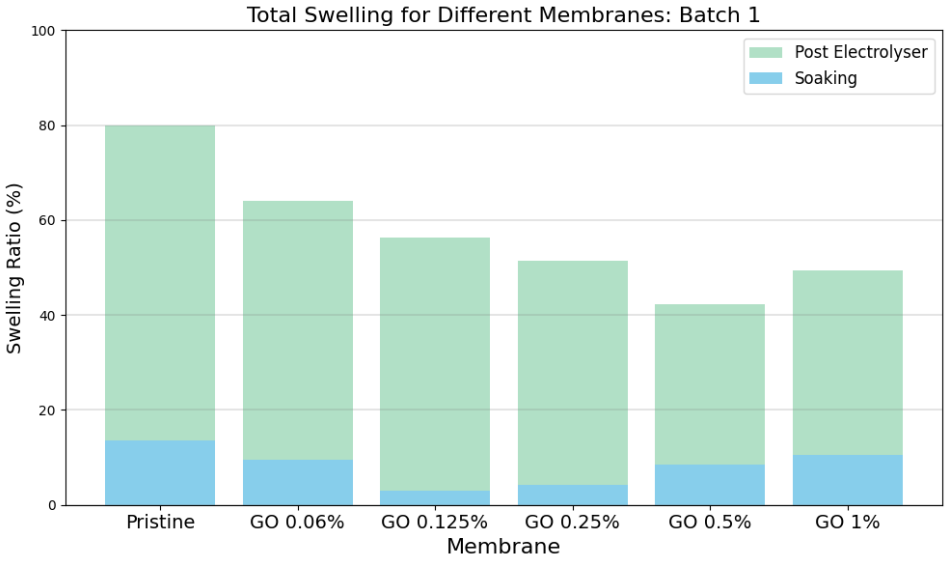

Figure D.17: Total Swelling Ratio of membranes: Batch 1, normalized to the dry state.

Figures D.18 and D.19 show the WU post electrolyser and the total WU of batch 1.

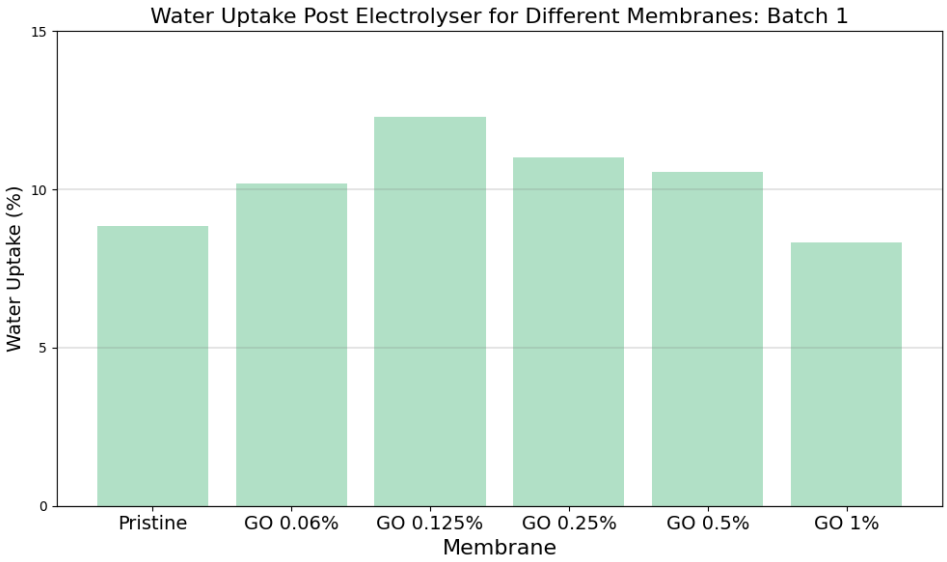

Figure D.18: Water Uptake post electrolyser of membranes: Batch 1, calculated relative to the pre-electrolysis soaked state.

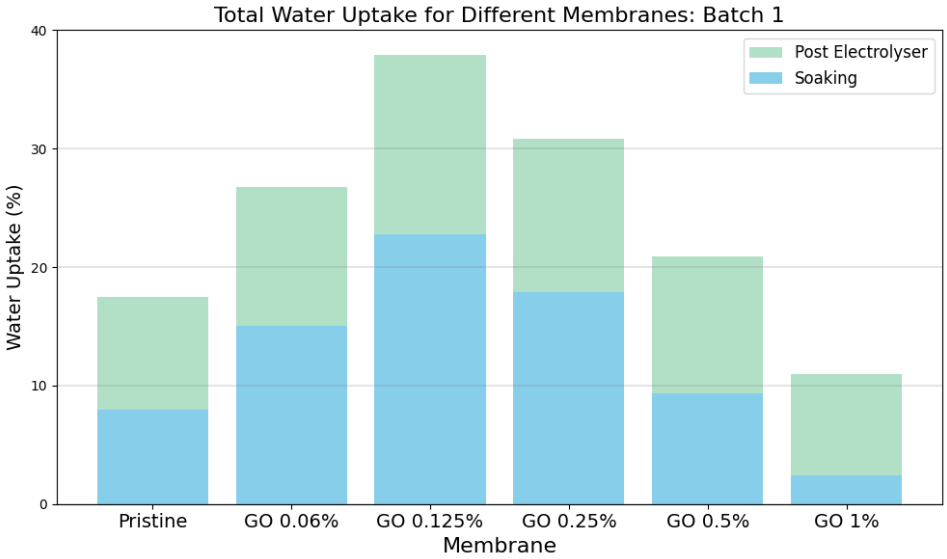

Figure D.19: Total Water Uptake of membranes: Batch 1, normalized to the dry state.

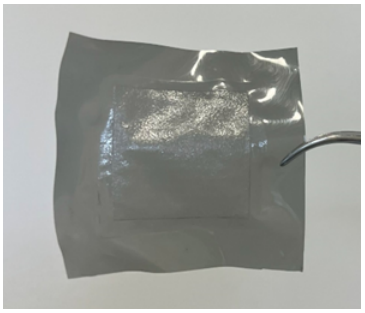

Figure D.20: Image of a swollen membrane post electrolyser.